


Summer 2011

Perfectly Matched Layer Absorbing Boundary Conditions for the Discrete Velocity Boltzmann-BGK Equation

Elena Craig
Old Dominion University

Follow this and additional works at: https://digitalcommons.odu.edu/mathstat_etds

 Part of the [Acoustics, Dynamics, and Controls Commons](#), [Applied Mathematics Commons](#), and the [Physics Commons](#)

Recommended Citation

Craig, Elena. "Perfectly Matched Layer Absorbing Boundary Conditions for the Discrete Velocity Boltzmann-BGK Equation" (2011). Doctor of Philosophy (PhD), dissertation, Mathematics and Statistics, Old Dominion University, DOI: 10.25777/vkxg-ke33 https://digitalcommons.odu.edu/mathstat_etds/19

This Dissertation is brought to you for free and open access by the Mathematics & Statistics at ODU Digital Commons. It has been accepted for inclusion in Mathematics & Statistics Theses & Dissertations by an authorized administrator of ODU Digital Commons. For more information, please contact digitalcommons@odu.edu.

**PERFECTLY MATCHED LAYER ABSORBING
BOUNDARY CONDITIONS FOR THE DISCRETE
VELOCITY BOLTZMANN-BGK EQUATION**

by

Elena Craig
B.S. May 2005, Old Dominion University
M.S. December 2007, Old Dominion University

A Dissertation Submitted to the Faculty of
Old Dominion University in Partial Fulfillment of the
Requirement for the Degree of

DOCTOR OF PHILOSOPHY

MATHEMATICS AND STATISTICS

OLD DOMINION UNIVERSITY
August 2011

Approved by:

Fang Q. Hu (Director)

Chester E. Grosch

Richard D. Noren

Yan Peng

Hideaki Kaneko

ABSTRACT

PERFECTLY MATCHED LAYER ABSORBING BOUNDARY CONDITIONS FOR THE DISCRETE VELOCITY BOLTZMANN-BGK EQUATION

Elena Craig

Old Dominion University, 2011

Director: Dr. Fang Q. Hu

Perfectly Matched Layer (PML) absorbing boundary conditions were first proposed by Berenger in 1994 for the Maxwell's equations of electromagnetics. Since Hu first applied the method to Euler's equations in 1996, progress made in the application of PML to Computational Aeroacoustics (CAA) includes linearized Euler equations with non-uniform mean flow, non-linear Euler equations, flows with an arbitrary mean flow direction, and non-linear Navier-Stokes equations. Although Boltzmann-BGK methods have appeared in the literature and have been shown capable of simulating aeroacoustics phenomena, very little has been done to develop absorbing boundary conditions for these methods. The purpose of this work was to extend the PML methodology to the discrete velocity Boltzmann-BGK equation (DVBE) for the case of a horizontal mean flow in two and three dimensions. The proposed extension of the PML has been accomplished in this dissertation. Both split and un-split PML absorbing boundary conditions are presented in two and three dimensions. A finite difference and a lattice model are considered for the solution of the PML equations. The linear stability of the PML equations is investigated for both models. The small relaxation time needed for the discrete velocity Boltzmann-BGK model to solve the Euler equations renders the explicit Runge-Kutta schemes impractical. Alternatively, implicit-explicit Runge-Kutta (IMEX) schemes are used in the finite difference model and are implemented explicitly by exploiting the special structure of the Boltzmann-BGK equation. This yields a numerically stable solution by the finite difference schemes. As the lattice model proves to be unstable, a coupled model consisting of a lattice Boltzmann (LB) method for the interior domain and an IMEX

finite difference method for the PML domains is proposed and investigated. Numerical examples of acoustic and vorticity waves are included to support the validity of the PML equations. In each example, accurate solutions are obtained, supporting the conclusion that PML is an effective absorbing boundary condition.

ACKNOWLEDGEMENTS

A special thanks to the members of my dissertation committee for their willingness to serve and for their valuable time and input. In particular, thanks to my advisor, Dr. Hu, for his guidance and encouragement throughout the years. Thanks to the National Science Foundation for their financial support of this work (DMS-0810946). Thanks to my family for your love and support.

TABLE OF CONTENTS

	Page
LIST OF FIGURES	viii
Chapter	
1. INTRODUCTION	1
2. THE DISCRETE VELOCITY BOLTZMANN-BGK EQUATION	7
2.1 THE BOLTZMANN EQUATION: RELATING THE MICRO- SCOPIC AND MACROSCOPIC DESCRIPTIONS	7
2.2 THE BGK MODEL	10
2.3 THE DISCRETE VELOCITY BOLTZMANN-BGK MODELS	11
2.4 LINEAR ANALYSIS OF THE DISCRETE VELOCITY BOLTZMANN-BGK EQUATION	14
3. THE PERFECTLY MATCHED LAYER (PML) METHOD	20
3.1 INTRODUCTION TO PERFECTLY MATCHED LAYERS	20
3.2 PROPOSED TWO-DIMENSIONAL PML EQUATIONS	23
3.2.1 DERIVATION OF UNSPLIT PML EQUATIONS	23
3.2.2 FORMULATION OF SPLIT PML EQUATIONS	25
3.2.3 LINEAR STABILITY OF TWO-DIMENSIONAL PML EQUATIONS	27
3.3 PROPOSED THREE-DIMENSIONAL PML EQUATIONS	32
3.3.1 UNSPLIT PML FORMULATION	32
3.3.2 DERIVATION OF SPLIT PML EQUATIONS	35
4. FINITE DIFFERENCES SOLUTION OF PML EQUATIONS	37
4.1 INTRODUCTION TO IMPLICIT EXPLICIT (IMEX) RUNGE- KUTTA SCHEMES	37
4.2 IMEX IMPLEMENTATION	40
4.3 IMEX STABILITY	43
4.4 NUMERICAL EXAMPLES	47
4.4.1 TWO-DIMENSIONAL PML - ACOUSTIC WAVE	47
4.4.2 TWO-DIMENSIONAL PML - VORTICITY WAVE	53
4.4.3 THREE-DIMENSIONAL PML - ACOUSTIC WAVE	54
5. LATTICE SOLUTION OF PML EQUATIONS	60
5.1 THE LATTICE BOLTZMANN EQUATION	60
5.2 LINEAR ANALYSIS OF LATTICE PML	62
5.3 COUPLED SOLUTION	68
5.4 NUMERICAL EXAMPLES	69

5.4.1	ACOUSTIC WAVE	69
5.4.2	VORTICITY WAVE	70
6.	CONCLUDING REMARKS	77
	REFERENCES	80
	VITA	88

LIST OF FIGURES

Figure	Page
1. Schematic of D2Q9 discrete velocity set.	12
2. Dispersion relations of all linear waves supported by Eqs. (24), (25), (26), and D2Q9.	15
3. Dispersion relations of all linear waves supported by Eqs. (24), (25), (26), and D2Q13.	16
4. Diagram of PML domains for a rectangular domain. Dashed lines indicate the interface between the PML domains and interior.	21
5. Illustration of absorption coefficients for PML domains.	24
6. Highest contour levels of maximum imaginary parts, ω_i , of eigenvalues for the x -layer over varying Mach numbers and absorption coefficient σ_x	29
7. Contours of maximum imaginary parts, ω_i , of eigenvalues for the y -layer over varying Mach numbers and absorption coefficient σ_y	30
8. Highest contour levels of maximum imaginary parts, ω_i , of eigenvalues for the corner layer for fixed M over varying absorption coefficients σ_x and σ_y	31
9. Diagram of PML domains in three dimensions.	32
10. Stability regions for the second, third, and fourth order IMEX schemes.	47
11. Scaled norm of acoustic density ρ versus time for $\epsilon = 0.1$ showing the stability value for the ratio $\Delta t/\Delta x$ for the IMEX schemes.	49
12. Contours of IMEX 3 density at times $t = 0, 10, 12$, and 16 for $\epsilon = 0.01$ showing the acoustic pulse exiting the boundaries with little reflection.	50
13. Comparison of IMEX 3 numerical acoustic density solution with exact solution at times $t = 6$ and 12 for $\epsilon = 0.01$	51
14. Maximum difference between IMEX 3 and reference solution of acoustic density ρ versus time along the line segment defined by the points $(4.5, -4.5)$ and $(4.5, 4.5)$ for $\epsilon = 0.01$ and varying PML widths D	53
15. Contours of IMEX 3 v -velocity at times $t = 0, 5, 30$, and 50 for $\epsilon = 0.001$ showing the vorticity wave exiting the boundary without noticeable reflection.	55
16. Comparison of IMEX 3 numerical v -velocity vorticity solution with exact solution at times $t = 5$ and 50 for $\epsilon = 0.001$	56
17. Maximum difference between IMEX 3 and reference solution of vorticity v -velocity versus time along the line segment defined by the points $(4.5, -4.5)$ and $(4.5, 4.5)$ for $\epsilon = 0.001$ and varying PML widths D	57
18. Scaled norm of unsplit PML IMEX 3 acoustic density ρ versus time for $\epsilon = 0.1$, $\Delta t = 0.9 \Delta x$ showing the significance of the factor β for the stability of the PML equations. The most stable solution of those shown is the solution obtained with the prescribed value $\beta_P = 0.4619$	58

19.	Contours of unsplit PML IMEX 3 density at times $t = 0, 4, 6,$ and 8 for $\epsilon = 0.1$ showing the acoustic wave exiting the boundaries with small reflection.	59
20.	Contours of LB density at times $t = 0, 10, 12,$ and 16 for $\epsilon = 0.01$ showing the reflections generated by the acoustic wave exiting the boundary.	64
21.	Comparison of LB numerical acoustic density solution with exact solution at times $t = 6$ and 12 for $\epsilon = 0.01$	65
22.	Contours of LB v -velocity at times $t = 0, 5, 30,$ and 50 for $\epsilon = 0.001$ showing the reflections generated by the vorticity wave exiting the boundary.	66
23.	Comparison of LB numerical v -velocity vorticity solution with exact solution at times $t = 5$ and 50 for $\epsilon = 0.001$	67
24.	Diagram of LB-IMEX 3 coupling for a 5-point finite difference stencil.	68
25.	Scaled norm of filtered LB-IMEX 3 acoustic density ρ versus time for $\epsilon = 0.1$ and $\Delta x = \Delta y = \Delta t = 0.1$	70
26.	Contours of LB-IMEX 3 density at times $t = 0, 10, 12,$ and 16 for $\epsilon = 0.01$ showing the acoustic wave exiting the boundary with small reflection.	71
27.	Comparison of LB-IMEX 3 numerical acoustic density solution with exact solution at times $t = 6$ and 12 for $\epsilon = 0.01$	72
28.	Maximum difference between LB-IMEX 3 and reference solution of acoustic density ρ versus time along the line segment defined by the points $(4.5, -4.5)$ and $(4.5, 4.5)$ for $\epsilon = 0.01$ and varying PML widths D	73
29.	Contours of LB-IMEX 3 v -velocity at times $t = 0, 5, 30,$ and 50 for $\epsilon = 0.001$ showing the vorticity wave exiting the boundary with small reflection.	74
30.	Comparison of LB-IMEX 3 numerical v -velocity vorticity solution with exact solution at times $t = 5$ and 50 for $\epsilon = 0.001$	75
31.	Maximum difference between LB-IMEX 3 and reference solution of vorticity v -velocity versus time along the line segment defined by the points $(4.5, -4.5)$ and $(4.5, 4.5)$ for $\epsilon = 0.001$ and varying PML widths D	76

CHAPTER 1

INTRODUCTION

Whether used to make the best choice of graft for a heart bypass surgery, to determine the path of a hurricane, or to design airplanes, Computational Fluid Dynamics (CFD) simulations are helping us gain insight and make decisions and predictions for a wide variety of important real life applications. Traditionally, CFD simulations have been carried out by solving the macroscopic governing equations of fluid flow, i.e. the Navier-Stokes and Euler equations. However, in recent years, methods based on the Boltzmann-BGK equation of gas kinetic theory have gained in popularity and have shown to be a good alternative to the Navier-Stokes equations for investigating fluid behavior. Not only can the macroscopic governing equations be recovered from the Boltzmann-BGK equation, but because it describes fluids at the microscopic level, the Boltzmann-BGK equation retains more physics of fluids, in particular for non-equilibrium flows. Furthermore, the Boltzmann-BGK equation can be solved for various flows where the macroscopic governing equations are extremely difficult or impossible to solve, as in the case of inhomogeneous multiphase and multicomponent flows.

The continuous Boltzmann equation is based on the gas kinetic theory and gives a microscopic description of fluids [1, 2]. Instead of solving for the macroscopic flow properties, the Boltzmann equation computes a particle velocity distribution function f which describes the probability that a particle with microscopic velocity $\boldsymbol{\xi}$ can be found in location \boldsymbol{x} at time t . The macroscopic flow properties such as density, momentum, energy and the stress tensor are given by the moments of the distribution function f with respect to the particle velocity $\boldsymbol{\xi}$. The Boltzmann-BGK equation is obtained from the continuous Boltzmann equation by replacing the collision operator with the Bhatnagar-Gross-Krook (BGK) collision model which approximates the tendency of a system to approach equilibrium through a relaxation process with constant relaxation time λ [2, 3]. If the infinite velocity space $\boldsymbol{\xi}$ is also reduced to a finite number of discrete velocities $\{\boldsymbol{\xi}_j\}$ such that the ability of the system to produce accurate fluid dynamics is maintained, then we obtain the discrete velocity Boltzmann-BGK equation (DVBE). The 2D 9-velocity (D2Q9) and the 3D

This dissertation follows the style of the *AIAA Journal*

27-velocity (D3Q27) models are two examples of such discrete velocity sets [4].

Numerical solutions of the discrete velocity Boltzmann-BGK equation can be obtained by finite difference and finite volume methods [5–8] as well as lattice methods [9–14]. The lattice methods are based on the lattice Boltzmann (LB) equation which was initially developed as an extension of lattice gas automata [15]. However, the lattice Boltzmann equation can be derived as a space-time discretization of the DVBE which can be translated to a simple two-step evolution procedure for the probability distribution functions $\{f_j\}$ on a discrete lattice [3,4]. The evolution procedure consists of a local collision step with constant relaxation time and a streaming of the distribution functions from one lattice point to the next relative to the discrete velocities. This process makes the LB method simple to implement, fast in execution, and well suited for parallel computing, which is why the LB method has become a widely used numerical tool for investigation and prediction in practical engineering applications. Substantial progress has been made in the past two decades in extending the capabilities of the LB method to a wide range of CFD problems, including flows with complex geometries, turbulent flows, multi-component and multi-phase flows, thermal flows and other complex physical systems ([9] and references cited therein).

In recent years, numerical methods based on the discrete velocity Boltzmann-BGK equation have also been applied to problems of Computational Aeroacoustics (CAA) [7,8,11,12,14,16]. Wave propagation problems, such as those arising in CAA, often involve infinite or very large physical domains which would be either unfeasible or very expensive to solve numerically. To reduce the computational cost and time to a level that current resources can handle, the computational domain is often truncated. Artificially truncating the physical domain creates numerical boundaries which have to allow both the aerodynamic disturbances and the acoustic waves to pass through without reflection in order to maintain an accurate flow solution. The type of boundary conditions that control spurious wave reflections from the boundaries are referred to as non-reflective boundary conditions.

The development of effective non-reflective boundary conditions is a very important aspect of simulating flows in unbounded domains and is crucial to Aeroacoustic problems. Numerous non-reflective boundary conditions have been proposed for the governing equations used in traditional CFD and CAA. Among these are the asymptotic boundary conditions [17–22], the characteristic boundary conditions [23–27],

the absorbing layers [28–37], and the Perfectly Matched Layer [38–44], which is the subject of the present work.

Asymptotic boundary conditions are derived from the far-field asymptotic expansion of the solution of the governing equation in physical space [45]. To use this type of boundary condition effectively, the computational domain must be sufficiently large so that the artificial boundaries are located far enough from the source for the truncated asymptotic solution to be considered valid. One immediate drawback of this method is the fact that the far-field asymptotic expansion of the solution must be known. Another drawback is the loss of computational efficiency as it may be necessary to simulate a larger computational domain than is physically relevant to satisfy the asymptotic assumptions.

Characteristic boundary conditions are obtained from the characteristic wave analysis of the governing equations. More specifically, the Jacobian matrix of the governing equations is diagonalized and the sign of the eigenvalues is used to identify waves as either incoming or outgoing. The boundary conditions are then specified to take into account the type of wave under consideration. To make sure the problem is well defined, the boundary conditions for outgoing waves must be extrapolated from inside the domain and cannot be specified. This type of boundary condition is very effective when the waves exiting the domain are normal to the boundary, but produces reflections when the angle of incidence is not zero or when nonlinear disturbances cross the outflow boundary.

The absorbing layers, also known as “sponge layers,” “exit zones”, or “buffer zones,” are obtained by extending the computational domain with regions where modified equations reduce the amplitude of outgoing waves so reflections are minimized. The construction of these boundary conditions can be done in a number of ways. Some frequently used methods in CFD and CAA include adding artificial dissipation and damping terms to the governing equations, modifying the characteristics of the governing equations, grid stretching, and numerical filtering [46]. These methods can be combined with one another or with other non-reflective boundary conditions for better performance. However, if the attenuation of the outgoing waves is not done in a gradual fashion, reflections can be created within the absorbing layers themselves.

The Perfectly Matched Layer (PML) technique is similar to the absorbing layers as the computational domain is extended with artificial layers where the outgoing

waves are absorbed exponentially in time. The advantage of using PML over other types of absorbing zones, is that PML equations match the governing equations at the boundary of the computational domain. As a result, the PML layers do not need to be as wide as other absorbing layers to show improved accuracy.

The Perfectly Matched Layer (PML) technique was first derived by Berenger in 1994 by manually constructing the conditions for non-reflective incident waves for Maxwell's equations [47]. It was subsequently shown to be equivalent to a more general approach, referred to as stretched-coordinate PML [48–50]. Recently, the PML methodology has been applied to the governing equations of CFD and CAA. In particular, PML has been extended to linearized Euler equations with non-uniform mean flow [40], to non-linear Euler equations [41, 51], to flows with an arbitrary mean flow direction [44], and to non-linear Navier-Stokes equations [51].

Compared to the extensive studies in the traditional CFD, research on the boundary conditions for numerical methods based on the Boltzmann-BGK equation is relatively limited. Kam et al. investigated three types of nonreflecting boundary conditions for the DVBE: the extrapolation method which is obtained by requiring that either \mathbf{f} or its first gradient be zero in every lattice direction, the C^1 continuity method which extrapolates \mathbf{f} on the boundary based on at least two known points inside the domain, and an absorbing boundary condition which is formed by adding a damping term to the Boltzmann equation [11]. Najafiyazdi and Mongeau applied the Perfectly Matched Layer (PML) technique to the lattice Boltzmann equation but their formulation has limited applicability to the field of CAA [52].

The objective of this thesis is to augment the existing research of the Perfectly Matched Layer as an absorbing boundary condition for the discrete velocity Boltzmann-BGK equation with specific application to the field of CAA. Thus far, the majority of work relating to the application of PML to CAA problems has been done for the Euler and Navier-Stokes governing equations. By comparison, very little has been done to extend the capabilities of the PML to the Boltzmann-BGK equation [52]. As more models based on the Boltzmann-BGK equation are being developed for CFD and CAA, there is a need for robust absorbing boundary conditions so these models can be used in practical applications.

Of specific importance in the present work is the derivation of PML equations for the discrete velocity Boltzmann-BGK equation in cartesian coordinates for the case of horizontal mean flow. For the aforementioned case, we derive new PML equations

in split and unsplit variables for two and three dimensions. An examination of the linear waves supported by a simple 9-velocity discrete Boltzmann-BGK equation shows that it supports the familiar acoustic and vorticity waves, in addition to other highly damped wave modes. The dispersion relations of the acoustic and vorticity waves of the 9-velocity discrete model are found to be similar to those of the Euler equations. Based on this fact, we are justified in expecting to be able to construct stable and effective PML equations following the same space-time transformation used by Hu to derive the PML for the Euler equations [39, 40]. The specific steps taken to derive the PML equations are detailed in Chapter 3.

To validate the PML equations, we use discrete velocity models with a small number of discrete velocities, i.e. the two dimensional 9-velocity model, referred to as D2Q9, and the three dimensional 19-velocity model known as D3Q19 [15]. We also consider solutions obtained by both a finite difference and a lattice method and we limit our study to inviscid flows. In order for the Boltzmann-BGK model to solve the Euler equations, the relaxation time λ has to be very small, or, in other words, the collision operator is highly stiff. When we seek a finite difference solution to the PML equations, the stiffness of the collision term renders the traditional explicit time integration schemes impractical because the stability restriction on the time step size is quite severe. On the other hand, use of implicit integration schemes would require that a linear system be solved at each time step which would be computationally expensive.

Alternatively, we consider implicit explicit (IMEX) Runge-Kutta schemes which have the benefit of an explicit implementation and a larger stability region than explicit schemes. The stability regions for the second, third, and fourth order IMEX Runge-Kutta schemes used for the finite difference solution of the PML equations are new to this work. The IMEX Runge-Kutta schemes are specifically designed and optimized for the integration of systems that contain both stiff and non-stiff terms. The implicit scheme is optimized for the integration of stiff terms while the explicit scheme is optimized for non-stiff terms so the combination of the two gives a larger stability region than if either scheme was used to integrate the whole system. Due to the special properties of the collision term in the Boltzmann-BGK equation, the implicit stages can be treated explicitly [10, 53, 54]. A description of IMEX schemes and how they are implemented explicitly in this work is given in Chapter 4.

Also of importance in this work is the coupled method we propose for the use

of the PML absorbing boundary conditions with the lattice Boltzmann equation. In this coupled model, described in detail in Chapter 5, the PML equations are solved with the third order IMEX Runge-Kutta finite difference scheme while the interior domain solution is obtained by the lattice Boltzmann method. In Chapter 6, we discuss some of the advantages and disadvantages of the two numerical methods we used in this work to solve the DVBE and the PML equations.

CHAPTER 2

THE DISCRETE VELOCITY BOLTZMANN-BGK EQUATION

2.1 THE BOLTZMANN EQUATION: RELATING THE MICROSCOPIC AND MACROSCOPIC DESCRIPTIONS

One of the basic hypothesis of statistical mechanics states that all macroscopic properties of a system that are independent of mass, such as density, pressure, viscosity and temperature, can be described in terms of the microscopic state of that system. Given in terms of the spatial coordinate and momentum of each constituent molecule, the microscopic description requires the use of $3N$ spatial coordinates $\{\mathbf{q}\}$, and $3N$ conjugate momenta, $\{\mathbf{p}\}$, where $N \approx 10^{23}$ is the number of molecules in the system. The $6N$ dimensional space, also known as phase space, contains all the possible states of the system under consideration. If the intermolecular forces are known at a given time, then theoretically the state of the system can be determined for any later or earlier time from the Hamilton equations [55]. From a practical point of view, solving the equations of motion at the microscopic level is impossible to achieve, first of all, because of the large number of variables involved and, secondly, because the microscopic state of a system at any given time is impossible to determine.

If a probabilistic approach is taken instead, then the microscopic state of the system does not need to be specified. This is done by considering a large collection of η systems which are equivalent at the microscopic level to the system of interest. Each system in this collection, also known as a Gibbs ensemble, can be represented by a point in the phase space. As the number of systems in the ensemble tends to infinity, the points that represent them become dense in the phase space and their distribution in the phase space can be described by a continuous probability density function.

The probability density function F_N is defined so that $F_N(\{\mathbf{q}\}, \{\mathbf{p}\}, t) \prod_{i=1}^N d\mathbf{q}_i d\mathbf{p}_i$ represents the fraction of phase points found in the incremental volume $\prod_{i=1}^N d\mathbf{q}_i d\mathbf{p}_i$ about the point \mathbf{q}, \mathbf{p} at time t [56]. If we know how F_N depends on the phase at one particular point in time, then from the Hamilton equations we can find F_N at any past or future time. The time evolution of F_N due to the natural motion of each ensemble member in the phase space is governed by Liouville's equation [56]. It is assumed that in determining the macroscopic properties of a system from its

microscopic state, averages taken over time and averages taken over the statistical ensemble are the same. Clearly, in attempting to solve Liouville's equation, we are still confronted with a large number of degrees of freedom and the issue of specifying the dependence of F_N on the phase point for a particular time.

The problem can be reformulated by integrating F_N over part of the variables to obtain the so called reduced particle density distribution functions [57]. The contraction of the N -particle system governed by Liouville's equation in terms of the reduced particle distribution functions leads to the Bogoliubov-Born-Green-Kirkwood-Yvon (BBGKY) hierarchy of equations for the R -particle system [58]. If we denote a phase point by \mathbf{y} , the R -particle distribution function is defined as: $F_R(\mathbf{y}_1, \mathbf{y}_2, \dots, \mathbf{y}_R, t) = \int F_N(\mathbf{y}_1, \dots, \mathbf{y}_R, \dots, \mathbf{y}_N, t) d\mathbf{y}_{R+1}, \dots, d\mathbf{y}_N$. Then $F_1(\mathbf{y}_1, t)$ represents the probability of finding molecule 1 in the incremental volume $d\mathbf{y}_1$ about the phase point \mathbf{y}_1 at time t . The R -th equation in the BBGKY hierarchy of equations ties the time evolution of the R -particle probability density function F_R to the evolution of the $(R + 1)$ -particle probability density function F_{R+1} .

In trying to relate the macroscopic and microscopic descriptions through the BBGKY hierarchy, the problem of specifying initial conditions for the system and the large number of degrees of freedom still remain. In addition, we are confronted with the fact that the equations in the BBGKY hierarchy are not self contained. However, the most relevant macroscopic properties can be obtained from averages taken with respect with the first few distribution functions and the BBGKY hierarchy of equations can be truncated in certain limiting cases to obtain more tractable problems.

The BBGKY chain can be truncated at F_1 if we make the assumptions consistent with the Boltzmann gas limit, i.e. the density is low enough to consider only two-particle collisions, the velocities of colliding particles are not correlated before collision and are independent of position, and external forces do not influence the local collision dynamics. The self contained equation for F_1 is the well-known Boltzmann equation. When he derived his equation in 1872, Boltzmann used a heuristic approach. The connection of the Boltzmann equation to Liouville's equation and the elementary laws of mechanics was only made in 1946 [58–60].

If we define the phase points in terms of spatial coordinate \mathbf{x} and velocity $\boldsymbol{\xi}$ and let $f(\mathbf{x}, \boldsymbol{\xi}, t)$ denote the single-particle density distribution function, then the Boltzmann equation can be written as:

$$\frac{\partial f}{\partial t} + \boldsymbol{\xi} \cdot \nabla_{\boldsymbol{x}} f + \boldsymbol{a} \cdot \nabla_{\boldsymbol{\xi}} f = \Omega(f) \quad (1)$$

where $\Omega(f)$ represents the collision integral and \boldsymbol{a} is the external force on the particle.

At this point we can make the connection to the macroscopic hydrodynamical description because the macroscopic fluid mass density ρ , the macroscopic velocity \boldsymbol{u} , the specific internal energy e , the pressure tensor \boldsymbol{P} and the heat flux \boldsymbol{Q} can be obtained from the moments of the single-particle distribution f with respect to its velocity argument [56, 61]. The first three are given by the following:

$$\rho(\boldsymbol{x}, t) = \int f(\boldsymbol{x}, \boldsymbol{\xi}, t) d\boldsymbol{\xi} \quad (2)$$

$$\rho(\boldsymbol{x}, t)\boldsymbol{u}(\boldsymbol{x}, t) = \int f(\boldsymbol{x}, \boldsymbol{\xi}, t)\boldsymbol{\xi} d\boldsymbol{\xi} \quad (3)$$

$$\rho(\boldsymbol{x}, t)e(\boldsymbol{x}, t) = \int f(\boldsymbol{x}, \boldsymbol{\xi}, t)\frac{(\boldsymbol{\xi} - \boldsymbol{u})^2}{2} d\boldsymbol{\xi} \quad (4)$$

The collision operator is an integral that quantifies the effect that particle collisions have on the evolution of the single particle distribution function over time. Even when only binary collisions are considered, the form of $\Omega(f)$ is rather complex [56]. However, we do not need to know the specific expression for the collision integral in order to understand some of its properties, which will be used in Chapter 4 for the application of IMEX Runge-Kutta schemes to the Boltzmann-BGK equation. Owing to the fact that binary collisions conserve mass, momentum, and energy, we can see that if we multiply the collision operator by 1, $\boldsymbol{\xi}$, and $\boldsymbol{\xi}^2$ and integrate over $\boldsymbol{\xi}$, we obtain:

$$\int \Omega(f) d\boldsymbol{\xi} = 0 \quad (5)$$

$$\int \Omega(f)\boldsymbol{\xi} d\boldsymbol{\xi} = 0 \quad (6)$$

$$\int \Omega(f)\boldsymbol{\xi}^2 d\boldsymbol{\xi} = 0 \quad (7)$$

The quantities 1, $\boldsymbol{\xi}$, and $\boldsymbol{\xi}^2$ are known as collisional invariants.

Another important aspect of the Boltzmann equation which can be derived without knowing the specific form of the collisional operator is the H-theorem which describes how the system approaches equilibrium and specifies the equilibrium state.

The global equilibrium state as given by the H-theorem and verified independently by equilibrium statistical mechanics is the Maxwellian distribution function [56]:

$$f_M(\boldsymbol{\xi}) = \frac{\rho}{(2\pi RT)^{\frac{3}{2}}} e^{-(\boldsymbol{\xi}-\mathbf{u})^2/2RT} \quad (8)$$

where R is the Boltzmann gas constant and T is the temperature.

The macroscopic hydrodynamical equations for the conservation of mass, momentum and energy can be obtained by multiplying the Boltzmann equation successively by the collisional invariants and integrating over $\boldsymbol{\xi}$. Due to the presence of higher order moments, the conservation equations are not closed. Various assumptions can be made to close these equations and obtain macroscopic governing equations. In the Chapman-Enskog approximation, this is accomplished by expanding the equations for the moments of f in a power series in small Knudsen number with the conjecture that the time dependence of f is determined only through ρ , \mathbf{u} , and T [62]. The first and second order Chapman-Enskog approximations yield the Euler and Navier-Stokes equations. Alternatively, Grad obtained a closed system of equations, referred to as Grad's 13 moment method, by expanding the single particle distribution function on the basis of the Hermite orthogonal polynomials in velocity space [63]. However, we do not need to solve the macroscopic governing equations to obtain the macroscopic variables of interest because these result directly from f which is obtained by solving the Boltzmann equation.

2.2 THE BGK MODEL

Due to the complex nature of the collision operator, obtaining solutions to the Boltzmann equation proves to be a daunting task. More solvable versions, referred to as model equations, have been proposed in the literature [2, 64–67]. These equations are obtained by replacing the collisional integral in the Boltzmann equation with a simplified collision model.

In order for the model equations to be good approximations to the Boltzmann equation, they should exhibit some of the same properties. As we mentioned before, collisional invariants are used to derive the macroscopic hydrodynamical equations for conservation of mass, momentum and energy from the Boltzmann equation. Since they have a direct effect on the macroscopic behavior of the system, the collisional invariants must be preserved by the model equation. At the same time, the model

equation should have an H-theorem to ensure that the system evolves towards the Maxwellian equilibrium distribution function both globally and locally.

A simple model equation which preserves the collisional invariants and has an H-theorem is the BGK model which was derived by Bhatnagar, Gross and Krook , and independently by Welander in 1954 [2,64]. The rationale behind the BGK model is that many of the gritty details of the binary collisions will not have a significant impact on the macroscopic variables. The effect of collisions on the distribution function f in the BGK model is proportional to the difference of f from its local Maxwellian f^{eq} . Absent of any external force, the Boltzmann-BGK equation can be written as

$$\frac{\partial f}{\partial t} + \boldsymbol{\xi} \cdot \nabla f = -\frac{1}{\lambda} (f - f^{eq}) \quad (9)$$

where λ is the relaxation time constant.

Because collisions only depend on local information, the BGK model equation is no longer a nonlinear integral-differential equation. However, despite its simple appearance, the BGK model equation is a highly nonlinear equation because the Maxwellian equilibrium distribution function f^{eq} depends locally on density, velocity, and internal energy which are all obtained from the moments of f .

In practice, the Boltzmann-BGK model can be used to obtain qualitatively good results for a wide variety of flow regimes. This is done by selecting the relaxation time to match the macroscopic transport coefficients of the flow. One of the greatest failures of this model is an incorrect prediction for the Prandtl number which is defined as the ratio of kinematic viscosity to thermal diffusivity.

2.3 THE DISCRETE VELOCITY BOLTZMANN-BGK MODELS

The discrete velocity Boltzmann-BGK models are obtained by discretizing Eq. (9) in velocity space using a finite set of velocity vectors $\{\boldsymbol{\xi}_i\}$. The discrete velocities $\boldsymbol{\xi}_i$ are chosen so that the resulting discrete model satisfies the conservation laws and is therefore able to produce accurate macroscopic fluid dynamics [68]. Some of the most commonly used discrete velocity models can be derived by expanding the Maxwellian distribution function in a Taylor series in the fluid velocity \mathbf{u} . In the Chapman-Enskog calculation, the functional form of the equilibrium distribution

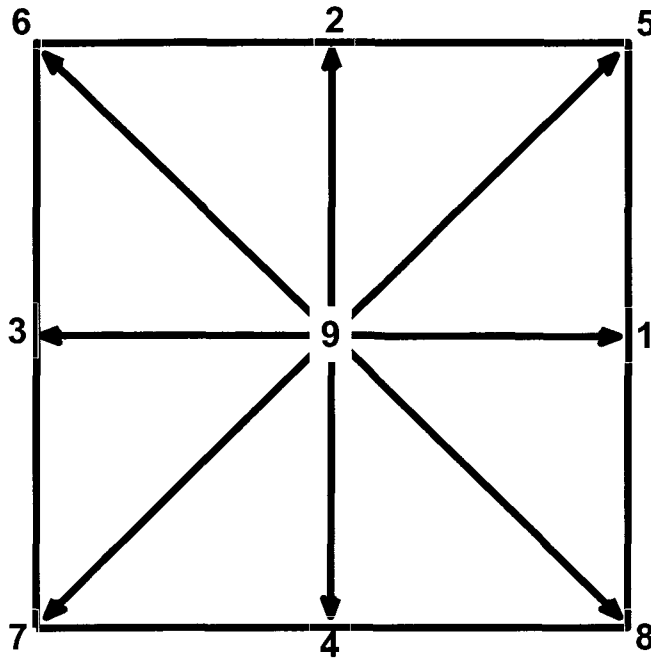


Fig. 1: Schematic of D2Q9 discrete velocity set.

function is only used to obtain the low order moments in velocity space. For the Taylor expanded Maxwellian, these moments can be calculated exactly through Hermite-Gauss quadrature. Moreover, in order to recover the Navier-Stokes equations through the Chapman-Enskog procedure, only terms up to \mathbf{u}^2 need to be retained [3]. The coefficients of the discrete velocity equilibrium distribution function are obtained by replacing the quadrature computed moments into the Taylor expansion of the Maxwellian. For example, a widely used two dimensional velocity discretization of Eq. (9), referred to as the 2D 9-velocity (D2Q9) model can be obtained in this way. This model uses the following discrete velocity set [15]:

$$\begin{aligned}
 \boldsymbol{\xi}_1 &= c(1, 0)^T; & \boldsymbol{\xi}_2 &= c(0, 1)^T; & \boldsymbol{\xi}_3 &= c(-1, 0)^T; & \boldsymbol{\xi}_4 &= c(0, -1)^T \\
 \boldsymbol{\xi}_5 &= c(1, 1)^T; & \boldsymbol{\xi}_6 &= c(-1, 1)^T; & \boldsymbol{\xi}_7 &= c(-1, -1)^T; & \boldsymbol{\xi}_8 &= c(1, -1)^T \\
 \boldsymbol{\xi}_9 &= c(0, 0)^T
 \end{aligned} \tag{10}$$

where c is a reference speed. The equilibrium distribution function for this model is given by

$$f_i^{eq} = w_i \rho \left[1 + \frac{3(\boldsymbol{\xi}_i \cdot \mathbf{u})}{c^2} + \frac{9(\boldsymbol{\xi}_i \cdot \mathbf{u})^2}{2c^4} - \frac{3(\mathbf{u} \cdot \mathbf{u})}{2c^2} \right] \quad (11)$$

where ρ and \mathbf{u} are macroscopic density and velocity respectively and w_i is the weight for velocity $\boldsymbol{\xi}_i$ with

$$w_1 = w_2 = w_3 = w_4 = 1/9; \quad w_5 = w_6 = w_7 = w_8 = 1/36; \quad w_9 = 4/9 \quad (12)$$

and speed of sound

$$c_s = \sqrt{c/3} \quad (13)$$

Shan and He showed that using a set of velocities that correspond to the nodes of a Gauss-Hermite quadrature to discretize the Boltzmann-BGK equation is equivalent to truncating the Hermite expansion of the distribution function to the corresponding order [68]. Because the truncated part of the distribution function does not affect the lower order moments that appear explicitly in the conservation equations, higher order approximations to the Boltzmann-BGK can be achieved by using more velocities in the quadrature. In general, a two dimensional discrete velocity Boltzmann-BGK equation (DVBE) can be written in component form as

$$\frac{\partial f_i}{\partial t} + u_i \frac{\partial f_i}{\partial x} + v_i \frac{\partial f_i}{\partial y} = -\frac{1}{\lambda} (f_i - f_i^{eq}) \quad (14)$$

where f_i is the distribution function for velocity $\boldsymbol{\xi}_i = (u_i, v_i)$. In discretized velocity space, the macroscopic density and momentum are given by

$$\rho = \sum_{j=1}^N f_j \quad (15)$$

$$\rho \mathbf{u} = \sum_{j=1}^N f_j \boldsymbol{\xi}_j \quad (16)$$

where N is the number of discrete velocities. If we define $\mathbf{f} = (f_1, f_2, \dots, f_N)$, we can write Eq. (14) in matrix form as

$$\frac{\partial \mathbf{f}}{\partial t} + \mathbf{A} \frac{\partial \mathbf{f}}{\partial x} + \mathbf{B} \frac{\partial \mathbf{f}}{\partial y} = -\frac{1}{\lambda} (\mathbf{f} - \mathbf{f}^{eq}) \quad (17)$$

where \mathbf{A} and \mathbf{B} are diagonal matrices such that $A_{ii} = u_i$ and $B_{ii} = v_i$.

2.4 LINEAR ANALYSIS OF THE DISCRETE VELOCITY BOLTZMANN-BGK EQUATION

We first investigate the linear waves supported by the discrete velocity Boltzmann-BGK equation. Marié et al. carried out a similar study for a three dimensional discrete velocity Boltzmann-BGK equation [12]. To perform a linear analysis of Eq. (14) or Eq. (17), we first separate the distribution function into a uniform mean flow component and a perturbation component as

$$f_i = \bar{f}_i^{eq} + f'_i \quad (18)$$

where the overbar and the prime sign denote the mean and the perturbation values, respectively. Redefining the right side of Eq. (14) as $g_i(f_j)$ and linearizing it yields

$$g_i(f_j) = g_i(\bar{f}_j^{eq}) + \frac{\partial g_i}{\partial f_j}(\bar{f}_j^{eq}) f'_j + O(f_j'^2) \quad (19)$$

Noting that

$$\frac{\partial g_i}{\partial f_j}(\bar{f}_j^{eq}) = -\frac{1}{\lambda} \left(\delta_{ij} - \frac{\partial f_i^{eq}}{\partial f_j}(\bar{f}_j^{eq}) \right) f'_i \quad (20)$$

and that $g_i(\bar{f}_j^{eq}) = 0$ and plugging back into Eq. (14) gives

$$\frac{\partial f'_i}{\partial t} + \boldsymbol{\xi}_i \cdot \nabla f'_i = -\frac{1}{\lambda} \left(\delta_{ij} - \frac{\partial f_i^{eq}}{\partial f_j}(\bar{f}_j^{eq}) \right) f'_i \quad (21)$$

The two dimensional form of the above can be written in matrix form as

$$\frac{\partial \mathbf{f}'}{\partial t} + \mathbf{A} \frac{\partial \mathbf{f}'}{\partial x} + \mathbf{B} \frac{\partial \mathbf{f}'}{\partial y} = -\frac{1}{\lambda} (\mathbf{I} - \mathbf{J}) \mathbf{f}' \quad (22)$$

where \mathbf{I} is the identity matrix, \mathbf{J} is defined by $J_{ij} = \frac{\partial f_i^{eq}}{\partial f_j}(\bar{f}_j^{eq})$, and matrices \mathbf{A} and \mathbf{B} are the same as given in (17). We look for plane wave solutions $\mathbf{f}'(\mathbf{x}, t) = \hat{\mathbf{f}} e^{i\mathbf{k} \cdot \mathbf{x} - i\omega t}$ and we obtain an eigenvalue problem for ω with given values of k_x and k_y , as follows:

$$-i\omega \hat{\mathbf{f}} + ik_x \mathbf{A} \hat{\mathbf{f}} + ik_y \mathbf{B} \hat{\mathbf{f}} = -\frac{1}{\lambda} (\mathbf{I} - \mathbf{J}) \hat{\mathbf{f}} \quad (23)$$

or equivalently

$$\omega \hat{\mathbf{f}} = \mathbf{M} \hat{\mathbf{f}}; \quad \mathbf{M} := k_x \mathbf{A} + k_y \mathbf{B} - \frac{i}{\lambda} (\mathbf{I} - \mathbf{J}) \quad (24)$$

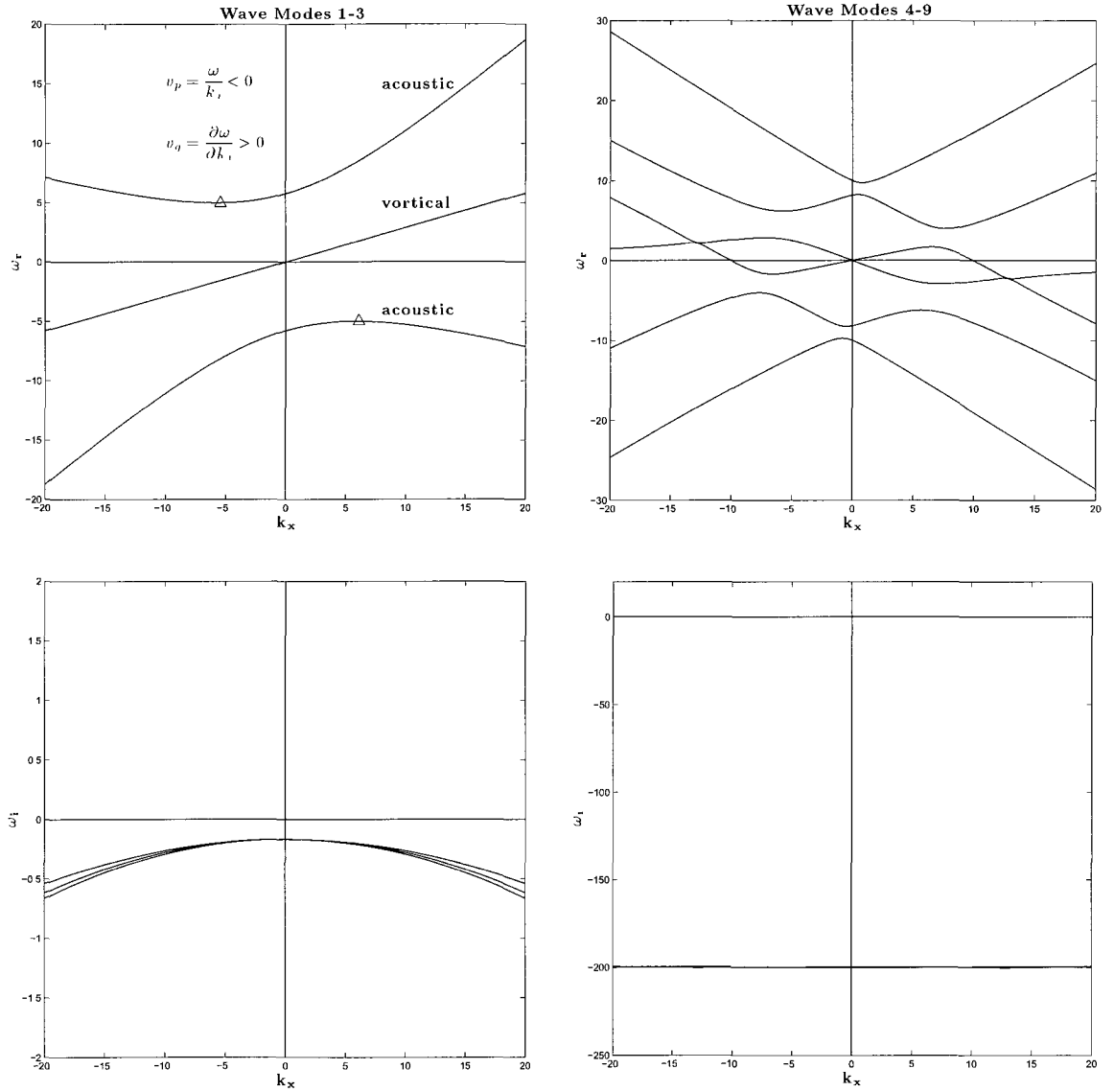


Fig. 2: Dispersion relations of all linear waves supported by Eqs. (24), (25), (26), and D2Q9.

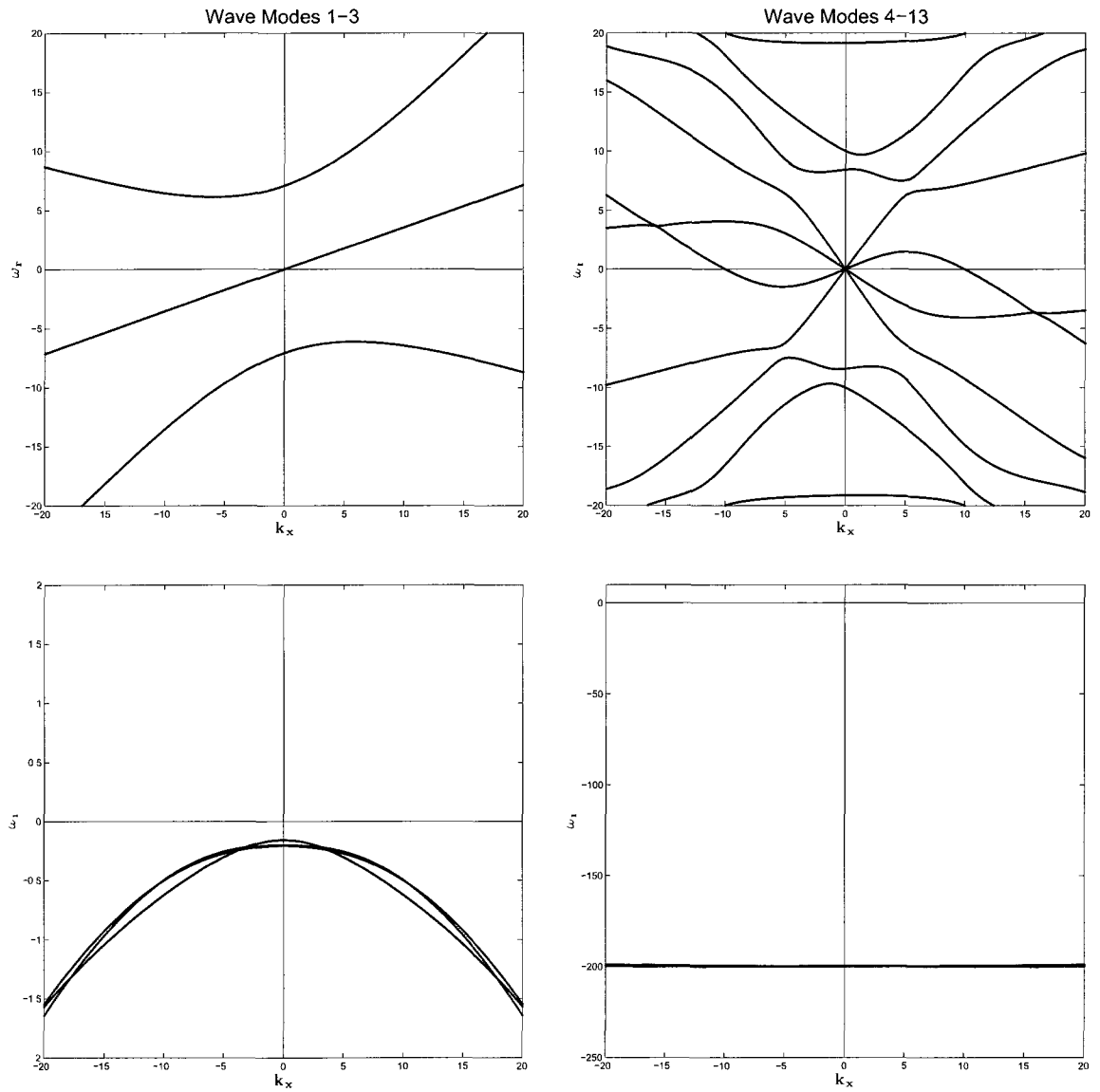


Fig. 3: Dispersion relations of all linear waves supported by Eqs. (24), (25), (26), and D2Q13.

The eigenvalue problem in Eq. (24) will be solved numerically with MATLAB. Using the D2Q9 model as an example, Figure 2 shows the dispersion relations of ω v.s. k_x for all the nine wave modes, with $k_y = 10$, $\lambda = 0.005$ and the mean flow velocity $U_0 = 0.5c_s$. The nine eigenvalues shown can be divided into two groups. One group of modes, shown in the left side of Figure 2, consist of three hydrodynamic waves, namely the two acoustic modes and one vortical mode. The imaginary parts of the three modes are negative, showing a damping effect of the viscosity in the BGK model. The other group of modes, shown on the right side of Figure 2, have significantly higher damping rates.

The dispersion relations of the D2Q13 [69, 70] model illustrated in Figure 3 have a similar behavior, with the ten wave modes shown on the right side of the figure having much higher damping rates than the three hydrodynamic waves shown on the left of the figure. It has been verified that dispersion relations of the three hydrodynamic waves, for the real part of ω , follow closely the curves given by

$$D_a(\omega, k_x, k_y) = (\omega - U_0 k_x)^2 - c_s^2(k_x^2 + k_y^2) = 0 \quad (25)$$

for the acoustic waves and

$$D_v(\omega, k_x, k_y) = \omega - U_0 k_x = 0 \quad (26)$$

for the vortical wave. These are the dispersion relations for the linearized Euler equations. These findings are similar to those reported in Ref. [12].

As in the case of Euler equations [39, 40, 71, 72], the acoustic wave modes of the DVBE as those shown in Figures 2 and 3 exhibit inconsistent phase and group velocities when the mean velocity U_0 is not zero. The phase velocity, defined as the ratio of frequency to wavenumber ($v_p = \frac{\omega}{k_x}$), is positive in quadrants I and III and negative in quadrants II and IV. The group velocity, defined as the change in frequency with respect to the change in wavenumber ($v_g = \frac{\partial \omega}{\partial k_x}$), is positive when the slope of the acoustic curve is positive and negative when the slope is negative. The symbols in Figure 2 denote the location where the group velocity is zero indicating that parts of the dispersion curves have inconsistent phase and group velocities, namely, a negative phase velocity but a positive group velocity for the waves that lie between the location of the symbol and the vertical axis.

Because a complex change of variables is involved in deriving the PML equations [39,47], the numerical stability of the absorbing layers requires that the inconsistencies in phase and group velocity be corrected. Otherwise, when the complex change of variables is applied, the resulting PML equations will produce exponentially growing solutions.

However, it has been demonstrated in previous studies that these inconsistencies in the phase and group velocities can be corrected by a proper linear space-time transformation of the form [39,40,71,72]

$$\bar{x} = x, \quad \bar{y} = y, \quad \bar{t} = t + \beta x \quad (27)$$

where β is defined by

$$\beta = -\frac{k_x^*}{\omega^*} \quad (28)$$

in which k_x^* and ω^* are the roots of

$$D_a(\omega^*, k_x^*, k_y) = 0, \quad \text{and} \quad \frac{\partial D_a}{\partial k_x}(\omega^*, k_x^*, k_y) = 0 \quad (29)$$

By Eqs. (25) and (29), we find that, for any k_y , $\omega^* = [(U_0^2 - c_s^2)]/U_0 k_x^*$ which leads to

$$\beta = \frac{U_0}{c_s^2 - U_0^2} \quad (30)$$

The corresponding transformed wavenumbers and frequency are

$$\bar{k}_x = k_x + \frac{U_0}{c_s^2 - U_0^2} \omega, \quad \bar{k}_y = k_y, \quad \bar{\omega} = \omega \quad (31)$$

The updated acoustic and vortical dispersion relations given by

$$D_a(\bar{\omega}, \bar{k}_x, \bar{k}_y) = \frac{c_s^2}{c_s^2 - U_0^2} \bar{\omega}^2 - (c_s^2 - U_0^2) \bar{k}_x^2 - c_s^2 \bar{k}_y^2 = 0 \quad (32)$$

$$D_v(\bar{\omega}, \bar{k}_x, \bar{k}_y) = \frac{c_s^2}{c_s^2 - U_0^2} \bar{\omega} - U_0 \bar{k}_x = 0 \quad (33)$$

indicate that the phase and group velocities are now consistent and that the PML change of variables will not cause instability.

For the second group of waves, shown on the right side of Figures 2 and 3, the inconsistencies of phase and group velocities are also found but cannot be corrected

easily. However, with intrinsic high damping rates associated with these modes, the application of PML change of variables may not cause instability when the PML absorption coefficients are not exceedingly large. This is confirmed in the stability analysis done in the next chapter.

CHAPTER 3

THE PERFECTLY MATCHED LAYER (PML) METHOD

3.1 INTRODUCTION TO PERFECTLY MATCHED LAYERS

Numerous problems that arise in the physical sciences and have significant technological implications involve the propagation of waves. Many of these problems, as those arising in CAA, also involve the propagation of waves in unbounded or very large domains. Truncation of the physical domain is then necessary for numerical simulation because the size of the problem must be reduced to a level that our current computational resources can manage [17, 73].

The numerical boundaries resulting from the truncation of the physical domain pose a problem if proper boundary conditions are not specified because waves will reflect off of them back into the computational domain to invalidate the solution. An effective nonreflecting boundary condition will ideally have the same effect on the interior solution as if no boundaries were present. From a practical point of view, we would like to reduce reflections on the boundary to within a margin of error. The Perfectly Matched Layer (PML) method has already been shown to be an effective tool for constructing nonreflecting boundary conditions for the Euler and Navier-Stokes equations [40, 41, 51, 74]. In view of this, the purpose of the present work will be to extend the PML methodology to the discrete velocity Boltzmann-BGK equation for use in the field of CAA.

In essence, the PML method is an analytic continuation of the wave equation into complex coordinates followed by a coordinate transformation back to real coordinates. This process changes propagating waves into exponentially decaying ones inside the PML layers. As seen in Figure 3.1, artificial regions, called "perfectly matched layers" are added on the boundaries of the computational domain. In these regions, new equations are derived to damp outgoing waves so they will not reach the boundaries and thus will not be able to reflect back. The equations for the PML regions are specifically designed to match the interior governing equations so that waves incident on the PML do not reflect at the interface.

As we saw from the analysis of the dispersion relations supported by the discrete velocity Boltzmann-BGK equation, in the case of flows with non-zero mean convective velocity, there is an inconsistency between the phase and group velocity

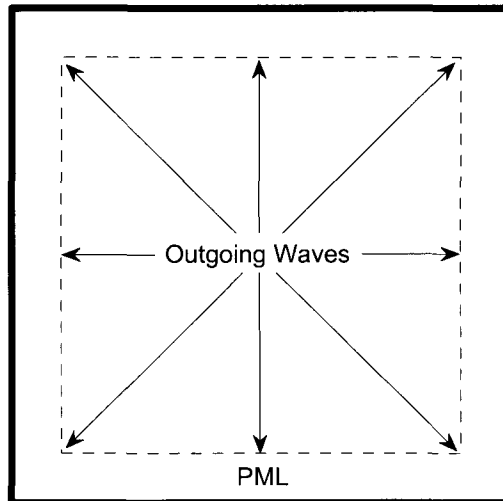


Fig. 4: Diagram of PML domains for a rectangular domain. Dashed lines indicate the interface between the PML domains and interior.

which can result in unstable PML equations if left uncorrected. This is the same inconsistency that is found in the dispersion relations of the Euler equations. A well chosen space-time transformation has been shown to correct the inconsistency for the Euler equations. Since the dispersion relations for the three hydrodynamic waves supported by the discrete velocity Boltzmann-BGK equations considered for the present study are the same as those supported by the Euler equations, we have reason to expect that the same space-time transformation will work here as well.

The derivation of the PML equations for the discrete velocity Boltzmann-BGK equation is a four fold process. The first step in the derivation is to apply the space-time transformation to the discrete velocity Boltzmann equation. To see why this is necessary, consider the change of variables required in deriving the PML equations for an absorbing layer in the x -direction:

$$x \rightarrow x + \frac{i}{\omega} \int_{x_0}^x \sigma_x dx \quad (34)$$

where σ_x is the absorption coefficient defined as a positive function of x in the PML

domain and zero in the interior domain. When this change of variable is applied to a linear solution of the form

$$u(x, t) = e^{i(k_r x - \omega t)} \quad (35)$$

we obtain

$$u(x, t) = e^{-\frac{k_x}{\omega} \int_{x_0}^x \sigma_x dx} e^{i(k_r x - \omega t)} \quad (36)$$

In the equation above, the term $\frac{k_x}{\omega}$ is the reciprocal of phase velocity so its sign will be the sign of the phase velocity. Because σ_x is a positive function of x , the sign of the integral $\int_{x_0}^x \sigma_x dx$ is determined by the increase or decrease in x and is related to the group velocity. A positive group velocity represents a right-going wave and an increase in x , whereas a negative group velocity represents a left-going wave and a decrease in x . When the phase and group velocities have the same sign, the sign of the term $\frac{k_x}{\omega} \int_{x_0}^x \sigma_x dx$ is positive and the exponential term $e^{-\frac{k_x}{\omega} \int_{x_0}^x \sigma_x dx}$ will have a negative power resulting in exponentially decaying solutions. On the other hand, if the phase and group velocities have opposite signs, the exponential term will have a positive power resulting in exponentially growing solutions and thus an unstable PML.

The transformed discrete velocity Boltzmann-BGK equation is then written in the frequency domain where we apply the PML complex change of variables:

$$x \rightarrow x + \frac{i}{\omega} \int_{x_0}^x \sigma_x dx; \quad y \rightarrow y + \frac{i}{\omega} \int_{y_0}^y \sigma_y dy \quad (37)$$

where σ_x and σ_y are the absorption coefficients in the x and y -directions respectively. Upon converting the resulting equations back to the original time and space, the equations for the PML regions emerge.

Perfectly Matched Layer (PML) absorbing boundary conditions for the lattice Boltzmann equation have been studied previously by Najafiyazdi and Mongeau [52]. However, this derivation has limited applicability because the absorption coefficients are assumed to be equal for the PML equations to be stable.

The approach we take in deriving the PML equations in the next section is applicable to any discrete velocity Boltzmann-BGK model, provided that the model supports accurate hydrodynamics. More specifically, we will derive the PML equations in both split and unsplit variables for the discrete velocity Boltzmann-BGK

equation in two and three dimensions for the case of horizontal mean flow.

3.2 PROPOSED TWO-DIMENSIONAL PML EQUATIONS

3.2.1 Derivation of Unsplit PML Equations

To obtain the PML equations, we first assume a mean flow with velocity U_0 and we decompose the distribution functions into a uniform mean flow component and a perturbation component

$$\mathbf{f} = \bar{\mathbf{f}} + \mathbf{f}' \quad (38)$$

where the overbar and the prime sign denote the steady mean and the perturbation values, respectively, and the function \mathbf{f} satisfies the discrete velocity Boltzmann-BGK equation (17). We also assume that $\bar{\mathbf{f}} = \bar{\mathbf{f}}^{eq}$ and the mean flow equilibrium distribution function, $\bar{\mathbf{f}}$, satisfies the following time-independent equation

$$\mathbf{A} \frac{\partial \bar{\mathbf{f}}}{\partial x} + \mathbf{B} \frac{\partial \bar{\mathbf{f}}}{\partial y} = 0 \quad (39)$$

We will now derive the absorbing equation for the perturbation distribution function \mathbf{f}' :

$$\frac{\partial \mathbf{f}'}{\partial t} + \mathbf{A} \frac{\partial(\mathbf{f} - \bar{\mathbf{f}})}{\partial x} + \mathbf{B} \frac{\partial(\mathbf{f} - \bar{\mathbf{f}})}{\partial y} = -\frac{1}{\lambda} (\mathbf{f} - \mathbf{f}^{eq}) \quad (40)$$

The first step in our derivation will be to correct the inconsistency in phase and group velocity so that we do not obtain unstable PML equations. To accomplish this, we follow the work of Hu and we apply the space-time transformation [41]

$$\bar{t} = t + \beta x \quad (41)$$

where β is given in Eq. (30). Equation (40) becomes

$$\frac{\partial \mathbf{f}'}{\partial \bar{t}} + \beta \mathbf{A} \frac{\partial(\mathbf{f} - \bar{\mathbf{f}})}{\partial \bar{t}} + \mathbf{A} \frac{\partial(\mathbf{f} - \bar{\mathbf{f}})}{\partial x} + \mathbf{B} \frac{\partial(\mathbf{f} - \bar{\mathbf{f}})}{\partial y} = -\frac{1}{\lambda} (\mathbf{f} - \mathbf{f}^{eq}) \quad (42)$$

Writing the above in the frequency domain gives

$$(-i\omega) \hat{\mathbf{f}}' + (-i\omega)\beta \mathbf{A} \widehat{(\mathbf{f} - \bar{\mathbf{f}})} + \mathbf{A} \frac{\partial \widehat{(\mathbf{f} - \bar{\mathbf{f}})}}{\partial x} + \mathbf{B} \frac{\partial \widehat{(\mathbf{f} - \bar{\mathbf{f}})}}{\partial y} = -\frac{1}{\lambda} \widehat{(\mathbf{f} - \mathbf{f}^{eq})} \quad (43)$$

Y_{\max}	$\sigma_x \neq 0$ $\sigma_y \neq 0$	$\sigma_x = 0$ $\sigma_y \neq 0$	$\sigma_x \neq 0$ $\sigma_y \neq 0$
	$\sigma_x \neq 0$ $\sigma_y = 0$	DVBE	$\sigma_x \neq 0$ $\sigma_y = 0$
Y_{\min}	$\sigma_x \neq 0$ $\sigma_y \neq 0$	$\sigma_x = 0$ $\sigma_y \neq 0$	$\sigma_x \neq 0$ $\sigma_y \neq 0$
	X_{\min}		X_{\max}

Fig. 5: Illustration of absorption coefficients for PML domains.

At this point, we apply the PML complex change of variables given in Eq. (37) with absorption coefficients σ_x and σ_y as illustrated in Figure 5. After the PML change of variables, we have

$$\begin{aligned}
& (-i\omega)\hat{\mathbf{f}}' + (-i\omega)\beta\mathbf{A}(\widehat{\mathbf{f} - \bar{\mathbf{f}}}) + \mathbf{A} \frac{1}{1 + \frac{i\sigma_x}{\omega}} \frac{\partial(\widehat{\mathbf{f} - \bar{\mathbf{f}}})}{\partial x} \\
& + \mathbf{B} \frac{1}{1 + \frac{i\sigma_y}{\omega}} \frac{\partial(\widehat{\mathbf{f} - \bar{\mathbf{f}}})}{\partial y} = -\frac{1}{\lambda}(\widehat{\mathbf{f} - \mathbf{f}^{eq}}) \tag{44}
\end{aligned}$$

To write the above in the time-domain, we multiply Eq. (44) by $(1 + \frac{i\sigma_x}{\omega}) (1 + \frac{i\sigma_y}{\omega})$ to obtain

$$\begin{aligned}
& (-i\omega)\hat{\mathbf{f}}' + (\sigma_x + \sigma_y)\hat{\mathbf{f}}' + \sigma_x\sigma_y \frac{i}{\omega}\hat{\mathbf{f}}' + (-i\omega)\beta\mathbf{A}(\widehat{\mathbf{f} - \bar{\mathbf{f}}}) + (\sigma_x + \sigma_y)\beta\mathbf{A}(\widehat{\mathbf{f} - \bar{\mathbf{f}}}) \\
& + \sigma_x\sigma_y \frac{i}{\omega}\beta\mathbf{A}(\widehat{\mathbf{f} - \bar{\mathbf{f}}}) + \mathbf{A} \left(1 + \frac{i\sigma_y}{\omega}\right) \frac{\partial(\widehat{\mathbf{f} - \bar{\mathbf{f}}})}{\partial x} + \mathbf{B} \left(1 + \frac{i\sigma_x}{\omega}\right) \frac{\partial(\widehat{\mathbf{f} - \bar{\mathbf{f}}})}{\partial y}
\end{aligned}$$

$$= -\frac{1}{\lambda} \left(1 + \frac{i\sigma_x}{\omega} + \frac{i\sigma_y}{\omega} - \frac{\sigma_x\sigma_y}{\omega^2} \right) \widehat{(\mathbf{f} - \mathbf{f}^{eq})} \quad (45)$$

We can write the above back in the time domain by introducing auxiliary variables \mathbf{q} , \mathbf{r}_1 , and \mathbf{r}_2 such that

$$\frac{\partial \mathbf{q}}{\partial t} = \mathbf{f} - \bar{\mathbf{f}}, \quad \frac{\partial \mathbf{r}_1}{\partial t} = \mathbf{f} - \mathbf{f}^{eq}, \quad \frac{\partial \mathbf{r}_2}{\partial t} = \mathbf{r}_1 \quad (46)$$

In the original physical space and time, the PML absorbing equation can finally be written as

$$\begin{aligned} \frac{\partial \mathbf{f}}{\partial t} + \mathbf{A} \frac{\partial \mathbf{f}}{\partial x} + \mathbf{B} \frac{\partial \mathbf{f}}{\partial y} + \sigma_y \mathbf{A} \frac{\partial \mathbf{q}}{\partial x} + \sigma_x \mathbf{B} \frac{\partial \mathbf{q}}{\partial y} + (\sigma_x + \sigma_y) (\mathbf{f} - \bar{\mathbf{f}}) + \sigma_x \sigma_y \mathbf{q} \\ + \sigma_x \beta \mathbf{A} [(\mathbf{f} - \bar{\mathbf{f}}) + \sigma_y \mathbf{q}] = -\frac{1}{\lambda} (\mathbf{f} - \mathbf{f}^{eq}) - \frac{1}{\lambda} (\sigma_x + \sigma_y) \mathbf{r}_1 - \frac{1}{\lambda} \sigma_x \sigma_y \mathbf{r}_2 \end{aligned} \quad (47)$$

Equations (46) and (47) are the time domain PML equations to be used in the PML domains. They are given in terms of the distribution functions and auxiliary variables.

3.2.2 Formulation of Split PML Equations

To derive the split PML equations, we split Eq. (44) and we introduce auxiliary variables \mathbf{q}_1 , \mathbf{q}_2 , and \mathbf{q}_3 which satisfy the following equations in the frequency domain

$$(-i\omega)\hat{\mathbf{q}}_1 + (-i\omega)\beta \mathbf{A} \widehat{(\mathbf{f} - \bar{\mathbf{f}})} + \frac{1}{1 + \frac{i\sigma_x}{\omega}} \mathbf{A} \frac{\partial \widehat{(\mathbf{f} - \bar{\mathbf{f}})}}{\partial x} = 0 \quad (48)$$

$$(-i\omega)\hat{\mathbf{q}}_2 + \frac{1}{1 + \frac{i\sigma_y}{\omega}} \mathbf{B} \frac{\partial \widehat{(\mathbf{f} - \bar{\mathbf{f}})}}{\partial y} = 0 \quad (49)$$

$$(-i\omega)\hat{\mathbf{q}}_3 = -\frac{1}{\lambda} \widehat{(\mathbf{f} - \mathbf{f}^{eq})} \quad (50)$$

We can recover Eq. (44) for $\hat{\mathbf{f}}'$ since $\hat{\mathbf{f}}' = \hat{\mathbf{q}}_1 + \hat{\mathbf{q}}_2 + \hat{\mathbf{q}}_3$. Multiplying Eqs. (48) and (49) by $(1 + \frac{i\sigma_x}{\omega})$ and $(1 + \frac{i\sigma_y}{\omega})$ respectively, we obtain

$$(-i\omega)\hat{\mathbf{q}}_1 + \sigma_x \hat{\mathbf{q}}_1 + \sigma_x \beta \mathbf{A} \widehat{(\mathbf{f} - \bar{\mathbf{f}})} + (-i\omega)\beta \mathbf{A} \widehat{(\mathbf{f} - \bar{\mathbf{f}})} + \mathbf{A} \frac{\partial \widehat{(\mathbf{f} - \bar{\mathbf{f}})}}{\partial x} = 0 \quad (51)$$

$$(-i\omega)\hat{\mathbf{q}}_2 + \sigma_y \hat{\mathbf{q}}_2 + \mathbf{B} \frac{\partial(\widehat{\mathbf{f}} - \bar{\mathbf{f}})}{\partial y} = 0 \quad (52)$$

$$(-i\omega)\hat{\mathbf{q}}_3 = -\frac{1}{\lambda} (\widehat{\mathbf{f}} - \mathbf{f}^{eq}) \quad (53)$$

Upon reverting the equations above back to the original time domain, we have

$$\frac{\partial \mathbf{q}_1}{\partial t} + \sigma_x \mathbf{q}_1 + \sigma_x \beta \mathbf{A}(\mathbf{f} - \bar{\mathbf{f}}) + \mathbf{A} \frac{\partial(\mathbf{f} - \bar{\mathbf{f}})}{\partial x} = 0 \quad (54)$$

$$\frac{\partial \mathbf{q}_2}{\partial t} + \sigma_y \mathbf{q}_2 + \mathbf{B} \frac{\partial(\mathbf{f} - \bar{\mathbf{f}})}{\partial y} = 0 \quad (55)$$

$$\frac{\partial \mathbf{q}_3}{\partial t} = -\frac{1}{\lambda} (\mathbf{f} - \mathbf{f}^{eq}) \quad (56)$$

By adding Eqs. (54), (55), and (56) we obtain the equation for \mathbf{f} and a second, split, PML set of equations

$$\frac{\partial \mathbf{f}}{\partial t} + \mathbf{A} \frac{\partial \mathbf{f}}{\partial x} + \mathbf{B} \frac{\partial \mathbf{f}}{\partial y} + \sigma_x \mathbf{q}_1 + \sigma_y \mathbf{q}_2 + \sigma_x \beta \mathbf{A}(\mathbf{f} - \bar{\mathbf{f}}) = -\frac{1}{\lambda} (\mathbf{f} - \mathbf{f}^{eq}) \quad (57)$$

$$\frac{\partial \mathbf{q}_1}{\partial t} + \sigma_x \mathbf{q}_1 + \sigma_x \beta \mathbf{A}(\mathbf{f} - \bar{\mathbf{f}}) + \mathbf{A} \frac{\partial(\mathbf{f} - \bar{\mathbf{f}})}{\partial x} = 0 \quad (58)$$

$$\frac{\partial \mathbf{q}_2}{\partial t} + \sigma_y \mathbf{q}_2 + \mathbf{B} \frac{\partial(\mathbf{f} - \bar{\mathbf{f}})}{\partial y} = 0 \quad (59)$$

In component form we have

$$\frac{\partial f_i}{\partial t} + u_i \frac{\partial f_i}{\partial x} + v_i \frac{\partial f_i}{\partial y} + \sigma_x q_{1i} + \sigma_y q_{2i} + \sigma_x \beta u_i (f_i - \bar{f}_i) = -\frac{1}{\lambda} (f_i - f_i^{eq}) \quad (60)$$

$$\frac{\partial q_{1i}}{\partial t} + \sigma_x q_{1i} + \sigma_x \beta u_i (f_i - \bar{f}_i) + u_i \frac{\partial(f_i - \bar{f}_i)}{\partial x} = 0 \quad (61)$$

$$\frac{\partial q_{2i}}{\partial t} + \sigma_y q_{2i} + v_i \frac{\partial(f_i - \bar{f}_i)}{\partial y} = 0 \quad (62)$$

We note that the split formulation does not require additional spatial derivatives. On the other hand, the unsplit formulation ensures that $\mathbf{f} = \bar{\mathbf{f}}$ when $\frac{\partial \mathbf{q}}{\partial t} = 0$.

3.2.3 Linear Stability of Two-Dimensional PML Equations

To assess the stability of the absorbing boundary conditions we proposed in the previous section, we investigate the linear stability of the PML equations. We only need to consider the stability of the split formulation since the eigen solutions of the unsplit formulation are equivalent to those of the split formulation. We begin our analysis by linearizing the split PML Eqs. (57)-(59) to obtain

$$\frac{\partial \mathbf{f}'}{\partial t} + \mathbf{A} \frac{\partial \mathbf{f}'}{\partial x} + \mathbf{B} \frac{\partial \mathbf{f}'}{\partial y} + \sigma_x \mathbf{q}_1 + \sigma_y \mathbf{q}_2 + \sigma_x \beta \mathbf{A} \mathbf{f}' = -\frac{1}{\lambda} (\mathbf{I} - \mathbf{J}) \mathbf{f}' \quad (63)$$

$$\frac{\partial \mathbf{q}_1}{\partial t} + \sigma_x \mathbf{q}_1 + \sigma_x \beta \mathbf{A} \mathbf{f}' + \mathbf{A} \frac{\partial \mathbf{f}'}{\partial x} = 0 \quad (64)$$

$$\frac{\partial \mathbf{q}_2}{\partial t} + \sigma_y \mathbf{q}_2 + \mathbf{B} \frac{\partial \mathbf{f}'}{\partial y} = 0 \quad (65)$$

where \mathbf{A} , \mathbf{B} , \mathbf{I} and \mathbf{J} are as previously defined. Now we substitute into the equations above a solution of the form

$$\begin{pmatrix} \mathbf{f}' \\ \mathbf{q}_1 \\ \mathbf{q}_2 \end{pmatrix} = \begin{pmatrix} \hat{\mathbf{f}} \\ \hat{\mathbf{q}}_1 \\ \hat{\mathbf{q}}_2 \end{pmatrix} e^{i(\mathbf{k} \cdot \mathbf{x} - \omega t)} \quad (66)$$

which can be written in the more compact form

$$\mathbf{F} = \hat{\mathbf{F}} e^{i(\mathbf{k} \cdot \mathbf{x} - \omega t)} \quad (67)$$

where $\hat{\mathbf{F}}$ is assumed constant. This gives the following system

$$\frac{\partial \mathbf{F}}{\partial t} + \begin{pmatrix} \mathbf{A} & 0 & 0 \\ \mathbf{A} & 0 & 0 \\ 0 & 0 & 0 \end{pmatrix} \frac{\partial \mathbf{F}}{\partial x} + \begin{pmatrix} \mathbf{B} & 0 & 0 \\ 0 & 0 & 0 \\ \mathbf{B} & 0 & 0 \end{pmatrix} \frac{\partial \mathbf{F}}{\partial y} + \begin{pmatrix} \sigma_x \beta \mathbf{A} + \frac{1}{\lambda} (\mathbf{I} - \mathbf{J}) & \sigma_x \mathbf{I} & \sigma_y \mathbf{I} \\ \sigma_x \beta \mathbf{A} & \sigma_x \mathbf{I} & 0 \\ 0 & 0 & \sigma_y \mathbf{I} \end{pmatrix} \mathbf{F} = 0 \quad (68)$$

Noting that

$$\frac{\partial \mathbf{F}}{\partial t} = -\imath\omega \mathbf{F} \quad (69)$$

$$\frac{\partial \mathbf{F}}{\partial x} = \imath k_x \mathbf{F} \quad (70)$$

$$\frac{\partial \mathbf{F}}{\partial y} = \imath k_y \mathbf{F} \quad (71)$$

we can see that the system reduces to

$$\begin{pmatrix} (k_x - \imath\sigma_x\beta)\mathbf{A} + k_y\mathbf{B} - \frac{\imath}{\lambda}(\mathbf{I} - \mathbf{J}) & -\imath\sigma_x\mathbf{I} & -\imath\sigma_y\mathbf{I} \\ (k_x - \imath\sigma_x\beta)\mathbf{A} & -\imath\sigma_x\mathbf{I} & 0 \\ k_y\mathbf{B} & 0 & -\imath\sigma_y\mathbf{I} \end{pmatrix} \hat{\mathbf{F}} = \omega \hat{\mathbf{F}} \quad (72)$$

or simply,

$$\mathbf{M}_1 \hat{\mathbf{F}} = \omega \hat{\mathbf{F}} \quad (73)$$

if we let \mathbf{M}_1 be the matrix in Eq. (72). For a given discrete velocity set, we can define the matrices \mathbf{A} and \mathbf{B} , and for given mean flow U_0 , we can compute matrix \mathbf{J} . Then it is not hard to see that for constant σ_x and σ_y , Eq. (73) is an eigenvalue problem for ω , for given values of k_x and k_y . The occurrence of any eigenvalue ω with a positive imaginary part ω_i will indicate instability because the wave amplitude will grow exponentially in time. On the other hand, if all the eigenvalues have nonpositive imaginary parts, then the system is dynamically stable.

Using the D2Q9 model as an example, we examine the eigenvalues generated for relaxation time $\lambda = 0.00011$ by the x , y , and corner layers. Although we would need to consider the range of wavenumbers $|k_x|, |k_x| \leq \infty$ for the continuous equations, the Nyquist limit for finite difference schemes prescribes only wavenumbers $|k_x| \leq \frac{\pi}{\Delta x}$ so that truncating the range of wavenumbers to $|k_x|, |k_x| \leq 20$ should be valid for most practical choices of Δx . To examine the stability of the x -layer, we consider the range of Mach numbers $0 \leq M = U_0/c_s \leq 0.7$ and absorption coefficients $0 \leq \sigma_x \leq 10$. The upper bound for the Mach number is due to the fact that our applications are for low Mach number flows. In Figure 6 we show the highest contour levels of maximum imaginary parts, ω_i , of eigenvalues for the x -layer over varying Mach number M and absorption coefficient σ_x . All ω_i are in the order of 10^{-11} or smaller and thus practically zero which suggests that the x -layer equations are stable. The highest level contours of the resulting maximum ω_i for the y -layer equations are

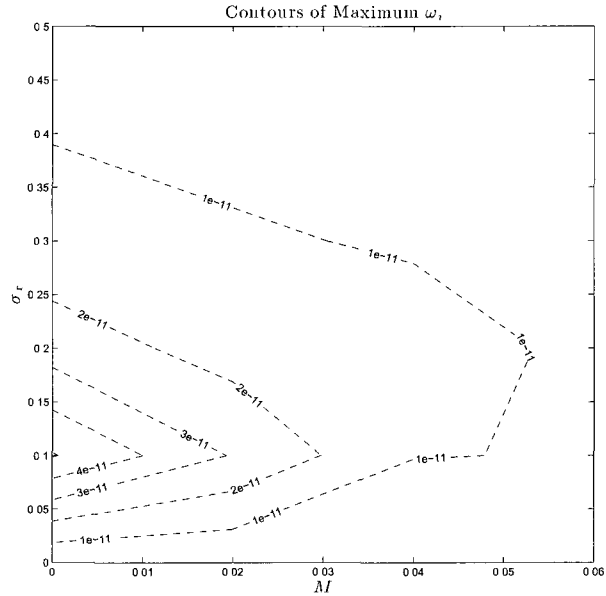


Fig. 6: Highest contour levels of maximum imaginary parts, ω_i , of eigenvalues for the x -layer over varying Mach numbers and absorption coefficient σ_x .

displayed in Figure 7 for varying Mach number $0 \leq M \leq 0.7$, absorption coefficient $0 \leq \sigma_y \leq 10$, and three different ranges of wavenumbers. We can see that as the range of wavenumbers is increased, the maximum value of ω_i also increases but slowly. This suggests that the large values of ω_i are caused by the larger wavenumbers. Although the ω_i are not small enough to be considered zero, they are small enough to be easily overcome by the intrinsic damping of the numerical schemes used to solve the PML equations or by numerical filtering. Figure 8 shows the contours for the maximum ω_i for the corner layer for fixed Mach numbers $M = 0.2$ and $M = 0.7$, over varying absorption coefficients σ_x and σ_y , and varying ranges of wavenumbers. As in the case of the y -layer, the maximum ω_i are small enough that they should be easily overcome by the damping of the finite difference schemes or by numerical filtering as will be demonstrated in numerical examples.

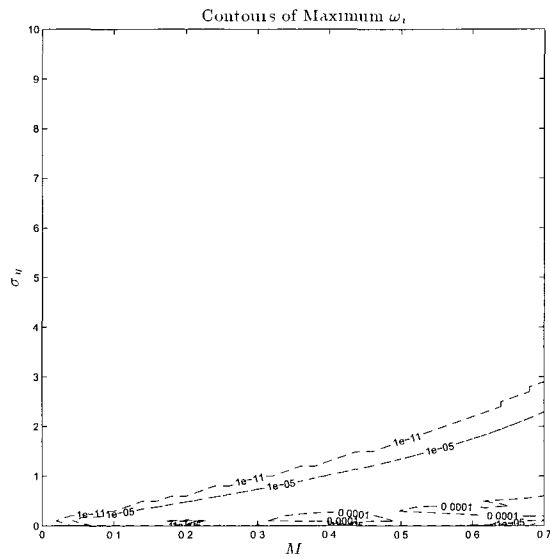
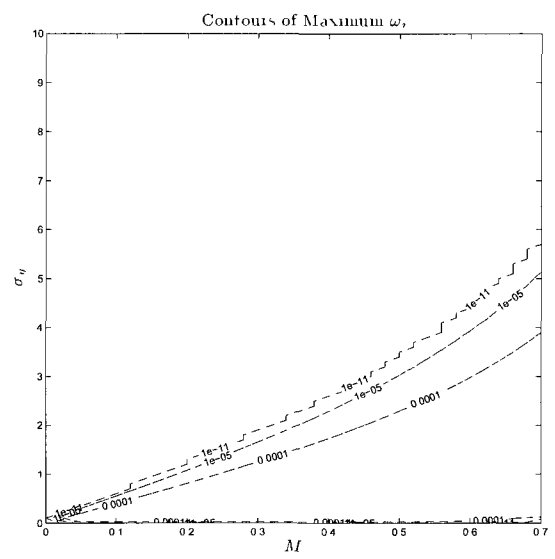
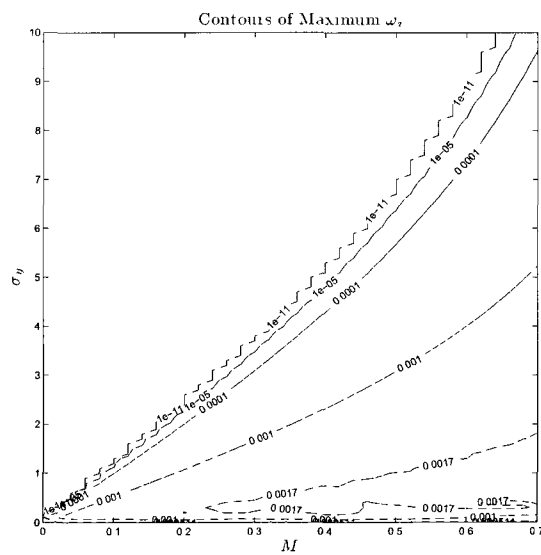
(a) $|kx, ky| \leq 5$ (b) $|kx, ky| \leq 10$ (c) $|kx, ky| \leq 20$

Fig. 7: Contours of maximum imaginary parts, ω_i , of eigenvalues for the y -layer over varying Mach numbers and absorption coefficient σ_y .

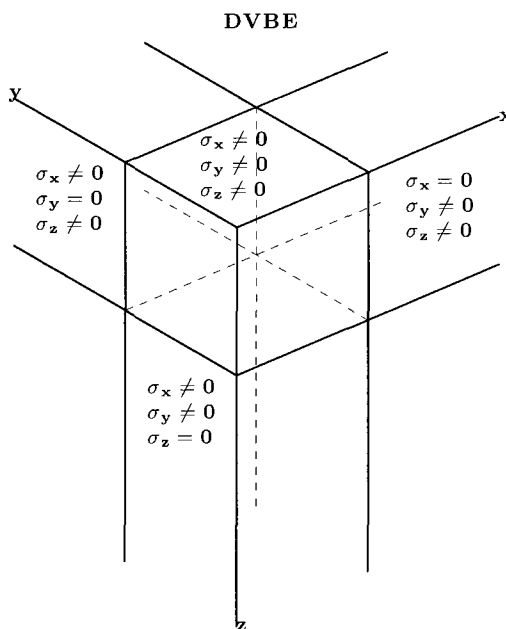


Fig. 9: Diagram of PML domains in three dimensions.

3.3 PROPOSED THREE-DIMENSIONAL PML EQUATIONS

3.3.1 Unsplit PML Formulation

To derive the PML equations in three dimensions, again we assume a mean flow with velocity U_0 and we decompose the distribution functions into a uniform mean flow component and a perturbation component

$$\mathbf{f} = \bar{\mathbf{f}} + \mathbf{f}' \quad (74)$$

where the overbar and the prime sign denote the steady mean and the perturbation values, respectively. We also assume that $\bar{\mathbf{f}} = \bar{\mathbf{f}}^{eq}$ and the mean flow equilibrium distribution function, $\bar{\mathbf{f}}$, satisfies the time-independent equation

$$\mathbf{A} \frac{\partial \bar{\mathbf{f}}}{\partial x} + \mathbf{B} \frac{\partial \bar{\mathbf{f}}}{\partial y} + \mathbf{C} \frac{\partial \bar{\mathbf{f}}}{\partial z} = 0 \quad (75)$$

We will derive the absorbing equation for the perturbation distribution function \mathbf{f}' :

$$\frac{\partial \mathbf{f}'}{\partial t} + \mathbf{A} \frac{\partial(\mathbf{f} - \bar{\mathbf{f}})}{\partial x} + \mathbf{B} \frac{\partial(\mathbf{f} - \bar{\mathbf{f}})}{\partial y} + \mathbf{C} \frac{\partial(\mathbf{f} - \bar{\mathbf{f}})}{\partial z} = -\frac{1}{\lambda} (\mathbf{f} - \mathbf{f}^{eq}) \quad (76)$$

To derive the PML equation for \mathbf{f}' , a space-time transformation is applied first to correct the inconsistency in phase and group velocity

$$\bar{t} = t + \beta x \quad (77)$$

where β is given in Eq. (30). Equation (76) becomes

$$\frac{\partial \mathbf{f}'}{\partial \bar{t}} + \beta \mathbf{A} \frac{\partial(\mathbf{f} - \bar{\mathbf{f}})}{\partial \bar{t}} + \mathbf{A} \frac{\partial(\mathbf{f} - \bar{\mathbf{f}})}{\partial x} + \mathbf{B} \frac{\partial(\mathbf{f} - \bar{\mathbf{f}})}{\partial y} + \mathbf{C} \frac{\partial(\mathbf{f} - \bar{\mathbf{f}})}{\partial z} = -\frac{1}{\lambda} (\mathbf{f} - \mathbf{f}^{eq}) \quad (78)$$

Writing the above in the frequency domain gives

$$\begin{aligned} (-i\omega) \widehat{\mathbf{f}}' + (-i\omega) \beta \mathbf{A} \widehat{(\mathbf{f} - \bar{\mathbf{f}})} + \mathbf{A} \frac{\partial \widehat{(\mathbf{f} - \bar{\mathbf{f}})}}{\partial x} + \mathbf{B} \frac{\partial \widehat{(\mathbf{f} - \bar{\mathbf{f}})}}{\partial y} \\ + \mathbf{C} \frac{\partial \widehat{(\mathbf{f} - \bar{\mathbf{f}})}}{\partial z} = -\frac{1}{\lambda} \widehat{(\mathbf{f} - \mathbf{f}^{eq})} \end{aligned} \quad (79)$$

Now we introduce the PML complex change of variables $x' = (1 + \frac{i\sigma_x}{\omega})x$, $y' = (1 + \frac{i\sigma_y}{\omega})y$, $z' = (1 + \frac{i\sigma_z}{\omega})z$, where σ_x , σ_y , and σ_z are the PML absorption coefficients as illustrated in Figure 9.

$$\begin{aligned} (-i\omega) \widehat{\mathbf{f}}' + (-i\omega) \beta \mathbf{A} \widehat{(\mathbf{f} - \bar{\mathbf{f}})} + \mathbf{A} \frac{1}{1 + \frac{i\sigma_x}{\omega}} \frac{\partial \widehat{(\mathbf{f} - \bar{\mathbf{f}})}}{\partial x} + \mathbf{B} \frac{1}{1 + \frac{i\sigma_y}{\omega}} \frac{\partial \widehat{(\mathbf{f} - \bar{\mathbf{f}})}}{\partial y} \\ + \mathbf{C} \frac{1}{1 + \frac{i\sigma_z}{\omega}} \frac{\partial \widehat{(\mathbf{f} - \bar{\mathbf{f}})}}{\partial z} = -\frac{1}{\lambda} \widehat{(\mathbf{f} - \mathbf{f}^{eq})} \end{aligned} \quad (80)$$

To write the above in the time-domain, we multiply Eq. (80) by $(1 + \frac{i\sigma_x}{\omega}) (1 + \frac{i\sigma_y}{\omega}) (1 + \frac{i\sigma_z}{\omega})$ to obtain

$$\begin{aligned}
& (-i\omega)\hat{\mathbf{f}}' + (\sigma_x + \sigma_y + \sigma_z)\hat{\mathbf{f}}' + \frac{i}{\omega}(\sigma_x\sigma_y + \sigma_x\sigma_z + \sigma_y\sigma_z)\hat{\mathbf{f}}' - \frac{1}{\omega^2}\sigma_x\sigma_y\sigma_z\hat{\mathbf{f}}' \\
& + (-i\omega)\beta\mathbf{A}(\widehat{\mathbf{f} - \bar{\mathbf{f}}}) + (\sigma_x + \sigma_y + \sigma_z)\beta\mathbf{A}(\widehat{\mathbf{f} - \bar{\mathbf{f}}}) \\
& + \frac{i}{\omega}(\sigma_x\sigma_y + \sigma_x\sigma_z + \sigma_y\sigma_z)\beta\mathbf{A}(\widehat{\mathbf{f} - \bar{\mathbf{f}}}) - \frac{1}{\omega^2}\sigma_x\sigma_y\sigma_z\beta\mathbf{A}(\widehat{\mathbf{f} - \bar{\mathbf{f}}}) \\
& + \mathbf{A}\frac{\partial(\widehat{\mathbf{f} - \bar{\mathbf{f}}})}{\partial x} + \frac{i}{\omega}(\sigma_y + \sigma_z)\mathbf{A}\frac{\partial(\widehat{\mathbf{f} - \bar{\mathbf{f}}})}{\partial x} - \frac{1}{\omega^2}\sigma_y\sigma_z\mathbf{A}\frac{\partial(\widehat{\mathbf{f} - \bar{\mathbf{f}}})}{\partial x} \\
& + \mathbf{B}\frac{\partial(\widehat{\mathbf{f} - \bar{\mathbf{f}}})}{\partial y} + \frac{i}{\omega}(\sigma_x + \sigma_z)\mathbf{B}\frac{\partial(\widehat{\mathbf{f} - \bar{\mathbf{f}}})}{\partial y} - \frac{1}{\omega^2}\sigma_x\sigma_z\mathbf{B}\frac{\partial(\widehat{\mathbf{f} - \bar{\mathbf{f}}})}{\partial y} \\
& + \mathbf{C}\frac{\partial(\widehat{\mathbf{f} - \bar{\mathbf{f}}})}{\partial z} + \frac{i}{\omega}(\sigma_x + \sigma_y)\mathbf{C}\frac{\partial(\widehat{\mathbf{f} - \bar{\mathbf{f}}})}{\partial z} - \frac{1}{\omega^2}\sigma_x\sigma_y\mathbf{C}\frac{\partial(\widehat{\mathbf{f} - \bar{\mathbf{f}}})}{\partial z} = -\frac{1}{\lambda}(1 \\
& + \frac{i}{\omega}(\sigma_x + \sigma_y + \sigma_z) - \frac{1}{\omega^2}(\sigma_x\sigma_y + \sigma_x\sigma_z + \sigma_y\sigma_z) - \frac{i}{\omega^3}\sigma_x\sigma_y\sigma_z)\left(\widehat{\mathbf{f} - \mathbf{f}^{eq}}\right) \quad (81)
\end{aligned}$$

We can write the above back in the time domain by introducing auxiliary variables \mathbf{q}_1 , \mathbf{q}_2 , \mathbf{r}_1 , \mathbf{r}_2 , and \mathbf{r}_3 such that

$$\frac{\partial \mathbf{q}_1}{\partial t} = \mathbf{f} - \bar{\mathbf{f}}, \quad \frac{\partial \mathbf{q}_2}{\partial t} = \mathbf{q}_1, \quad \frac{\partial \mathbf{r}_1}{\partial t} = \mathbf{f} - \mathbf{f}^{eq}, \quad \frac{\partial \mathbf{r}_2}{\partial t} = \mathbf{r}_1, \quad \frac{\partial \mathbf{r}_3}{\partial t} = \mathbf{r}_2 \quad (82)$$

In the original physical space and time, the unsplit PML absorbing equations in three dimensions can finally be written as

$$\begin{aligned}
& \frac{\partial \mathbf{f}}{\partial t} + (\sigma_x + \sigma_y + \sigma_z)(\mathbf{f} - \bar{\mathbf{f}}) + (\sigma_x\sigma_y + \sigma_x\sigma_z + \sigma_y\sigma_z)\mathbf{q}_1 + \sigma_x\sigma_y\sigma_z\mathbf{q}_2 \\
& + \sigma_x\beta\mathbf{A}[(\mathbf{f} - \bar{\mathbf{f}}) + (\sigma_y + \sigma_z)\mathbf{q}_1 + \sigma_y\sigma_z\mathbf{q}_2] + \mathbf{A}\frac{\partial \mathbf{f}}{\partial x} + (\sigma_y + \sigma_z)\mathbf{A}\frac{\partial \mathbf{q}_1}{\partial x} + \sigma_y\sigma_z\mathbf{A}\frac{\partial \mathbf{q}_2}{\partial x}
\end{aligned}$$

$$\begin{aligned}
& + \mathbf{B} \frac{\partial \mathbf{f}}{\partial y} + (\sigma_x + \sigma_z) \mathbf{B} \frac{\partial \mathbf{q}_1}{\partial y} + \sigma_x \sigma_z \mathbf{B} \frac{\partial \mathbf{q}_2}{\partial y} + \mathbf{C} \frac{\partial \mathbf{f}}{\partial z} + (\sigma_x + \sigma_y) \mathbf{C} \frac{\partial \mathbf{q}_1}{\partial z} + \sigma_x \sigma_y \mathbf{C} \frac{\partial \mathbf{q}_2}{\partial z} \\
& = -\frac{1}{\lambda} (\mathbf{f} - \mathbf{f}^{eq}) - \frac{1}{\lambda} (\sigma_x + \sigma_y + \sigma_z) \mathbf{r}_1 - \frac{1}{\lambda} (\sigma_x \sigma_y + \sigma_x \sigma_z + \sigma_y \sigma_z) \mathbf{r}_2 - \frac{1}{\lambda} \sigma_x \sigma_y \sigma_z \mathbf{r}_3
\end{aligned} \tag{83}$$

3.3.2 Derivation of Split PML Equations

To derive the split PML equations in three dimensions, we start with Eq. (80) and we introduce auxiliary variables \mathbf{q}_1 , \mathbf{q}_2 , \mathbf{q}_3 , and \mathbf{q}_4 which satisfy the following equations

$$(-i\omega)\hat{\mathbf{q}}_1 + (-i\omega)\beta \mathbf{A}(\widehat{\mathbf{f} - \bar{\mathbf{f}}}) + \frac{1}{1 + \frac{i\sigma_x}{\omega}} \mathbf{A} \frac{\partial(\widehat{\mathbf{f} - \bar{\mathbf{f}}})}{\partial x} = 0 \tag{84}$$

$$(-i\omega)\hat{\mathbf{q}}_2 + \frac{1}{1 + \frac{i\sigma_y}{\omega}} \mathbf{B} \frac{\partial(\widehat{\mathbf{f} - \bar{\mathbf{f}}})}{\partial y} = 0 \tag{85}$$

$$(-i\omega)\hat{\mathbf{q}}_3 + \frac{1}{1 + \frac{i\sigma_z}{\omega}} \mathbf{C} \frac{\partial(\widehat{\mathbf{f} - \bar{\mathbf{f}}})}{\partial z} = 0 \tag{86}$$

$$(-i\omega)\hat{\mathbf{q}}_4 = -\frac{1}{\lambda} (\widehat{\mathbf{f} - \mathbf{f}^{eq}}) \tag{87}$$

Eq. (80) is recovered where $\hat{\mathbf{f}}' = \hat{\mathbf{q}}_1 + \hat{\mathbf{q}}_2 + \hat{\mathbf{q}}_3 + \hat{\mathbf{q}}_4$. Multiplying Eqs. (84), (85), and (86) by $(1 + \frac{i\sigma_x}{\omega})$, $(1 + \frac{i\sigma_y}{\omega})$ and $(1 + \frac{i\sigma_z}{\omega})$ respectively, we obtain

$$(-i\omega)\hat{\mathbf{q}}_1 + \sigma_x \hat{\mathbf{q}}_1 + \sigma_x \beta \mathbf{A}(\widehat{\mathbf{f} - \bar{\mathbf{f}}}) + (-i\omega)\beta \mathbf{A}(\widehat{\mathbf{f} - \bar{\mathbf{f}}}) + \mathbf{A} \frac{\partial(\widehat{\mathbf{f} - \bar{\mathbf{f}}})}{\partial x} = 0 \tag{88}$$

$$(-i\omega)\hat{\mathbf{q}}_2 + \sigma_y \hat{\mathbf{q}}_2 + \mathbf{B} \frac{\partial(\widehat{\mathbf{f} - \bar{\mathbf{f}}})}{\partial y} = 0 \tag{89}$$

$$(-i\omega)\hat{\mathbf{q}}_3 + \sigma_z \hat{\mathbf{q}}_3 + \mathbf{C} \frac{\partial(\widehat{\mathbf{f} - \bar{\mathbf{f}}})}{\partial z} = 0 \tag{90}$$

$$(-i\omega)\hat{\mathbf{q}}_4 = -\frac{1}{\lambda} (\widehat{\mathbf{f} - \mathbf{f}^{eq}}) \tag{91}$$

Changing the above back to the original time domain gives

$$\frac{\partial \mathbf{q}_1}{\partial t} + \sigma_x \mathbf{q}_1 + \sigma_x \beta \mathbf{A}(\mathbf{f} - \bar{\mathbf{f}}) + \mathbf{A} \frac{\partial(\mathbf{f} - \bar{\mathbf{f}})}{\partial x} = 0 \quad (92)$$

$$\frac{\partial \mathbf{q}_2}{\partial t} + \sigma_y \mathbf{q}_2 + \mathbf{B} \frac{\partial(\mathbf{f} - \bar{\mathbf{f}})}{\partial y} = 0 \quad (93)$$

$$\frac{\partial \mathbf{q}_3}{\partial t} + \sigma_z \mathbf{q}_3 + \mathbf{C} \frac{\partial(\mathbf{f} - \bar{\mathbf{f}})}{\partial z} = 0 \quad (94)$$

$$\frac{\partial \mathbf{q}_4}{\partial t} = -\frac{1}{\lambda} (\mathbf{f} - \mathbf{f}^{eq}) \quad (95)$$

If we add Eqs. (92), (93), (94), and (95) we obtain the equation for \mathbf{f} and the set of split PML equations

$$\frac{\partial \mathbf{f}}{\partial t} + \mathbf{A} \frac{\partial \mathbf{f}}{\partial x} + \mathbf{B} \frac{\partial \mathbf{f}}{\partial y} + \mathbf{C} \frac{\partial \mathbf{f}}{\partial z} + \sigma_x \mathbf{q}_1 + \sigma_y \mathbf{q}_2 + \sigma_z \mathbf{q}_3 + \sigma_x \beta \mathbf{A}(\mathbf{f} - \bar{\mathbf{f}}) = -\frac{1}{\lambda} (\mathbf{f} - \mathbf{f}^{eq}) \quad (96)$$

$$\frac{\partial \mathbf{q}_1}{\partial t} + \sigma_x \mathbf{q}_1 + \sigma_x \beta \mathbf{A}(\mathbf{f} - \bar{\mathbf{f}}) + \mathbf{A} \frac{\partial(\mathbf{f} - \bar{\mathbf{f}})}{\partial x} = 0 \quad (97)$$

$$\frac{\partial \mathbf{q}_2}{\partial t} + \sigma_y \mathbf{q}_2 + \mathbf{B} \frac{\partial(\mathbf{f} - \bar{\mathbf{f}})}{\partial y} = 0 \quad (98)$$

$$\frac{\partial \mathbf{q}_3}{\partial t} + \sigma_z \mathbf{q}_3 + \mathbf{C} \frac{\partial(\mathbf{f} - \bar{\mathbf{f}})}{\partial z} = 0 \quad (99)$$

Given $\boldsymbol{\xi}_i = (u_i, v_i, w_i)$, we can write the split PML equations in component form

$$\frac{\partial f_i}{\partial t} + u_i \frac{\partial f_i}{\partial x} + v_i \frac{\partial f_i}{\partial y} + w_i \frac{\partial f_i}{\partial z} + \sigma_x q_{1i} + \sigma_y q_{2i} + \sigma_z q_{3i} + \sigma_x \beta u_i (f_i - \bar{f}_i) = -\frac{1}{\lambda} (f_i - f_i^{eq}) \quad (100)$$

$$\frac{\partial q_{1i}}{\partial t} + \sigma_x q_{1i} + \sigma_x \beta u_i (f_i - \bar{f}_i) + u_i \frac{\partial(f_i - \bar{f}_i)}{\partial x} = 0 \quad (101)$$

$$\frac{\partial q_{2i}}{\partial t} + \sigma_y q_{2i} + v_i \frac{\partial(f_i - \bar{f}_i)}{\partial y} = 0 \quad (102)$$

$$\frac{\partial q_{3i}}{\partial t} + \sigma_z q_{3i} + w_i \frac{\partial(f_i - \bar{f}_i)}{\partial z} = 0 \quad (103)$$

The variations for the absorption coefficients σ_x , σ_y , and σ_z are shown in Figure 9.

CHAPTER 4

FINITE DIFFERENCES SOLUTION OF PML EQUATIONS

4.1 INTRODUCTION TO IMPLICIT EXPLICIT (IMEX) RUNGE-KUTTA SCHEMES

For the applications considered in this work, the relaxation parameter in the BGK operator is very small and the system is considered stiff. When we seek a finite difference solution to the DVBE coupled with the PML equations derived in the previous chapter, the stiffness of the collision operator becomes problematic for the time discretization. This is not an issue for the lattice solution of the DVBE because the time step is set by the lattice size, whereas in the case of finite differences, the time step is an independent numerical parameter.

Explicit time integration schemes restrict the time step to be in the order of the relaxation time λ for the computation to be stable [13]. Since the relaxation time is very small, explicit integration schemes are not a practical option for aeroacoustic problems.

With stability being the dominant consideration, implicit methods are more appropriate because they have larger stability regions. However, implicit integration schemes require the solution of linear systems with added approximations for the evaluation of Jacobian matrices due to the non-linearity of the collision term [53]. In addition, the stiffness of the system may also restrict the time step for iterations to converge. Recently developed implicit explicit (IMEX) Runge-Kutta methods provide a more efficient alternative to both fully explicit and implicit methods and they have the added benefit of a fully explicit implementation due to the properties of the BGK operator.

In designing time integration methods for evolution equations such as the Boltzmann-BGK or the Navier-Stokes equations, it is useful to consider separately the different driving forces that make up the governing equations, such as convection, diffusion or reaction [75]. This can be done by employing partitioned methods which combine several integration schemes into one so that the resulting combination is more efficient for the overall system than any of its component schemes alone. Terms, equations, or even gridpoints can be the basis for the partitioning of the governing equations and various techniques can be employed for the construction of the

composite scheme [76].

When the partitioning of the governing equations is done on a term by term basis the resulting methods are referred to as additive methods [77]. Due to their simple design and strong theoretical background, the Runge-Kutta schemes are well suited for the construction of additive schemes. Runge-Kutta schemes are particularly useful because they permit direct control of partitioning errors and thus allow for the construction of stable high-order partitioned methods [75].

The IMEX Runge-Kutta schemes are a class of additive Runge-Kutta methods that combine implicit and explicit Runge-Kutta schemes and are specifically designed to integrate systems that contain stiff terms [10, 53, 54]. More specifically, the stiff terms are integrated using an implicit method and the remaining non-stiff terms are integrated by an explicit method. To ensure an explicit evaluation of the non-stiff terms in the composite IMEX scheme, only diagonally implicit L-stable Runge-Kutta schemes are considered for the implicit integration of the stiff term. Strong Stability Preserving (SSP) schemes are preferred for the explicit integration to prevent oscillations in the limit toward the conservation equations. General conditions are imposed so that the scheme is both consistent with the equilibrium system and accurate in the stiff limit [54].

To apply the IMEX Runge-Kutta scheme to the DVBE we first rewrite the equation as the sum of its non-stiff and stiff terms as follows:

$$\frac{\partial \mathbf{f}}{\partial t} = h(\mathbf{f}) + \frac{1}{\lambda}g(\mathbf{f})$$

where $h(\mathbf{f})$ denotes symbolically all the non-collision terms and $g(\mathbf{f})$ denotes the part in the collision term. The IMEX numerical scheme for solution \mathbf{f}^n at time t_n to advance to \mathbf{f}^{n+1} at time $t_n + \Delta t$ is

$$\mathbf{f}^{n+1} = \mathbf{f}^n + \Delta t \sum_{i=1}^{\nu} \tilde{w}_i h(\mathbf{f}^{(i)}) + \frac{\Delta t}{\lambda} \sum_{i=1}^{\nu} w_i g(\mathbf{f}^{(i)}) \quad (104)$$

where the stage values $\mathbf{f}^{(i)}$ are given by

$$\mathbf{f}^{(1)} = \mathbf{f}^n + \frac{\Delta t}{\lambda} a_{11} g(\mathbf{f}^{(1)}), \quad (105)$$

$$\mathbf{f}^{(i)} = \mathbf{f}^n + \Delta t \sum_{j=1}^{i-1} \tilde{a}_{ij} h(\mathbf{f}^{(j)}) + \frac{\Delta t}{\lambda} \sum_{j=1}^i a_{ij} g(\mathbf{f}^{(j)}), \quad i = 2, 3, \dots, \nu. \quad (106)$$

The coefficients \tilde{a}_{ij} , \tilde{w}_i , a_{ij} , and w_i are selected to maximize accuracy and are listed in a double Butcher's *tableau* as follows:

$$\begin{array}{c|c} \tilde{c} & \tilde{A} \\ \hline & \tilde{w}^T \end{array} \qquad \begin{array}{c|c} c & A \\ \hline & w \end{array}$$

In the finite difference numerical examples, we will compare the solutions obtained with three IMEX schemes of different orders of accuracy. For the second order scheme, we will use the stiffly accurate IMEX-SSP2(3,2,2) advanced by Pareschi and Russo [54]. The explicit component of this IMEX scheme maintains strong stability at the discrete level and is referred to as Strong Stability Preserving (SSP), while the implicit component is an L-stable scheme. IMEX-SSP2(3,2,2) requires the computation of three stages before the solution can be advanced to the next time step, as evident from the coefficient *tableau* below:

$$\begin{array}{c|ccc} 0 & 0 & 0 & 0 \\ 0 & 0 & 0 & 0 \\ 1 & 0 & 1 & 0 \\ \hline & 0 & \frac{1}{2} & \frac{1}{2} \end{array} \qquad \begin{array}{c|ccc} \frac{1}{2} & \frac{1}{2} & 0 & 0 \\ 0 & -\frac{1}{2} & \frac{1}{2} & 0 \\ 1 & 0 & \frac{1}{2} & \frac{1}{2} \\ \hline & 0 & \frac{1}{2} & \frac{1}{2} \end{array}$$

For the third order IMEX scheme, we will use IMEX-SSP3(4,3,3), also proposed by Pareschi and Russo, and composed of an SSP explicit scheme and an L-stable implicit scheme. The third order scheme requires four stages before advancing the solution to the next time step. If we let $\alpha_1 = 0.24169426078821$, $\alpha_2 = 0.06042356519705$, and $\alpha_3 = 0.1291528696059$, we can write the coefficients for the third order scheme as:

$$\begin{array}{c|cccc} 0 & 0 & 0 & 0 & 0 \\ 0 & 0 & 0 & 0 & 0 \\ 1 & 0 & 1 & 0 & 0 \\ \frac{1}{2} & 0 & \frac{1}{4} & \frac{1}{4} & 0 \\ \hline & 0 & \frac{1}{6} & \frac{1}{6} & \frac{2}{3} \end{array} \qquad \begin{array}{c|ccccc} \alpha_1 & \alpha_1 & 0 & 0 & 0 \\ 0 & -\alpha_1 & \alpha_1 & 0 & 0 \\ 1 & 0 & 1 - \alpha_1 & \alpha_1 & 0 \\ \frac{1}{2} & \alpha_2 & \alpha_3 & \frac{1}{2} - \alpha_2 - \alpha_3 - \alpha_1 & \alpha_1 \\ \hline & 0 & \frac{1}{6} & \frac{1}{6} & \frac{2}{3} \end{array}$$

We also use the fourth order IMEX scheme ARK4(3)6L[2]SA proposed by Kennedy and Carpenter [75]. In this scheme, the stiff terms are integrated by an L-stable, stiffly accurate explicit, singly diagonal implicit Runge-Kutta method (ESDIRK) while the nonstiff terms are integrated using a traditional explicit Runge-Kutta method (ERK). The coefficients for the explicit scheme ARK4(3)6L[2]SA-ERK are given as

0	0	0	0	0	0	0	0
$\frac{1}{2}$	$\frac{1}{2}$	0	0	0	0	0	0
$\frac{83}{250}$	$\frac{13861}{62500}$	$\frac{6889}{62500}$	0	0	0	0	0
$\frac{31}{50}$	$\frac{-116923316275}{2393684061468}$	$\frac{-2731218467317}{15368042101831}$	$\frac{9408046702089}{11113171139209}$	0	0	0	0
$\frac{17}{20}$	$\frac{-451086348788}{2902428689909}$	$\frac{-2682348792572}{7519795681897}$	$\frac{12662868775082}{11960479115383}$	$\frac{3355817975965}{11060851509271}$	0	0	0
1	$\frac{647845179188}{3216320057751}$	$\frac{73281519250}{8382639484533}$	$\frac{552539513391}{3454668386233}$	$\frac{3354512671639}{8306763924573}$	$\frac{4040}{17871}$	0	0
	$\frac{82889}{524892}$	0	$\frac{15625}{83664}$	$\frac{69875}{102672}$	$\frac{-2260}{8211}$	$\frac{1}{4}$	

and the coefficients for the implicit scheme ARK4(3)6L[2]SA-ESDIRK are

0	0	0	0	0	0	0	0
$\frac{1}{2}$	$\frac{1}{4}$	$\frac{1}{4}$	0	0	0	0	0
$\frac{83}{250}$	$\frac{8611}{62500}$	$\frac{-1743}{31250}$	$\frac{1}{4}$	0	0	0	0
$\frac{31}{50}$	$\frac{5012029}{34652500}$	$\frac{-654441}{2922500}$	$\frac{174375}{388108}$	$\frac{1}{4}$	0	0	0
$\frac{17}{20}$	$\frac{15267082809}{155376265600}$	$\frac{-71443401}{120774400}$	$\frac{730878875}{902184768}$	$\frac{2285395}{8070912}$	$\frac{1}{4}$	0	0
1	$\frac{82889}{524892}$	0	$\frac{15625}{83664}$	$\frac{69875}{102672}$	$\frac{-2260}{8211}$	$\frac{1}{4}$	
	$\frac{82889}{524892}$	0	$\frac{15625}{83664}$	$\frac{69875}{102672}$	$\frac{-2260}{8211}$	$\frac{1}{4}$	

4.2 IMEX IMPLEMENTATION

For the benefits mentioned in the previous section, we will use IMEX Runge-Kutta schemes for the finite difference solution of the discrete velocity Boltzmann-BGK Eq. (17) and the PML absorbing Eqs. (57)-(59). Although the IMEX Runge-Kutta schemes have implicit steps, the special structure of the BGK collision operator permits a fully explicit numerical implementation.

Since the local equilibrium state in the BGK collision model minimizes the entropy of all the states that produce the same macroscopic properties, at any point in space and time, the distribution function f and the Maxwellian distribution function f^{eq} produce the same macroscopic density, momentum and internal energy.

$$\rho(\mathbf{x}, t) = \int f(\mathbf{x}, \boldsymbol{\xi}, t) d\boldsymbol{\xi} = \int f^{eq}(\mathbf{x}, \boldsymbol{\xi}, t) d\boldsymbol{\xi} \quad (107)$$

$$\rho(\mathbf{x}, t)\mathbf{u}(\mathbf{x}, t) = \int f(\mathbf{x}, \boldsymbol{\xi}, t)\boldsymbol{\xi} d\boldsymbol{\xi} = \int f^{eq}(\mathbf{x}, \boldsymbol{\xi}, t)\boldsymbol{\xi} d\boldsymbol{\xi} \quad (108)$$

$$\rho(\mathbf{x}, t)e(\mathbf{x}, t) = \int f(\mathbf{x}, \boldsymbol{\xi}, t) \frac{(\boldsymbol{\xi} - \mathbf{u})^2}{2} d\boldsymbol{\xi} = \int f^{eq}(\mathbf{x}, \boldsymbol{\xi}, t) \frac{(\boldsymbol{\xi} - \mathbf{u})^2}{2} d\boldsymbol{\xi} \quad (109)$$

This property follows from an assumption in the Chapman-Enskog approximation which states that integrating the product of a linear combination of collisional invariants with either the distribution function f or the Maxwellian distribution function f^{eq} over the velocity space produces the same results [56]. The equilibrium distribution function f^{eq} used in the discrete velocity models we consider in this paper also satisfies this property with respect to the discrete velocities and quadrature weights prescribed by the model [3].

$$\rho = \sum_{j=1}^N f_j = \sum_{j=1}^N f_j^{eq} \quad (110)$$

$$\rho \mathbf{u} = \sum_{j=1}^N f_j \boldsymbol{\xi}_j = \sum_{j=1}^N f_j^{eq} \boldsymbol{\xi}_j \quad (111)$$

$$\rho e = \frac{1}{2} \sum_{j=1}^N f_j (\boldsymbol{\xi}_j - \mathbf{u})^2 = \frac{1}{2} \sum_{j=1}^N f_j^{eq} (\boldsymbol{\xi}_j - \mathbf{u})^2 \quad (112)$$

where

$$f_j \equiv f_j(\mathbf{x}, t) \equiv W_j f(\mathbf{x}, \boldsymbol{\xi}_j, t) \quad (113)$$

$$f_j^{eq} \equiv f_j^{eq}(\mathbf{x}, t) \equiv W_j f^{eq}(\mathbf{x}, \boldsymbol{\xi}_j, t) \quad (114)$$

and W_j represent the weight coefficients in the quadrature. For the purpose of validating the PML equations, discrete velocity models with a small velocity set are sufficient. However, higher order discrete velocity models can be obtained by expanding the equilibrium distribution function in Hermite polynomials to higher orders and by using higher precision Gauss-Hermite quadratures [68].

These properties of the collision operator allow us to solve the implicit step for the stage distribution function $\mathbf{f}^{(i)}$ in the IMEX scheme explicitly. To demonstrate how this is accomplished, let us consider the D2Q9 discrete velocity model as an example. We will begin by taking the moments of the IMEX stage Eqs. (105) and (106) to obtain the macroscopic density $\rho^{(i)}$ and macroscopic velocity $\mathbf{u}^{(i)}$ as in [53]. The first stage density value is given by

$$\rho^{(1)} = \sum_{k=1}^9 f_k^{(1)} = \sum_{k=1}^9 f_k^n + \frac{\Delta t}{\lambda} \sum_{k=1}^9 a_{11} g(f_k^{(1)}) \quad (115)$$

Remembering that $g(f_k^{(1)})$ represents the collision term and is given by

$$g(f_k^{(1)}) = f_k^{eq(1)} - f_k^{(1)} \quad (116)$$

and making use of Eq. (110), we can see that

$$\sum_{k=1}^9 a_{11} g(f_k^{(1)}) = a_{11} \sum_{k=1}^9 (f_k^{eq(1)} - f_k^{(1)}) = a_{11} \sum_{k=1}^9 f_k^{eq(1)} - a_{11} \sum_{k=1}^9 f_k^{(1)} = 0 \quad (117)$$

so the first stage macroscopic density is obtained from the previous function values as

$$\rho^{(1)} = \sum_{k=1}^9 f_k^n \quad (118)$$

Since $\rho^{(1)}$ is now known, if we make use of Eq. (111) to show that

$$\sum_{k=1}^9 a_{11} g(f_k^{(1)}) \boldsymbol{\xi}_k = a_{11} \sum_{k=1}^9 (f_k^{eq(1)} - f_k^{(1)}) \boldsymbol{\xi}_k = a_{11} \sum_{k=1}^9 f_k^{eq(1)} \boldsymbol{\xi}_k - a_{11} \sum_{k=1}^9 f_k^{(1)} \boldsymbol{\xi}_k = 0 \quad (119)$$

we can also obtain the macroscopic velocity $\mathbf{u}^{(1)}$ from

$$\rho^{(1)} \mathbf{u}^{(1)} = \sum_{k=1}^9 f_k^{(1)} \boldsymbol{\xi}_k = \sum_{k=1}^9 f_k^n \boldsymbol{\xi}_k \quad (120)$$

Having obtained both $\rho^{(1)}$ and $\mathbf{u}^{(1)}$, we can now replace them in Eq. (11) to get the equilibrium distribution functions $f_k^{eq(1)}$. Finally, the first stage distribution functions $f_k^{(1)}$ can be obtained explicitly from Eq. (105) as

$$f_k^{(1)} = \frac{1}{1 + \frac{\Delta t}{\lambda} a_{11}} \left[f_k^n + \frac{\Delta t}{\lambda} a_{11} f_k^{eq(1)} \right] \quad (121)$$

The distribution functions for the remaining stages in the IMEX scheme can be computed subsequently by following the same procedure as for the first stage. More specifically, the macroscopic density $\rho^{(i)}$ and velocity $\mathbf{u}^{(i)}$ can be recovered from

$$\rho^{(i)} = \sum_{k=1}^9 f_k^{(i)} = \sum_{k=1}^9 f_k^n + \Delta t \sum_{k=1}^9 \sum_{j=1}^{i-1} \tilde{a}_{ij} h(f_k^{(j)}) + \frac{\Delta t}{\lambda} \sum_{k=1}^9 \sum_{j=1}^i a_{ij} g(f_k^{(j)}) \quad (122)$$

and

$$\rho^{(i)} \mathbf{u}^{(i)} = \sum_{k=1}^9 f_k^{(i)} \boldsymbol{\xi}_k = \sum_{k=1}^N f_k^n \boldsymbol{\xi}_k + \Delta t \sum_{k=1}^N \sum_{j=1}^{i-1} \tilde{a}_{ij} h(f_k^{(j)}) \boldsymbol{\xi}_k + \frac{\Delta t}{\lambda} \sum_{k=1}^N \sum_{j=1}^i a_{ij} g(f_k^{(j)}) \boldsymbol{\xi}_k \quad (123)$$

which, due to the identities in Eqs. (110) and (111), reduce to

$$\rho^{(i)} = \sum_{k=1}^9 f_k^n + \Delta t \sum_{k=1}^9 \sum_{j=1}^{i-1} \tilde{a}_{ij} h(f_k^{(j)}) \quad (124)$$

and

$$\rho^{(i)} \mathbf{u}^{(i)} = \sum_{k=1}^9 f_k^n \boldsymbol{\xi}_k + \Delta t \sum_{k=1}^9 \sum_{j=1}^{i-1} \tilde{a}_{ij} h(f_k^{(j)}) \boldsymbol{\xi}_k \quad (125)$$

By substituting the macroscopic variables $\rho^{(i)}$ and $\mathbf{u}^{(i)}$ obtained above into Eq. (11) we can find the equilibrium distribution functions $f_k^{eq(i)}$, so that the distribution functions $f_k^{(i)}$ can be explicitly obtained from Eq. (106) as

$$f_k^{(i)} = \frac{1}{1 + \frac{\Delta t}{\lambda} a_{ii}} \left[f_k^n + \Delta t \sum_{j=1}^{i-1} \left(\tilde{a}_{ij} h(f_k^{(j)}) + \frac{a_{ij}}{\lambda} g(f_k^{(j)}) \right) + \frac{\Delta t}{\lambda} a_{ii} f_k^{eq(1)} \right] \quad (126)$$

Once the procedure described above is completed for all the stages of the IMEX scheme under consideration, the stage distribution functions can be replaced into Eq. (104) to advance the solution to the next time step.

4.3 IMEX STABILITY

The qualitative behavior of dynamical systems can be determined by examining the local solution in the neighborhood of equilibrium points. As such, we can obtain information about the stability of a system by studying the stability of its equilibrium points, more specifically the origin since equilibrium points can always be translated there. One frequently used way of doing this, outlined by the Poincare-Lyapunov theorem, is to determine the stability of equilibrium points by examining the eigenvalues of the linear part of the dynamical system. This analysis stipulates that the origin is an asymptotically stable equilibrium point if all the eigenvalues of the linear system have negative real parts.

Correspondingly, we can determine the stability of numerical methods for ordinary differential equations, such as the IMEX Runge-Kutta schemes used in this paper, by considering the eigenvalues of the linearized system. Specifically, this is done by applying one step of the numerical scheme to the test problem:

$$\frac{\partial y}{\partial t} = \lambda y; \quad y(0) = 1 \quad (127)$$

where λ is an eigenvalue of the linear system. The application of Runge-Kutta numerical schemes to the above test problem leads to the following general form:

$$y_{n+1} = R(\Delta t \lambda) y_n \quad (128)$$

The function $R(\Delta t \lambda)$ is called the *stability function* of the Runge-Kutta method and it is a polynomial of $\Delta t \lambda$ in the case of explicit schemes and a rational function of $\Delta t \lambda$ in the case of implicit schemes. The numerical scheme is stable if and only if

$$\hat{R}(\Delta t \lambda) = |R(\Delta t \lambda)| \leq 1 \quad (129)$$

for all eigenvalues λ . The region where this condition is satisfied is called the *stability region* of the numerical method and it is considered to be one of the most important factors in determining the performance of numerical methods for the solution of ordinary differential equations. Given a set of eigenvalues, the stability region specifies the restriction on the maximum time step Δt that can be used so the numerical method is stable.

To obtain the stability region for the IMEX Runge-Kutta schemes as applied to the Boltzmann-BGK equation, we assume that the stiff collision operator has predominantly real eigenvalues, λ_g , while the convective terms have eigenvalues, λ_f , that are predominantly purely imaginary. We obtain the following model problem:

$$\frac{\partial y}{\partial t} = \lambda_f y + \lambda_g y \quad (130)$$

When we apply the numerical scheme to the above model equation, we use the implicit part of the scheme for the term $\lambda_g y$ and the explicit part for the term $\lambda_f y$. The stability function for the three IMEX Runge-Kutta schemes used in this paper can be written in terms of the scaled eigenvalues $\mu_f = \Delta t \lambda_f$ and $\mu_g = \Delta t \lambda_g$ as follows:

$$\begin{aligned}
R_2(\mu_f, \mu_g) = & 1 + (\mu_f + \mu_g) \left\{ w_2 \frac{(1 - a_{11}\mu_g + a_{21}\mu_g)}{(1 - a_{11}\mu_g)(1 - a_{22}\mu_g)} \right. \\
& \left. + \frac{w_3}{1 - a_{33}\mu_g} \left[1 + \frac{(\tilde{a}_{32}\mu_f + a_{32}\mu_g)(1 - a_{11}\mu_g + a_{21}\mu_g)}{(1 - a_{11}\mu_g)(1 - a_{22}\mu_g)} \right] \right\} \quad (131)
\end{aligned}$$

$$\begin{aligned}
R_3(\mu_f, \mu_g) = & 1 + (\mu_f + \mu_g) \left\{ w_2 \frac{(1 - a_{11}\mu_g + a_{21}\mu_g)}{(1 - a_{11}\mu_g)(1 - a_{22}\mu_g)} \right. \\
& + \frac{w_3}{1 - a_{33}\mu_g} \left[1 + \frac{(\tilde{a}_{32}\mu_f + a_{32}\mu_g)(1 - a_{11}\mu_g + a_{21}\mu_g)}{(1 - a_{11}\mu_g)(1 - a_{22}\mu_g)} \right] \\
& + \frac{w_4}{1 - a_{44}\mu_g} \left[1 + \frac{a_{41}\mu_g}{1 - a_{11}\mu_g} + \frac{(\tilde{a}_{42}\mu_f + a_{42}\mu_g)(1 - a_{11}\mu_g + a_{21}\mu_g)}{(1 - a_{11}\mu_g)(1 - a_{22}\mu_g)} \right. \\
& \left. \left. + \frac{\tilde{a}_{43}\mu_f + a_{43}\mu_g}{1 - a_{33}\mu_g} \left(1 + \frac{(\tilde{a}_{32}\mu_f + a_{32}\mu_g)(1 - a_{11}\mu_g + a_{21}\mu_g)}{(1 - a_{11}\mu_g)(1 - a_{22}\mu_g)} \right) \right] \right\} \quad (132)
\end{aligned}$$

$$\begin{aligned}
R_4(\mu_f, \mu_g) = & 1 + (\mu_f + \mu_g) \left\{ w_1 + \frac{w_3}{1 - a_{33}\mu_g} \right. \\
& \left[1 + \tilde{a}_{31}\mu_f + a_{31}\mu_g + \frac{(\tilde{a}_{32}\mu_f + a_{32}\mu_g)(1 + \tilde{a}_{21}\mu_f + a_{21}\mu_g)}{1 - a_{22}\mu_g} \right] + \frac{w_4}{1 - a_{44}\mu_g} \\
& \left[1 + \tilde{a}_{41}\mu_f + a_{41}\mu_g + \frac{(\tilde{a}_{42}\mu_f + a_{42}\mu_g)(1 + \tilde{a}_{21}\mu_f + a_{21}\mu_g)}{1 - a_{22}\mu_g} + \frac{(\tilde{a}_{43}\mu_f + a_{43}\mu_g)}{1 - a_{33}\mu_g} \right. \\
& \left. \left(1 + \tilde{a}_{31}\mu_f + a_{31}\mu_g + \frac{(\tilde{a}_{32}\mu_f + a_{32}\mu_g)(1 + \tilde{a}_{21}\mu_f + a_{21}\mu_g)}{1 - a_{22}\mu_g} \right) \right] \\
& \left. + \frac{w_5}{1 - a_{55}\mu_g} \left[1 + \tilde{a}_{51}\mu_f + a_{51}\mu_g + \frac{(\tilde{a}_{52}\mu_f + a_{52}\mu_g)(1 + \tilde{a}_{21}\mu_f + a_{21}\mu_g)}{1 - a_{22}\mu_g} \right] \right\}
\end{aligned}$$

$$\begin{aligned}
& + \frac{\tilde{a}_{53}\mu_f + a_{53}\mu_g}{1 - a_{33}\mu_g} \left(1 + \tilde{a}_{31}\mu_f + a_{31}\mu_g + \frac{(\tilde{a}_{32}\mu_f + a_{32}\mu_g)(1 + \tilde{a}_{21}\mu_f + a_{21}\mu_g)}{1 - a_{22}\mu_g} \right) \\
& + \frac{\tilde{a}_{54}\mu_f + a_{54}\mu_g}{1 - a_{44}\mu_g} \left(1 + \tilde{a}_{41}\mu_f + a_{41}\mu_g + \frac{(\tilde{a}_{42}\mu_f + a_{42}\mu_g)(1 + \tilde{a}_{21}\mu_f + a_{21}\mu_g)}{1 - a_{22}\mu_g} \right) \\
& + \frac{\tilde{a}_{43}\mu_f + a_{43}\mu_g}{1 - a_{33}\mu_g} \left(1 + \tilde{a}_{31}\mu_f + a_{31}\mu_g + \frac{(\tilde{a}_{32}\mu_f + a_{32}\mu_g)(1 + \tilde{a}_{21}\mu_f + a_{21}\mu_g)}{1 - a_{22}\mu_g} \right) \Bigg) \\
& + \frac{w_6}{1 - a_{66}\mu_g} \left[1 + \tilde{a}_{61}\mu_f + a_{61}\mu_g + \frac{(\tilde{a}_{62}\mu_f + a_{62}\mu_g)(1 + \tilde{a}_{21}\mu_f + a_{21}\mu_g)}{1 - a_{22}\mu_g} \right. \\
& + \frac{\tilde{a}_{63}\mu_f + a_{63}\mu_g}{1 - a_{33}\mu_g} \left(1 + \tilde{a}_{31}\mu_f + a_{31}\mu_g + \frac{(\tilde{a}_{32}\mu_f + a_{32}\mu_g)(1 + \tilde{a}_{21}\mu_f + a_{21}\mu_g)}{1 - a_{22}\mu_g} \right) \\
& + \frac{\tilde{a}_{64}\mu_f + a_{64}\mu_g}{1 - a_{44}\mu_g} \left(1 + \tilde{a}_{41}\mu_f + a_{41}\mu_g + \frac{(\tilde{a}_{42}\mu_f + a_{42}\mu_g)(1 + \tilde{a}_{21}\mu_f + a_{21}\mu_g)}{1 - a_{22}\mu_g} \right) \\
& + \frac{\tilde{a}_{43}\mu_f + a_{43}\mu_g}{1 - a_{33}\mu_g} \left(1 + \tilde{a}_{31}\mu_f + a_{31}\mu_g + \frac{(\tilde{a}_{32}\mu_f + a_{32}\mu_g)(1 + \tilde{a}_{21}\mu_f + a_{21}\mu_g)}{1 - a_{22}\mu_g} \right) \Bigg) \\
& + \frac{\tilde{a}_{65}\mu_f + a_{65}\mu_g}{1 - a_{55}\mu_g} \left(1 + \tilde{a}_{51}\mu_f + a_{51}\mu_g + \frac{(\tilde{a}_{52}\mu_f + a_{52}\mu_g)(1 + \tilde{a}_{21}\mu_f + a_{21}\mu_g)}{1 - a_{22}\mu_g} \right) \\
& + \frac{\tilde{a}_{53}\mu_f + a_{53}\mu_g}{1 - a_{33}\mu_g} \left(1 + \tilde{a}_{31}\mu_f + a_{31}\mu_g + \frac{(\tilde{a}_{32}\mu_f + a_{32}\mu_g)(1 + \tilde{a}_{21}\mu_f + a_{21}\mu_g)}{1 - a_{22}\mu_g} \right) \\
& + \frac{\tilde{a}_{54}\mu_f + a_{54}\mu_g}{1 - a_{44}\mu_g} \left(1 + \tilde{a}_{41}\mu_f + a_{41}\mu_g + \frac{(\tilde{a}_{42}\mu_f + a_{42}\mu_g)(1 + \tilde{a}_{21}\mu_f + a_{21}\mu_g)}{1 - a_{22}\mu_g} \right) \\
& + \frac{\tilde{a}_{43}\mu_f + a_{43}\mu_g}{1 - a_{33}\mu_g} \left(1 + \tilde{a}_{31}\mu_f + a_{31}\mu_g + \frac{(\tilde{a}_{32}\mu_f + a_{32}\mu_g)(1 + \tilde{a}_{21}\mu_f + a_{21}\mu_g)}{1 - a_{22}\mu_g} \right) \Bigg) \Bigg] \Bigg] \\
& \tag{133}
\end{aligned}$$

In deriving the expressions for the stability function, we only considered the nonzero coefficients of the schemes. Clearly, as the order of the scheme increases and

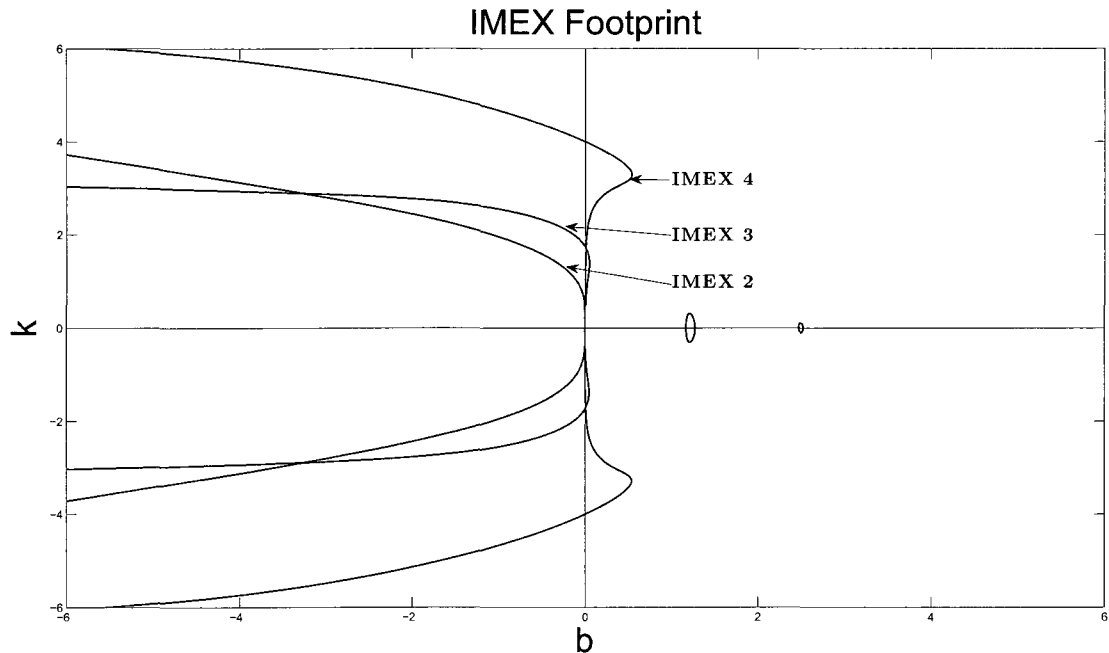


Fig. 10: Stability regions for the second, third, and fourth order IMEX schemes.

more stages have to be computed, the analytic expression for the stability function becomes more and more cumbersome. Rather than simplifying the analytical expressions of the stability functions, an easier way to obtain the stability regions is to plot the level curves of the function \hat{R} viewed as a function of b and k , the moduli of λ_g and λ_f . For example, this can be done in MATLAB using the *contourplot* command. In fact, only the level curve $\hat{R} = 1$ is needed because this level curve outlines exactly the boundary of the stability region. In Figure 10 we plot the stability regions for the three IMEX schemes and, as expected, with each increase in the order of the scheme, we obtain a larger stability region at the cost of having more intermediary stages to compute.

4.4 NUMERICAL EXAMPLES

4.4.1 Two-Dimensional PML - Acoustic Wave

We will first test the effectiveness of the two-dimensional unsplit PML Eq. (47) and split PML Eqs. (57)-(59) by simulating an acoustic wave traveling at the speed of sound relative to the mean flow $(U_0, 0)$. For this, we consider the physical domain

$[-5, 5] \times [-5, 5]$ with PML layers of width D surrounding the boundaries. The domain is discretized with a uniform grid $\Delta x = \Delta y = 0.1$. The initial conditions for density ρ and velocity components u and v are:

$$\rho = \rho_0 + \epsilon e^{-\ln 2 \frac{x^2+y^2}{\sigma^4}} \quad (134)$$

$$u = Mc_s; \quad v = 0 \quad (135)$$

where $\rho_0 = 1$ is the mean flow density and $M = 0.25$ is the Mach number defined by

$$M = \frac{U_0}{c_s} \quad (136)$$

Compared to the mean flow, acoustic waves generally have considerably smaller amplitudes and the error generated by the numerical scheme from the computation of the mean flow can sometimes be orders of magnitude larger than the sound intensity [78]. Therefore, the choice of numerical schemes for the propagation of acoustic waves cannot be based on the order of accuracy predicted by the Taylor series truncation alone, but also on a consideration of whether the number of wave modes and their characteristics supported by the computation scheme are the same as those of the original partial differential equations [78]. Since dispersion-relation-preserving (DRP) finite difference schemes are both numerically accurate and preserve the wave modes of the original system, they are able to predict the radiation of the acoustic waves accurately despite the large gap between the error generated by the mean flow computation and the amplitude of the sound waves. For this reason, the spatial discretization in this example will be done using the seven-point fourth-order DRP finite difference scheme of Tam and Webb [22]. Because the wave amplitude will have decreased to zero by the time it reached the end of the PML layers, we can use periodic boundary conditions for the x and y derivatives. The absorption coefficients σ_x and σ_y are used in the PML layers as illustrated in Figure 5 and are of the form

$$\sigma_x = \sigma_m \left| \frac{x - x_0}{D} \right|^\alpha, \quad \sigma_y = \sigma_m \left| \frac{y - y_0}{D} \right|^\alpha \quad (137)$$

where x_0 and y_0 are the locations of the DVBE-PML interfaces, the parameter $\alpha = 2$, D represents the width of the PML layer, and σ_m , generally satisfying $1 \leq \sigma_m \Delta x \leq 2$, is chosen so that $\sigma_m \Delta x = 1$ for all the examples presented here. The distribution functions f_i are initialized using the equilibrium values obtained from the initial

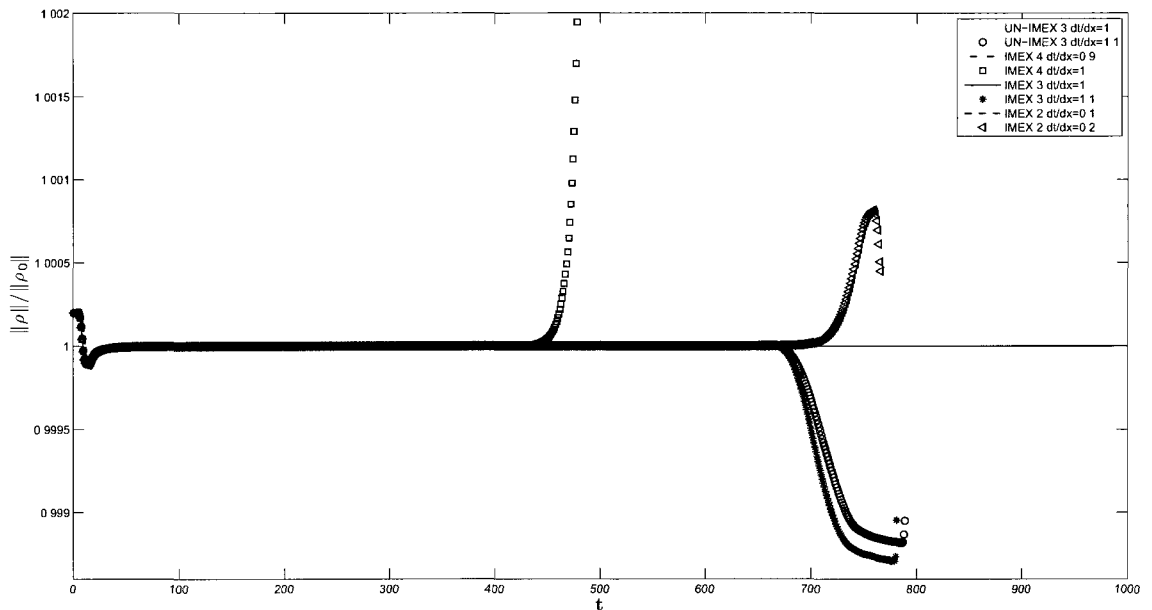


Fig. 11: Scaled norm of acoustic density ρ versus time for $\epsilon = 0.1$ showing the stability value for the ratio $\Delta t/\Delta x$ for the IMEX schemes.

macroscopic variables ρ and \mathbf{u} given in Eqs. (134)-(143) while the PML variables are initialized at zero.

The choice of value for the relaxation time λ is based on the ability of a discrete velocity Boltzmann-BGK model to capture the behavior of sound waves accurately. Marié and Ricot have shown that the error of the D3Q19 discrete velocity model for acoustic dissipation and dispersion is small if the relaxation time is small [14]. They conclude that in the limit of small λ , the discretization of velocity space produces no error in the behavior of sound waves. In order to minimize the error that the discrete velocity model could introduce in the simulation of sound waves, we choose the small relaxation time $\lambda = 0.00011$ for all the numerical examples in this paper.

Unless we are specifically comparing the effect of PML width on the reflection error, we will be using a PML width of $D = 10 \Delta x$, which in this case represents ten percent of the physical domain. However, it should be noted that the PML width is not contingent on the size of the interior domain. In fact, for a larger interior domain, the PML width would represent a smaller percentage of it.

Our first effort will be to compare the stability of the three IMEX schemes for

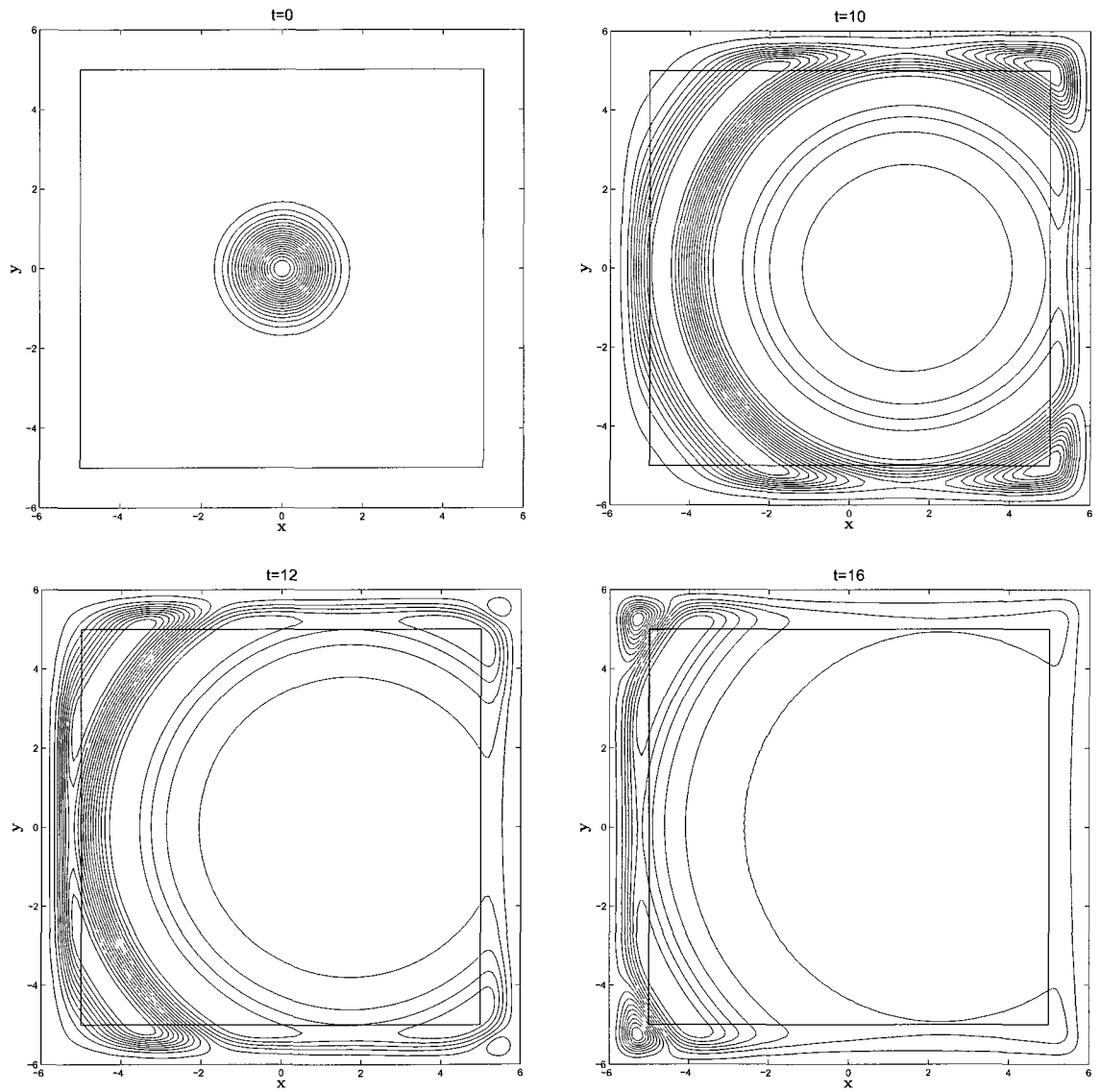


Fig. 12: Contours of IMEX 3 density at times $t = 0, 10, 12,$ and 16 for $\epsilon = 0.01$ showing the acoustic pulse exiting the boundaries with little reflection.

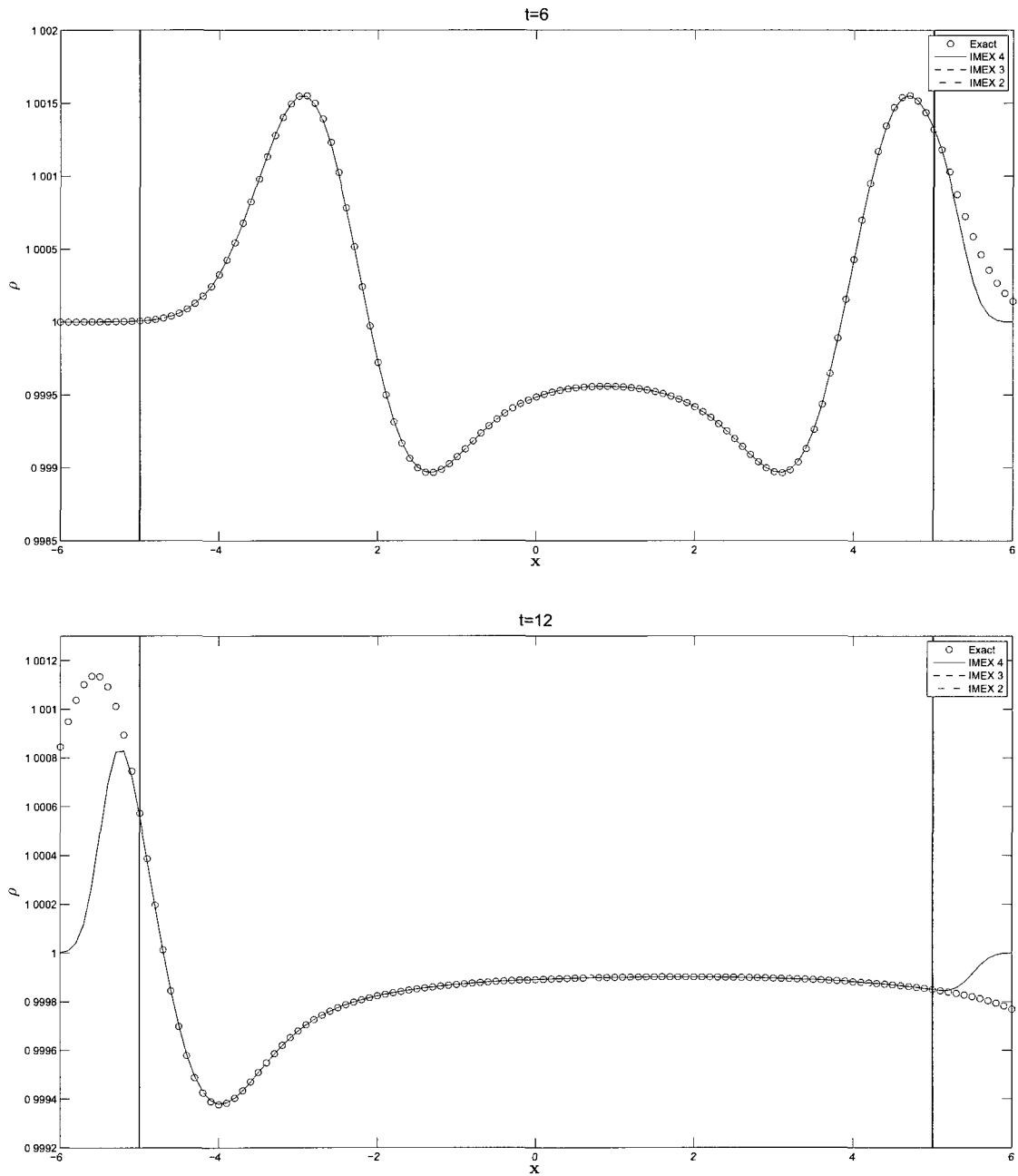


Fig. 13: Comparison of IMEX 3 numerical acoustic density solution with exact solution at times $t = 6$ and 12 for $\epsilon = 0.01$.

different values of time step Δt . For this, we plot the time evolution of the density norm given by

$$\|\rho\| = \left[\sum_i \sum_j (\rho(i, j))^2 \right]^{1/2} \quad (138)$$

and normalized by the mean flow density norm $\|\rho_0\|$. The results given in Figure 11 show that stable solutions are obtained for $\Delta t = 0.1 \Delta x$ for the second order IMEX scheme, $\Delta t = 1 \Delta x$ for the third order IMEX scheme, and $\Delta t = 0.9 \Delta x$ for the fourth order IMEX scheme. Although the stability region of the fourth order scheme is the largest of the three, it has a lower stability limit for the time step than the third order scheme. One possible justification for this inconsistency may be the fact that the third order scheme was designed to maintain strong stability at the discrete level, i.e. it is strong stability preserving (SSP) whereas the fourth order scheme is not. Also included in the graph is the solution obtained with the third order IMEX scheme for the unsplit PML formulation, and we can see that the same stability limit is obtained as for the split PML formulation.

In Figure 12 we show the contour plots of density at times $t = 0, 10, 12$ and 16 computed using the third order IMEX scheme. There is no apparent difference in the contours if the other two IMEX schemes are used to compute the solution instead. Furthermore, we obtain the same results for both the unsplit and split formulations of the PML equations. As it is shown, the acoustic pulse exits the boundaries with little visible reflection in the interior domain.

We further test the accuracy of the numerical solution by comparing it with the exact solution. In Figure 13 we plot the density along the line segment $y = 0$ at times $t = 6$ and 12 . We can see that the solutions obtained with the three IMEX schemes are in good agreement with the exact solution on the scale of the graph.

To evaluate the reflection error quantitatively, we will compare the numerical solution to a reference solution obtained by using a larger computational domain. In Figure 14 we plot the maximum difference between the numerical density solution and the reference density solution along the line segment defined by the points $(4.5, -4.5)$ and $(4.5, 4.5)$. This difference is normalized by A_0 which is the difference between the peak amplitude of density as it exits the right DVBE-PML interface and the mean flow density. The normalized maximum density difference is plotted as a function of time for different values of PML width D . As it is shown in the figure, when the width of the PML layer increases from $D = 10 \Delta x$ to $D = 20 \Delta x$, the reflection error

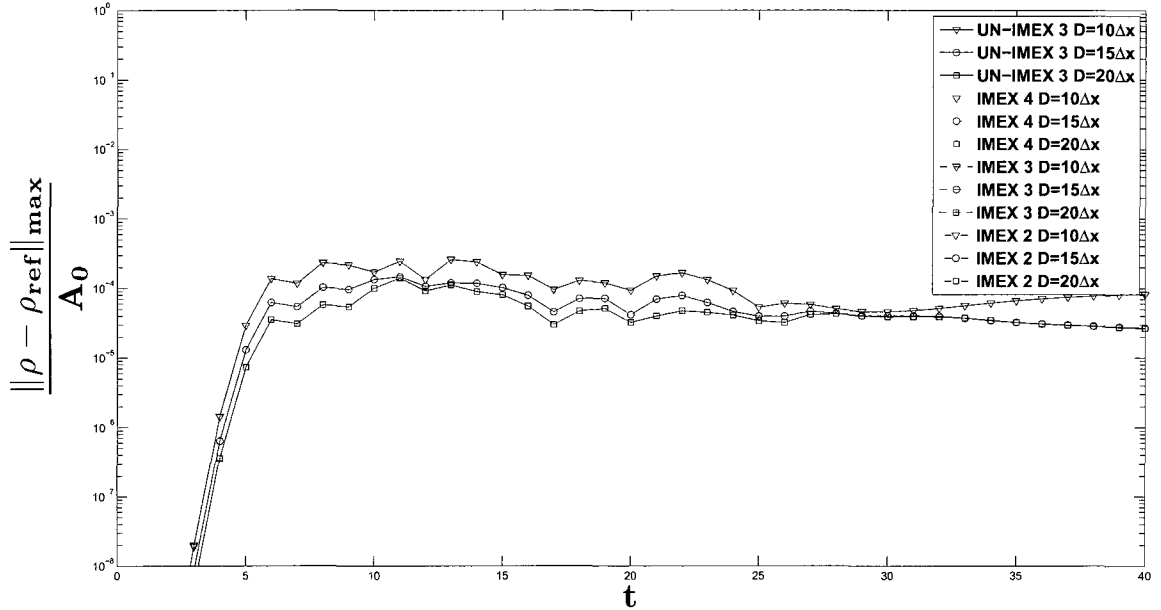


Fig. 14: Maximum difference between IMEX 3 and reference solution of acoustic density ρ versus time along the line segment defined by the points $(4.5, -4.5)$ and $(4.5, 4.5)$ for $\epsilon = 0.01$ and varying PML widths D .

is reduced. We can see that a reflection error of less than 0.1 percent is obtained with a PML width of 10 grid points with $D = 10 \Delta x$.

4.4.2 Two-Dimensional PML - Vorticity Wave

We also test the two-dimensional unsplit PML Eq. (47) and split PML Eqs. (57)-(59) by simulating a vorticity wave in a mean flow $(U_0, 0)$ with Mach number $M = 0.25$. Again, we consider the physical domain $[-5, 5] \times [-5, 5]$ with PML width $D = 10 \Delta x$ surrounding the boundaries and a relaxation time $\lambda = 0.00011$. The domain is discretized with a uniform grid $\Delta x = \Delta y = 0.1$. The initial conditions for density ρ and velocity components u and v are:

$$\rho = 1; \quad U_0 = Mc_s; \quad V_0 = 0 \quad (139)$$

$$u = U_0 + \epsilon y e^{-\ln 2 \frac{x^2 + y^2}{196}} \quad (140)$$

$$v = V_0 - \epsilon x e^{-\ln 2 \frac{x^2 + y^2}{196}} \quad (141)$$

In Figure 15 we plot the contours of the v -velocity at times $t = 5, 30$ and 50 for $\epsilon = 0.001$. We can see from the contour plots that the vorticity wave is effectively absorbed by the PML layer. To confirm the results, in Figure 16 we also compare the numerical solution along the line segment $y = 0$ to the exact solution at times $t = 5$ and 50 . The numerical solution for all three IMEX schemes is in good agreement with the exact solution at both times. To evaluate the reflection error quantitatively, again we compare the numerical solution to a reference solution obtained by using a larger computational domain. In Figure 17 we plot the maximum difference between the numerical v -velocity solution and the reference v -velocity solution along the line segment defined by the points $(4.5, -4.5)$ and $(4.5, 4.5)$. This difference is normalized by B_0 which is the peak amplitude of the v -velocity as it exits the right DVBE-PML interface. As the width of the PML layer increases from $D = 10 \Delta x$ to $D = 20 \Delta x$, the reflection error is reduced. For all three IMEX solutions, a reflection error of less than 0.2 percent is obtained with a PML width $D = 10 \Delta x$. In this example, unlike the acoustic example before, where the reflection error for split and unsplit PML formulations was indistinguishable from each other on the scale of the graph, the unsplit PML equations produce better results.

4.4.3 Three-Dimensional PML - Acoustic Wave

In this example, we test the unsplit PML equations (83) by simulating an acoustic wave in a mean flow $(U_0, 0)$ with Mach number $M = 0.25$. The physical domain under consideration is $[-2, 2] \times [-2, 2] \times [-2, 2]$ with PML width $D = 10 \Delta x$ and a relaxation time $\lambda = 0.00011$. The domain is discretized with a uniform grid $\Delta x = \Delta y = 0.1$. The initial conditions for density ρ and velocity components u, v and w are:

$$\rho = \rho_0 + \epsilon e^{-\ln 2 \frac{x^2 + y^2 + z^2}{0.25}} \quad (142)$$

$$u = Mc_s; \quad v = 0; \quad w = 0 \quad (143)$$

where $\rho_0 = 1$.

We first consider the effect of the factor β on the stability of the PML equations. For this, we plot the time evolution of the density norm given by

$$\|\rho\| = \left[\sum_i \sum_j \sum_l |\rho(i, j, l)|^3 \right]^{1/3} \quad (144)$$

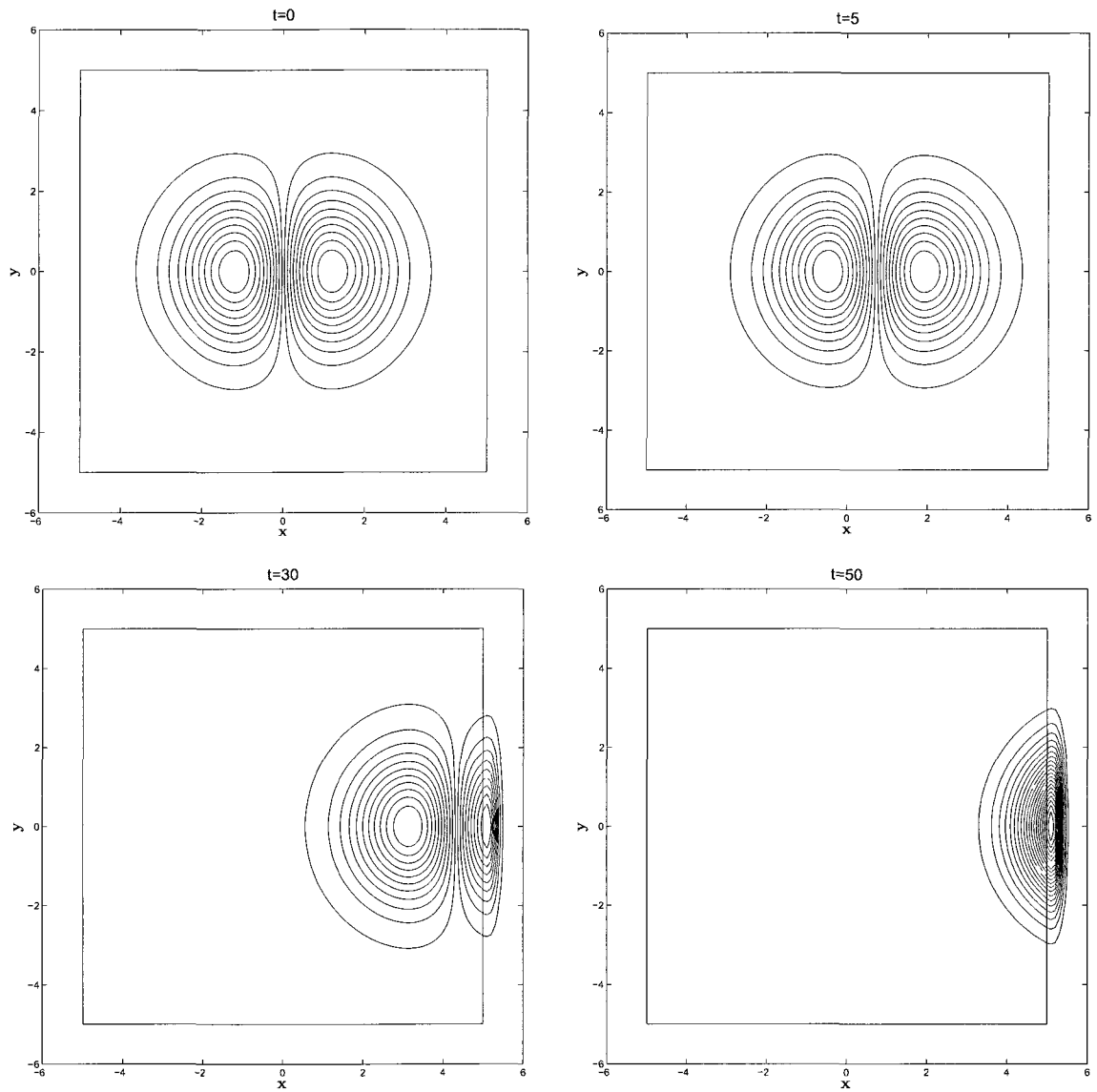


Fig. 15: Contours of IMEX 3 v -velocity at times $t = 0, 5, 30,$ and 50 for $\epsilon = 0.001$ showing the vorticity wave exiting the boundary without noticeable reflection.

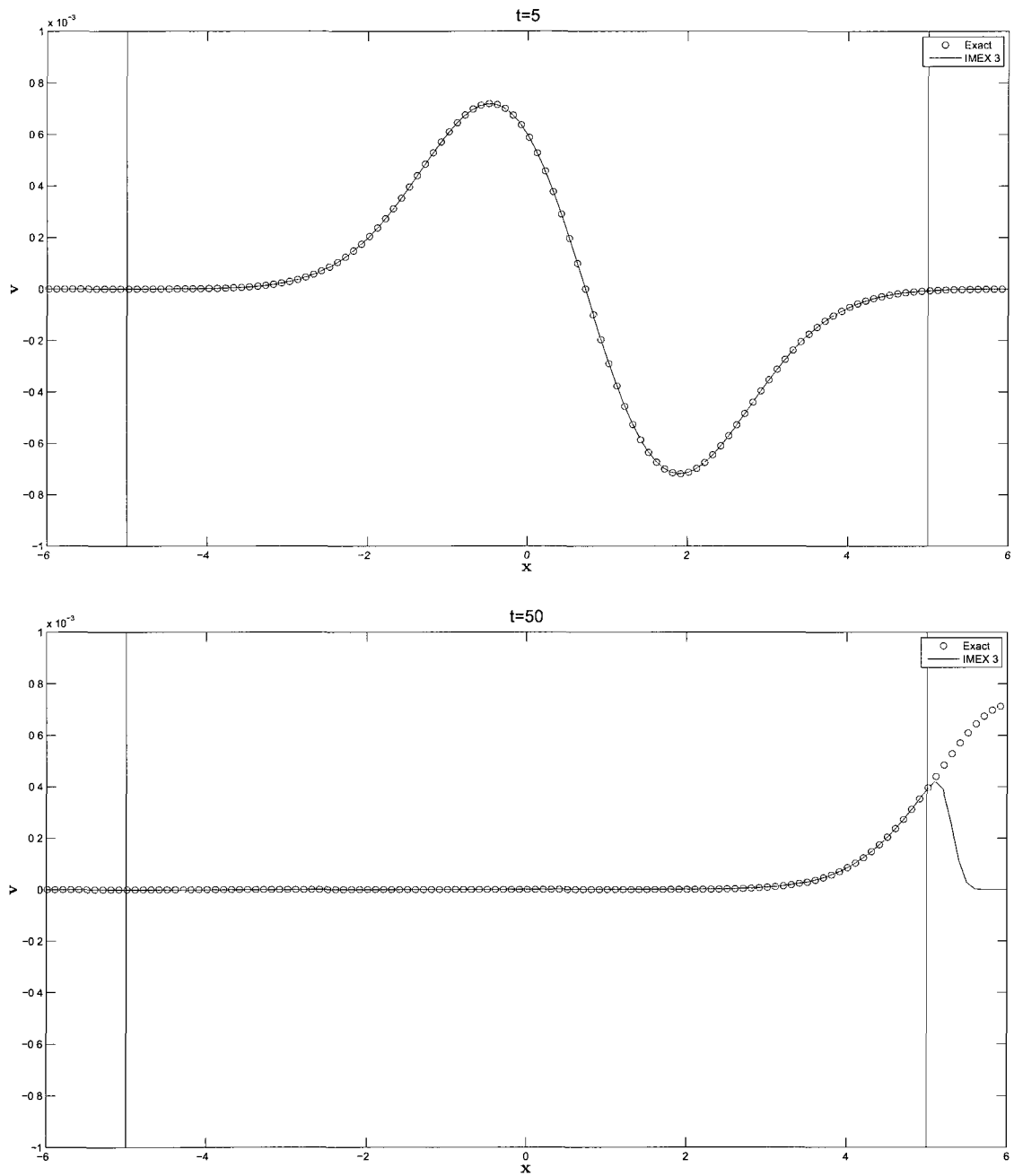


Fig. 16: Comparison of IMEX 3 numerical v -velocity vorticity solution with exact solution at times $t = 5$ and 50 for $\epsilon = 0.001$.

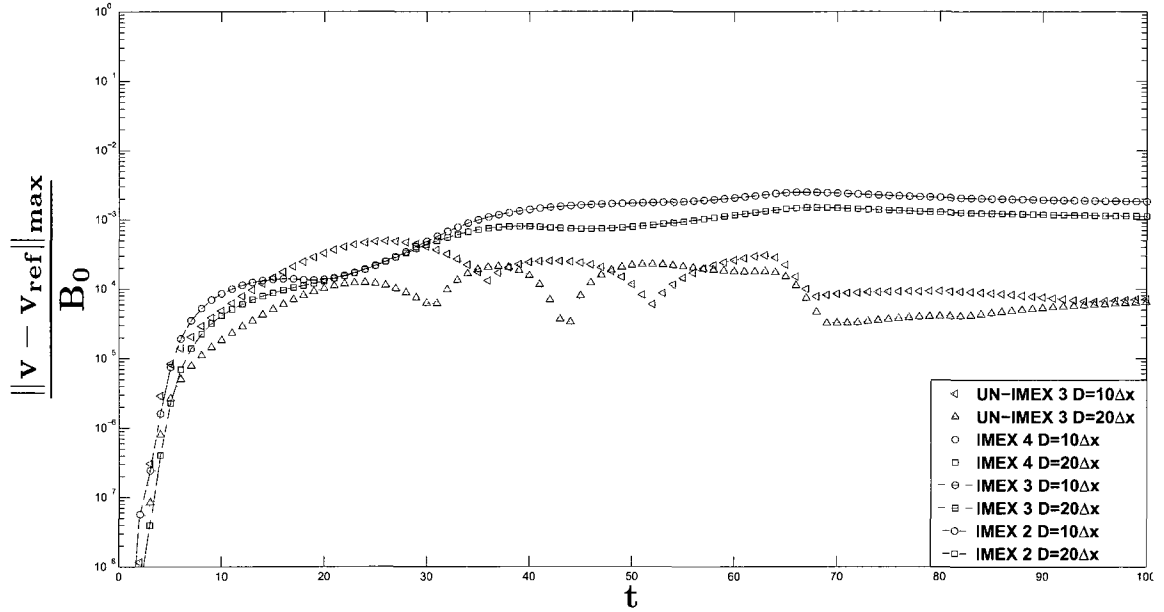


Fig. 17: Maximum difference between IMEX 3 and reference solution of vorticity v -velocity versus time along the line segment defined by the points $(4.5, -4.5)$ and $(4.5, 4.5)$ for $\epsilon = 0.001$ and varying PML widths D .

and normalized by the mean flow density norm $\|\rho_0\|$ for various values of β and time step $\Delta t = 0.9 \Delta x$, which is the limiting time step for stability. The results displayed in Figure 18 prove that the solution obtained with the value of β prescribed by Eq. (30) is more stable than the solutions obtained with other values of β .

In Figure 19 we show the contours of density at times $t = 0, 4, 6$ and 8 obtained with a time step $\Delta t = \Delta x$. The visible reflection is very small although the time step is larger than the time step required for stability.

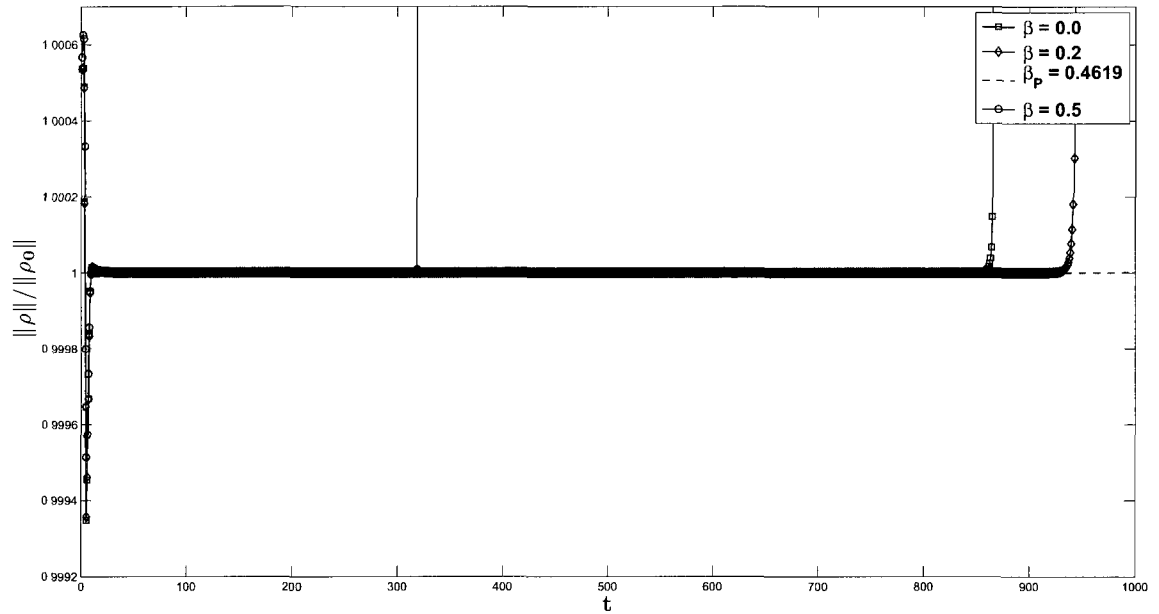


Fig. 18: Scaled norm of unsplit PML IMEX 3 acoustic density ρ versus time for $\epsilon = 0.1$, $\Delta t = 0.9 \Delta x$ showing the significance of the factor β for the stability of the PML equations. The most stable solution of those shown is the solution obtained with the prescribed value $\beta_P = 0.4619$.

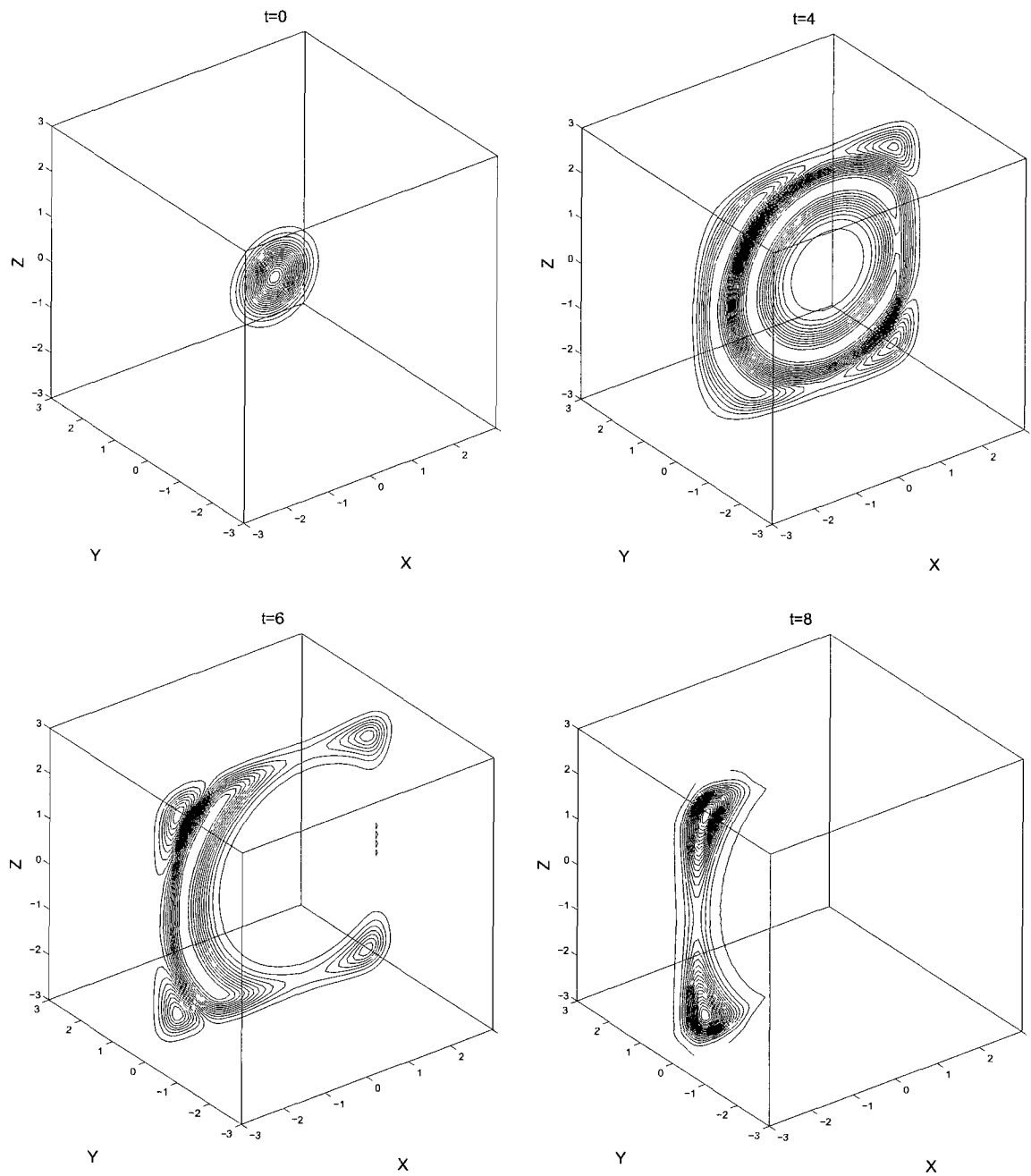


Fig. 19: Contours of unsplit PML IMEX 3 density at times $t = 0, 4, 6,$ and 8 for $\epsilon = 0.1$ showing the acoustic wave exiting the boundaries with small reflection.

CHAPTER 5

LATTICE SOLUTION OF PML EQUATIONS

5.1 THE LATTICE BOLTZMANN EQUATION

The lattice Boltzmann (LB) equation was originally derived from its boolean counterpart, the lattice-gas automata (LGA). The first LGA model to simulate the Navier-Stokes equations was independently proposed by Frisch et al. and Wolfram in 1986 [79, 80]. This model, commonly referred to as the FHP model, is comprised of a two dimensional triangular lattice and Boolean particles possessing momenta which allow them to move from one lattice site to another in discrete time steps. At each lattice site there is either no particle or at most six particles simultaneously, one for each of its six neighboring sites. The evolution of the Boolean particle numbers is described by a collision followed by the advection of particles to the next site according to their velocities. The collision process describes the possible incoming and outgoing configurations at each site based on a set of collision rules that ensure the conservation of particle number, momentum, and energy.

Since the hydrodynamics described by LGA methods are intrinsically noisy due to large fluctuations in Boolean particle number, they show a lack Galilean invariance, and conserve spurious quantities due to their simple symmetry, better alternatives were sought [81]. One such alternative was proposed by McNamara and Zanetti in 1988 in the form of the lattice Boltzmann equation [82]. This LB equation was obtained by replacing the Boolean number fields in the corresponding LGA with ensemble averages. It is worth pointing out that the collision operator was initially based on its LGA predecessor and only later models used the BGK collision model. Also, the equilibrium distribution functions were Fermi-Dirac functions and not the Maxwell-Boltzmann functions of current LB models. More recently, He and Luo were able to show that the LB equation can be derived as a special discretization of the continuous Boltzmann equation [3, 4].

An important distinction between the lattice Boltzmann (LB) equation and the discrete velocity Boltzmann equation (DVBE) can be found in the procedure used for the space and time discretizations. In LB models, the velocity set used to discretize momentum space is chosen in such a way that a lattice structure is obtained simultaneously for space and time [81]. The space and time discretizations of the

DVBE, on the other hand, are independent of each other. To see this more clearly, let us consider one procedure by which the LB equation can be derived. The procedure outlined below involves a space and time discretization of the discrete velocity Boltzmann equation followed by a change of variables [83]. We begin by writing the discrete velocity Boltzmann-BGK equation in component form

$$\frac{\partial f_i}{\partial t} + \boldsymbol{\xi}_i \cdot \nabla f_i = -\frac{1}{\lambda} (f_i - f_i^{eq}) \quad (145)$$

If we integrate Eq. (145) for a time interval Δt along a characteristic of the form

$$\mathbf{r}(s) = (\mathbf{x} + \boldsymbol{\xi}_i s, t + s) \quad (146)$$

we obtain

$$f_i(\mathbf{x} + \boldsymbol{\xi}_i \Delta t, t + \Delta t) - f_i(\mathbf{x}, t) = -\frac{1}{\lambda} \int_0^{\Delta t} (f_i(\mathbf{x} + \boldsymbol{\xi}_i s, t + s) - f_i^{eq}(\mathbf{x} + \boldsymbol{\xi}_i s, t + s)) ds \quad (147)$$

An approximation of the above integral by the trapezoid rule with second order accuracy will results in

$$f_i(\mathbf{x} + \boldsymbol{\xi}_i \Delta t, t + \Delta t) - f_i(\mathbf{x}, t) = -\frac{\Delta t}{2\lambda} (f_i(\mathbf{x} + \boldsymbol{\xi}_i \Delta t, t + \Delta t) - f_i^{eq}(\mathbf{x} + \boldsymbol{\xi}_i \Delta t, t + \Delta t)) - \frac{\Delta t}{2\lambda} (f_i(\mathbf{x}, t) - f_i^{eq}(\mathbf{x}, t)) + \mathcal{O}(\Delta t^3) \quad (148)$$

Since $f_i^{eq}(\mathbf{x} + \boldsymbol{\xi}_i \Delta t, t + \Delta t)$ depends on the set $f_i(\mathbf{x} + \boldsymbol{\xi}_i \Delta t, t + \Delta t)$, we have a system of coupled nonlinear algebraic equations for f_i at time $t + \Delta t$. If we recast Eq. (148) in the following form

$$f_i(\mathbf{x} + \boldsymbol{\xi}_i \Delta t, t + \Delta t) + \frac{\Delta t}{2\lambda} (f_i(\mathbf{x} + \boldsymbol{\xi}_i \Delta t, t + \Delta t) - f_i^{eq}(\mathbf{x} + \boldsymbol{\xi}_i \Delta t, t + \Delta t)) - f_i(\mathbf{x}, t) - \frac{\Delta t}{2\lambda} (f_i(\mathbf{x}, t) - f_i^{eq}(\mathbf{x}, t)) = -\frac{\Delta t}{\lambda} (f_i(\mathbf{x}, t) - f_i^{eq}(\mathbf{x}, t)) \quad (149)$$

and then apply the change of variables

$$\tilde{f}_i(\mathbf{x}, t) = f_i(\mathbf{x}, t) + \frac{\Delta t}{2\lambda} (f_i(\mathbf{x}, t) - f_i^{eq}(\mathbf{x}, t)) \quad (150)$$

we obtain

$$\tilde{f}_i(\mathbf{x}, t) - f_i^{eq}(\mathbf{x}, t) = f_i(\mathbf{x}, t) + \frac{\Delta t}{2\lambda} (f_i(\mathbf{x}, t) - f_i^{eq}(\mathbf{x}, t)) - f_i^{eq}(\mathbf{x}, t) \quad (151)$$

or equivalently

$$\tilde{f}_i(\mathbf{x}, t) - f_i^{eq}(\mathbf{x}, t) = \frac{\lambda + \frac{\Delta t}{2}}{\lambda} (f_i(\mathbf{x}, t) - f_i^{eq}(\mathbf{x}, t)) \quad (152)$$

Finally, we obtain the explicit system for \tilde{f}_i , i.e. the lattice Boltzmann equation as

$$\tilde{f}_i(\mathbf{x} + \boldsymbol{\xi}_i \Delta t, t + \Delta t) - \tilde{f}_i(\mathbf{x}, t) = -\frac{\Delta t}{\lambda + \frac{\Delta t}{2}} (\tilde{f}_i(\mathbf{x}, t) - f_i^{eq}(\mathbf{x}, t)) \quad (153)$$

As in the case of its LGA predecessors, the lattice Boltzmann equation can be implemented in two steps, a local collision process given by

$$\tilde{f}_i^*(\mathbf{x}, t) = \tilde{f}_i(\mathbf{x}, t) - \frac{\Delta t}{\lambda + \frac{\Delta t}{2}} (\tilde{f}_i(\mathbf{x}, t) - f_i^{eq}(\mathbf{x}, t)) \quad (154)$$

and a streaming from node to node described by

$$\tilde{f}_i(\mathbf{x} + \boldsymbol{\xi}_i \Delta t, t + \Delta t) = \tilde{f}_i^*(\mathbf{x}, t) \quad (155)$$

The fact that only previous neighboring node information is required to advance the solution to the next time step accounts for some of the attractive properties of the LBE method, namely the straightforward implementation, fast evolution, and adaptability to parallel architectures. Since the time integration used in the above derivation of the lattice Boltzmann equation is done along a characteristic line defined in terms of the velocity $\boldsymbol{\xi}$, the discretizations of space and time are no longer independent of each other. As we will see in the next section, this affects the stability of the PML equations when the LB method is used to solve them.

5.2 LINEAR ANALYSIS OF LATTICE PML

The interdependence of the velocity, space, and time discretizations in the LB equation poses difficulties when we want to solve the PML equations by this method. The equations for the PML variables cannot be solved using the collision and streaming steps as with the LB method, but have to be computed by a finite difference scheme instead. We propose the following lattice formulation for the PML Eqs. (57), (58), and (59)

$$\begin{aligned}
f_i(\mathbf{x} + \boldsymbol{\xi}_i \Delta t, t + \Delta t) - f_i(\mathbf{x}, t) &= -\frac{\Delta t}{\lambda + \frac{\Delta t}{2}}(f_i(\mathbf{x}, t) - f_i^{eq}(\mathbf{x}, t)) - \Delta t \sigma_x q_{1i}(\mathbf{x}, t) \\
&\quad - \Delta t \sigma_y q_{2i}(\mathbf{x}, t) - \Delta t \sigma_x \beta u_i(f_i(\mathbf{x}, t) - \bar{f}_i^{eq}(\mathbf{x}, t))
\end{aligned} \tag{156}$$

$$\begin{aligned}
q_{1i}(\mathbf{x}, t + \Delta t) - q_{1i}(\mathbf{x}, t) &= -\Delta t \sigma_x q_{1i}(\mathbf{x}, t) - \Delta t u_i \frac{\partial(f_i(\mathbf{x}, t) - \bar{f}_i^{eq}(\mathbf{x}, t))}{\partial x} \\
&\quad - \Delta t \sigma_x \beta u_i(f_i(\mathbf{x}, t) - \bar{f}_i^{eq}(\mathbf{x}, t))
\end{aligned} \tag{157}$$

$$\begin{aligned}
q_{2i}(\mathbf{x}, t + \Delta t) - q_{2i}(\mathbf{x}, t) &= -\Delta t \sigma_y q_{2i}(\mathbf{x}, t) - \Delta t v_i \frac{\partial(f_i(\mathbf{x}, t) - \bar{f}_i^{eq}(\mathbf{x}, t))}{\partial y}
\end{aligned} \tag{158}$$

To investigate the stability of the lattice formulation, again we study the linear stability of the PML equations. For the lattice formulation, the linear analysis gives the following eigenvalue problem

$$\begin{pmatrix} \mathbf{C} \left[\mathbf{I} - \frac{\Delta t}{\lambda + \frac{\Delta t}{2}}(\mathbf{I} - \mathbf{J}) - \Delta t \sigma_x \beta \mathbf{A} \right] & -\Delta t \sigma_x \mathbf{C} & -\Delta t \sigma_y \mathbf{C} \\ [-ik_x \Delta t - \Delta t \sigma_x \beta] \mathbf{A} & [1 - \Delta t \sigma_x] & 0 \\ -ik_y \Delta t \mathbf{B} & 0 & [1 - \Delta t \sigma_y] \end{pmatrix} \hat{\mathbf{F}} = \hat{\mathbf{F}} e^{-i\omega \Delta t} \tag{159}$$

where \mathbf{C} is the diagonal matrix defined as $C_{jj} = e^{-i\mathbf{k} \cdot \boldsymbol{\xi}_j \Delta t}$ and the matrices \mathbf{I} , \mathbf{A} , \mathbf{B} and \mathbf{J} are as previously defined.

The eigenvalue analysis proves the existence of eigenvalues with positive imaginary parts that cannot be overcome even by filtering, showing that the proposed lattice formulation will yield unstable PML layers. This fact has also been confirmed in simulations. We used various finite difference schemes, including the DRP, but in all examples, the solution was highly unstable. A combination of a second order centered low pass filter for the PML domains and a tenth order low pass filter for the LB domain stabilized the solution somewhat so the acoustic and vorticity waves could be observed exiting the boundaries. However, compared to the finite difference solutions presented in the previous chapter, the results are poor as evident from Figures 20, 21, 22, and 23.

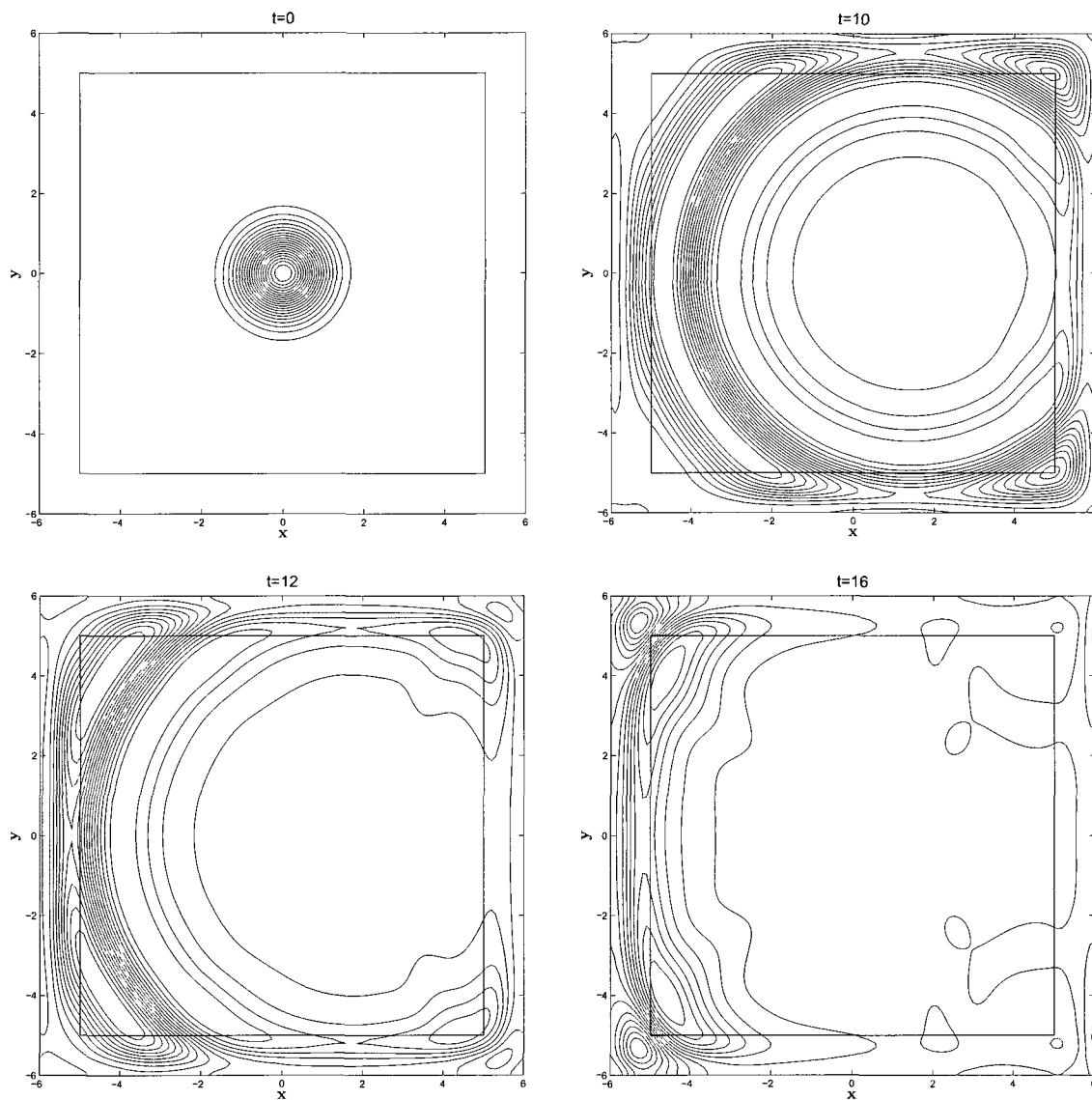


Fig. 20: Contours of LB density at times $t = 0, 10, 12,$ and 16 for $\epsilon = 0.01$ showing the reflections generated by the acoustic wave exiting the boundary.

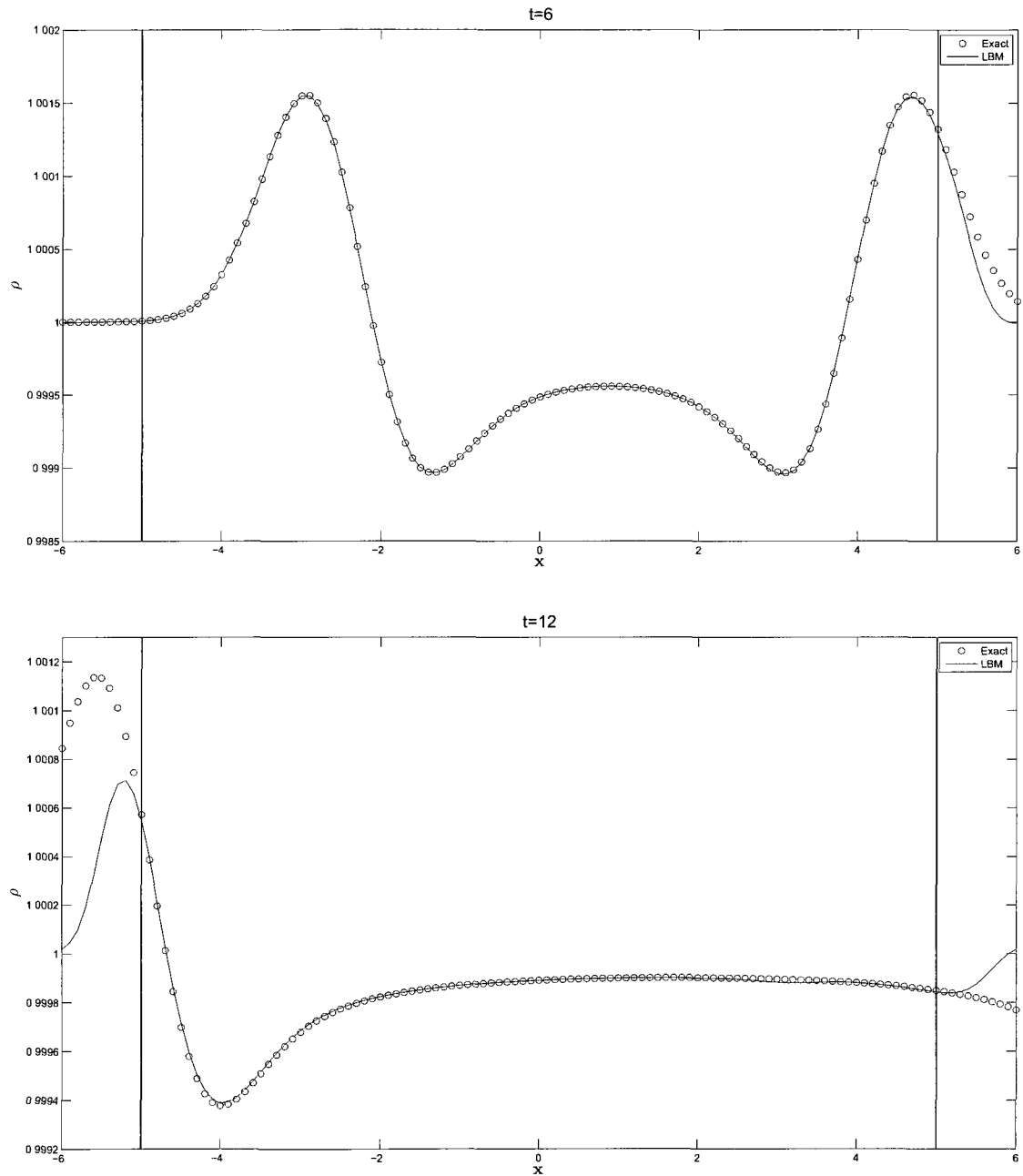


Fig. 21: Comparison of LB numerical acoustic density solution with exact solution at times $t = 6$ and 12 for $\epsilon = 0.01$.

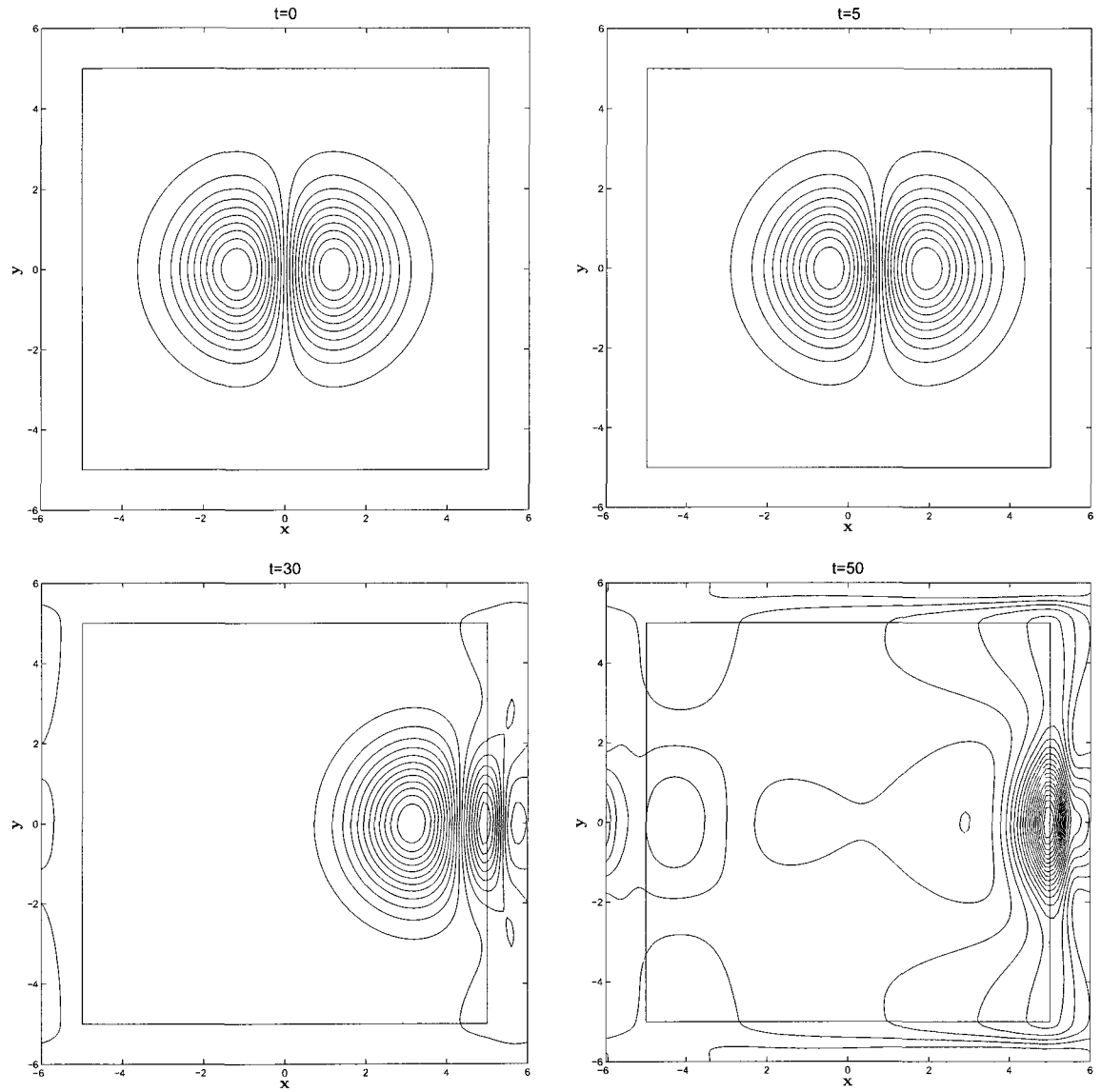


Fig. 22: Contours of LB v -velocity at times $t = 0, 5, 30,$ and 50 for $\epsilon = 0.001$ showing the reflections generated by the vorticity wave exiting the boundary.

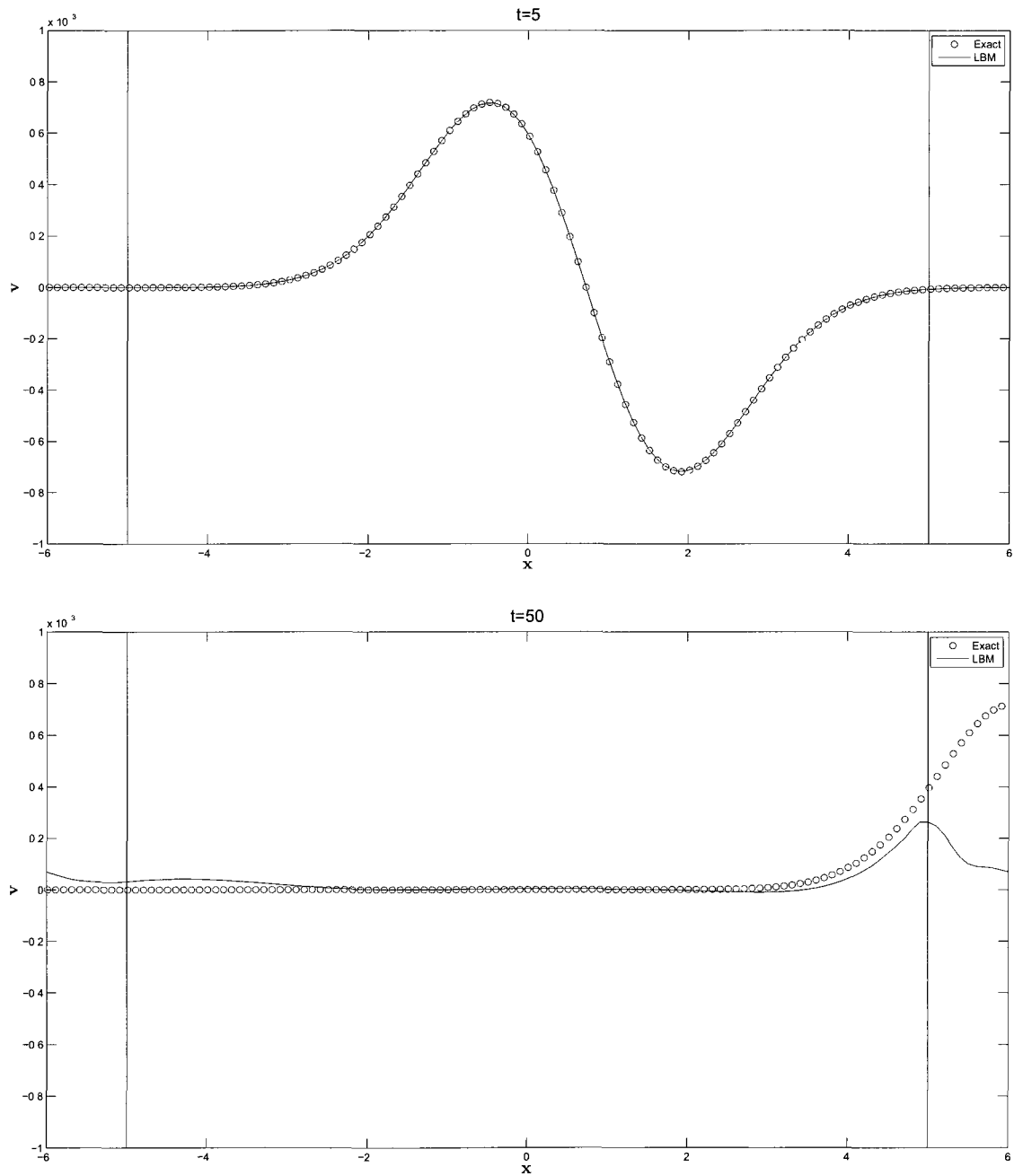


Fig. 23: Comparison of LB numerical v -velocity vorticity solution with exact solution at times $t = 5$ and 50 for $\epsilon = 0.001$.

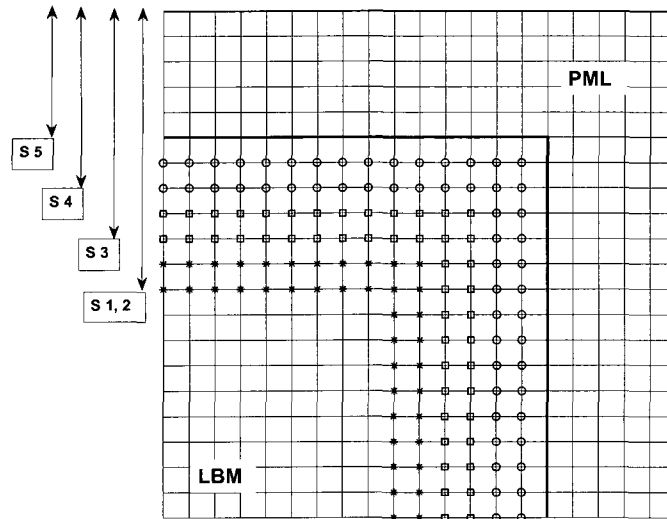


Fig. 24: Diagram of LB-IMEX 3 coupling for a 5-point finite difference stencil.

5.3 COUPLED SOLUTION

As the lattice discretization of the PML equations produces highly unstable results, in order to use the PML equations in conjunction with the lattice Boltzmann method, we formulate a mixed LB and finite difference method to which we will henceforth refer to as the coupled method. In the coupled method, the unsplit PML equations are solved by finite differences using the third order IMEX scheme for the time integration while the interior domain solution is obtained by solving the LB equation. Since the finite difference solution obtained with the third order IMEX scheme is stable for a ratio $\Delta t/\Delta x = 1$, the coupling of the two methods at the PML interface is fairly straightforward.

To advance the solution to next time step, the finite difference solution in the PML domains is obtained first. Periodic boundary conditions are used for the outer PML boundaries while the interior interface solution is obtained using previous interior LB function values. In order to minimize the grid to grid oscillations at the interior domain and PML interface, we require that the interface solution be updated from previous finite difference function values only. This requirement makes it necessary to obtain the finite difference solution for additional interior grid points beside the

PML. The implementation will vary depending on the finite difference scheme used.

To illustrate how the coupling is implemented, we will consider a five point centered finite difference scheme. In order to advance the PML solution, represented in Figure 24 by S5, we need to compute the derivatives of the fourth stage PML solution in the IMEX scheme. Since only finite difference function values are permitted, the interface solution will require that the stage four solution be obtained for two additional interior grid points. This is due to the fact that the five point stencil at the interface grid point will use the solution of two interior grid points and two PML grid points. The stage four PML solution and the solution for the two additional grid points is represented by S4 in Figure 24. Similarly, to obtain the stage four solution, S4, we will need the derivatives of stage three values for the PML and an additional four interior grid points, as represented by S3. Finally, since the stage three solution will make use of the derivatives of the stage two solution and stage one is necessary to obtain the stage two solution, it follows that stages one and two will have to be computed for the PML domains and an additional six interior grid points as symbolized by S1,2 in the diagram.

Once the finite difference solution is obtained for the PML domains as outlined above, the LBM solution is calculated for the interior domain. It should be noted that the interface finite difference solution becomes the boundary condition for the LB streaming step. In the numerical examples that follow, again we used the DRP finite difference scheme which requires nine additional interior grid points for the coupling of the two solutions. Even so, there will still be oscillations at the grid point near the interface which may cause instability. Figure 25 shows that this coupling is stable when a tenth order centered low pass filter is applied to the entire solution.

5.4 NUMERICAL EXAMPLES

5.4.1 ACOUSTIC WAVE

To test the LB-IMEX 3 coupled method, we will use the same examples and the same parameters as in Chapter 4 so that we can compare its performance with the performance of the finite difference model. We plot the density contours for the acoustic wave at $t = 0, 10, 12,$ and 16 for $\Delta x = \Delta y = \Delta t = 0.1$ in Figure 26 and we compare the numerical solution with the exact solution at $t = 6$ and 16 in Figure 27. As can be observed in these figures, the absorption of the acoustic wave

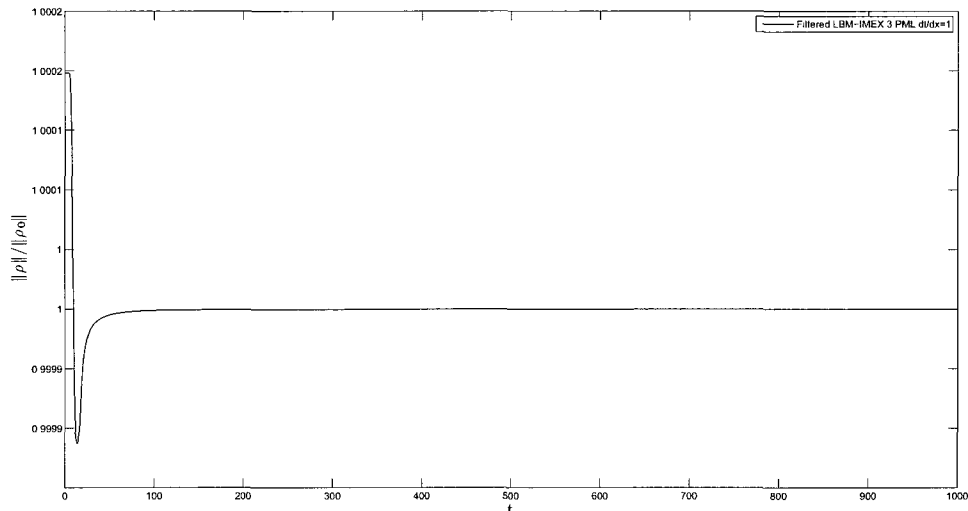


Fig. 25: Scaled norm of filtered LB-IMEX 3 acoustic density ρ versus time for $\epsilon = 0.1$ and $\Delta x = \Delta y = \Delta t = 0.1$.

is not as good as in the finite difference case but the reflection generated by the coupling is still very small. For a quantitative evaluation of accuracy, we plot the maximum difference between the numerical density solution and a reference solution along the line segment defined by the points $(4.5, -4.5)$ and $(4.5, 4.5)$ for different values of PML width D . The plotted maximum difference of density is relative to the amplitude, A_0 , of the outgoing wave as it exits the right boundary. As the PML width is increased from $D = 10 \Delta x$ to $D = 20 \Delta x$ the maximum reflection error is constant. This indicates that the error generated by the coupling of the LB method with the IMEX 3 PML is dominating the reflection error. Still, a reflection error of less than 2 percent is obtained for the range of PML widths considered.

5.4.2 VORTICITY WAVE

In Figure 29, we plot the contours of the v -velocity at $t = 0, 5, 30,$ and 50 for $\epsilon = 0.001$. We can see from the contour plots that the vorticity wave is effectively absorbed by the PML layer. The coupled solution compares very well with the exact solution at $t = 5$ and 50 , as illustrated in Figure 30. The fact that the vorticity results are in better agreement with the exact solution than the acoustic results is consistent with the reflection coefficient results obtained in Chapter 4 where the unsplit IMEX

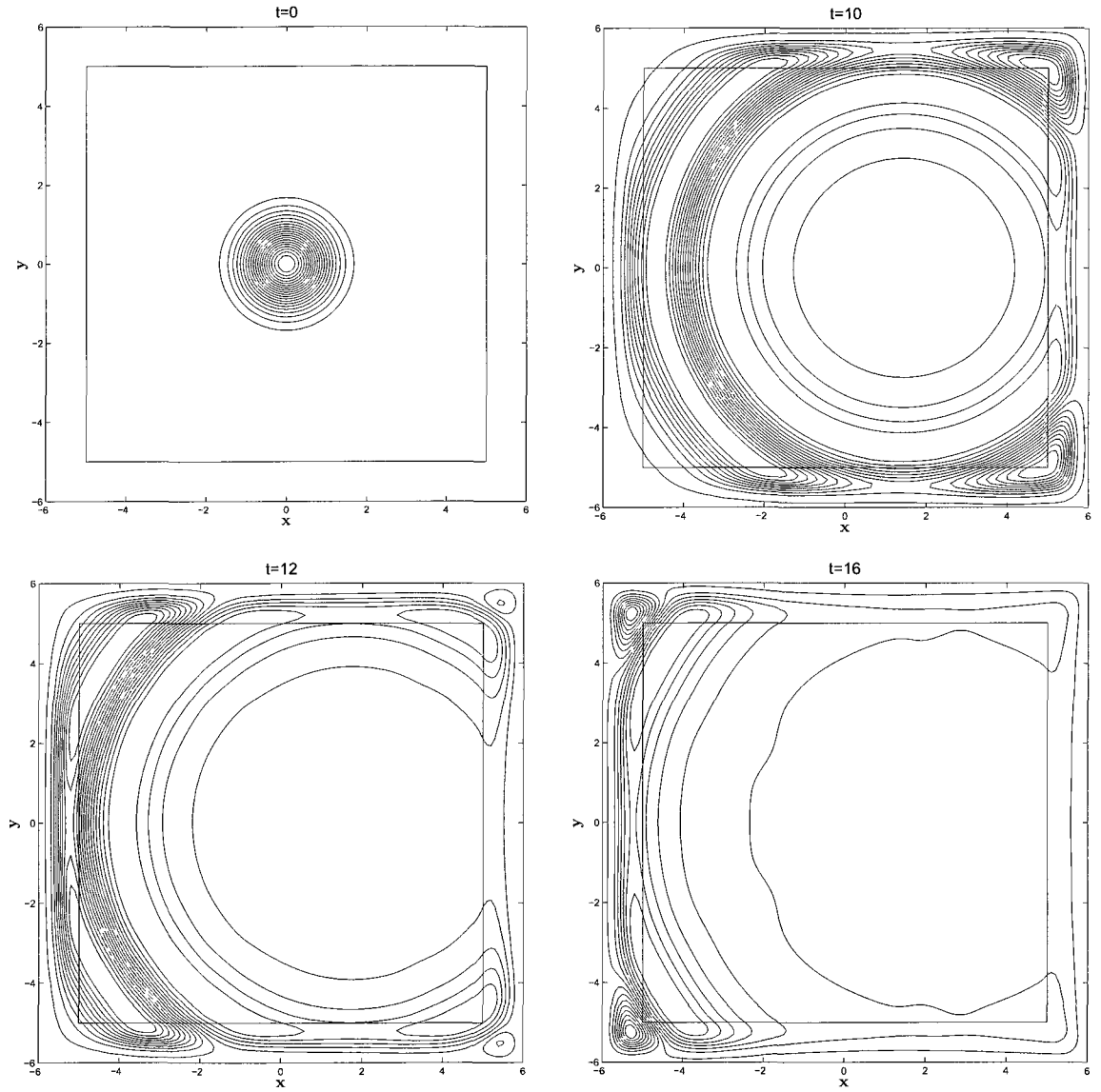


Fig. 26: Contours of LB-IMEX 3 density at times $t = 0, 10, 12,$ and 16 for $\epsilon = 0.01$ showing the acoustic wave exiting the boundary with small reflection.

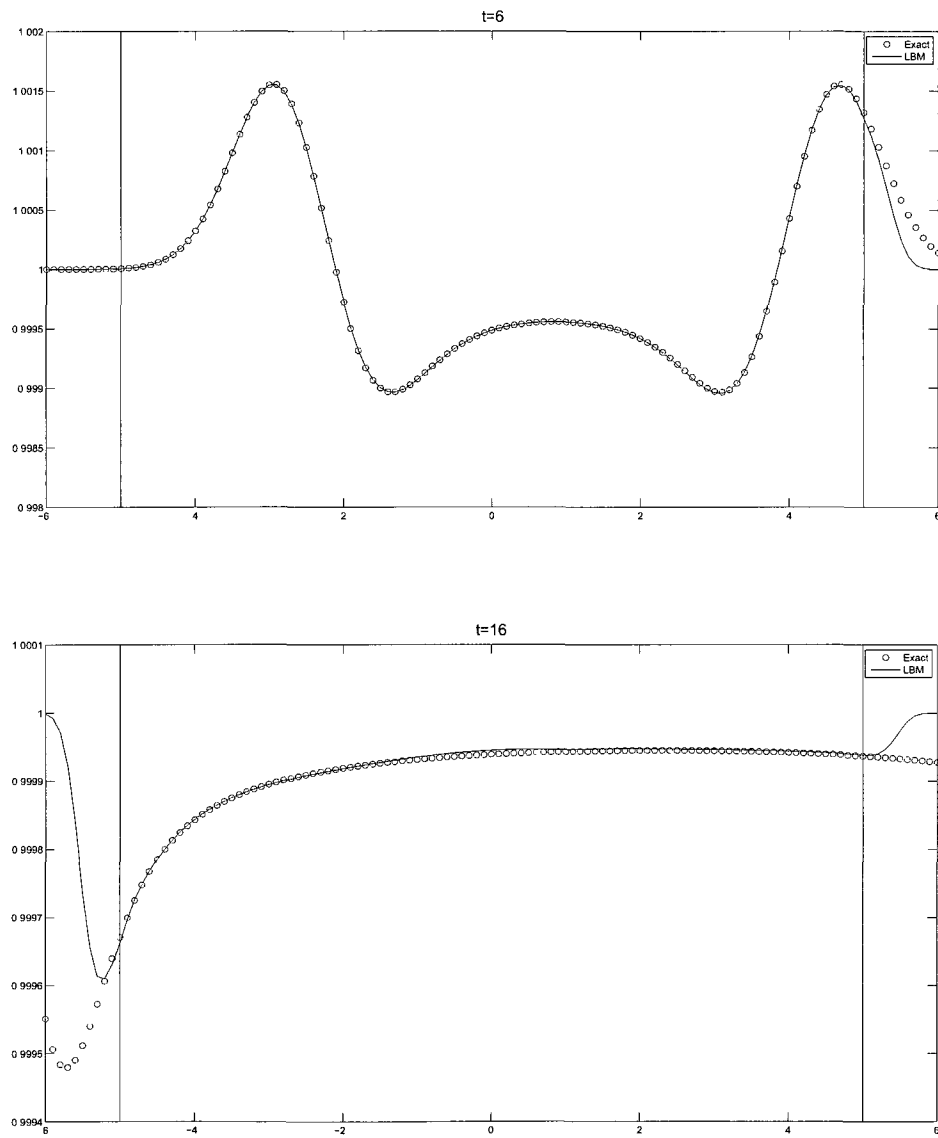


Fig. 27: Comparison of LB-IMEX 3 numerical acoustic density solution with exact solution at times $t = 6$ and 12 for $\epsilon = 0.01$.

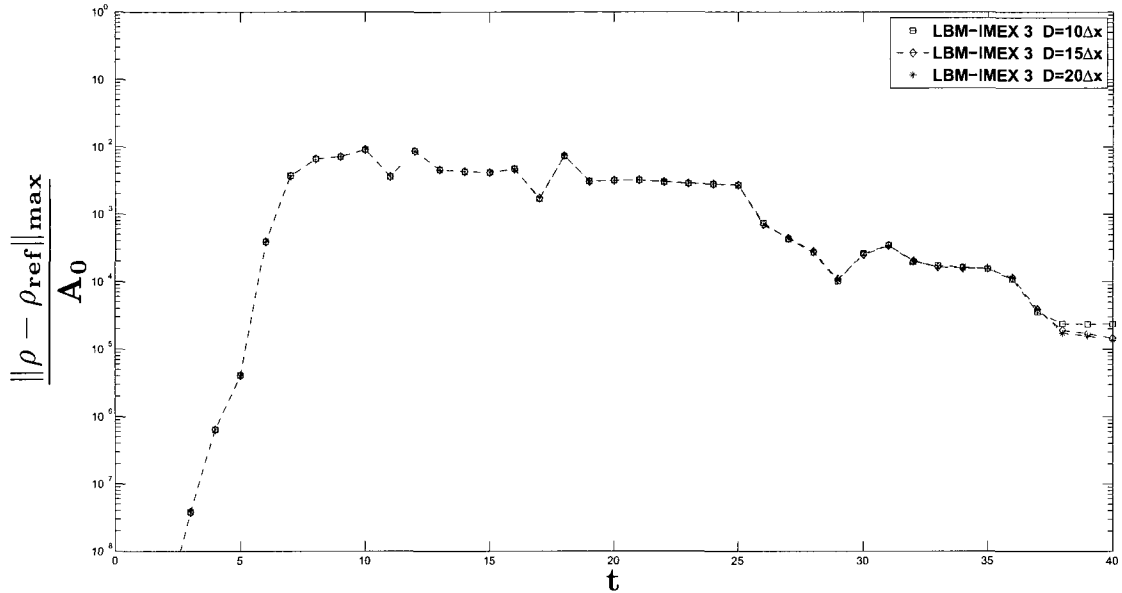


Fig. 28: Maximum difference between LB-IMEX 3 and reference solution of acoustic density ρ versus time along the line segment defined by the points $(4.5, -4.5)$ and $(4.5, 4.5)$ for $\epsilon = 0.01$ and varying PML widths D .

3 PML formulation gave the same results as the split IMEX 3 PML formulation in the acoustic example, but produced better results in the vorticity example. These similarities are due to the fact that we used the unsplit PML equations for the coupled method. The maximum difference between the numerical and reference v -velocity along the line segment defined by the points $(4.5, -4.5)$ and $(4.5, 4.5)$ as a function of time is plotted in Figure 31 for different values of PML width D . Again, the difference is normalized by the peak amplitude, B_0 of the v -velocity as it exits the right LB-PML interface. A reflection error of less than one percent is obtained for all of the PML widths considered, showing that the coupled method can be used effectively in conjunction with the LB method.

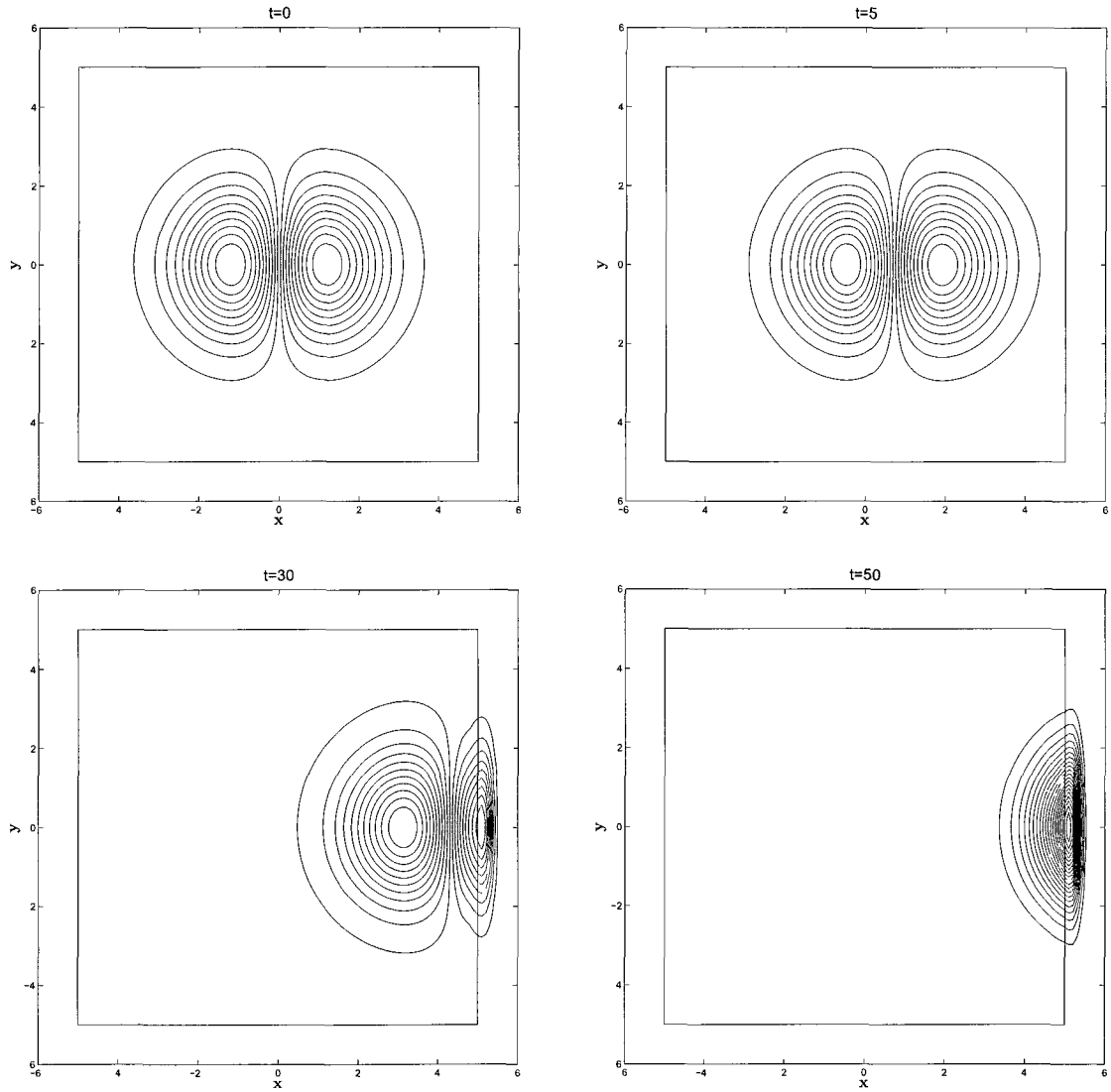


Fig. 29: Contours of LB-IMEX 3 v -velocity at times $t = 0, 5, 30,$ and 50 for $\epsilon = 0.001$ showing the vorticity wave exiting the boundary with small reflection.

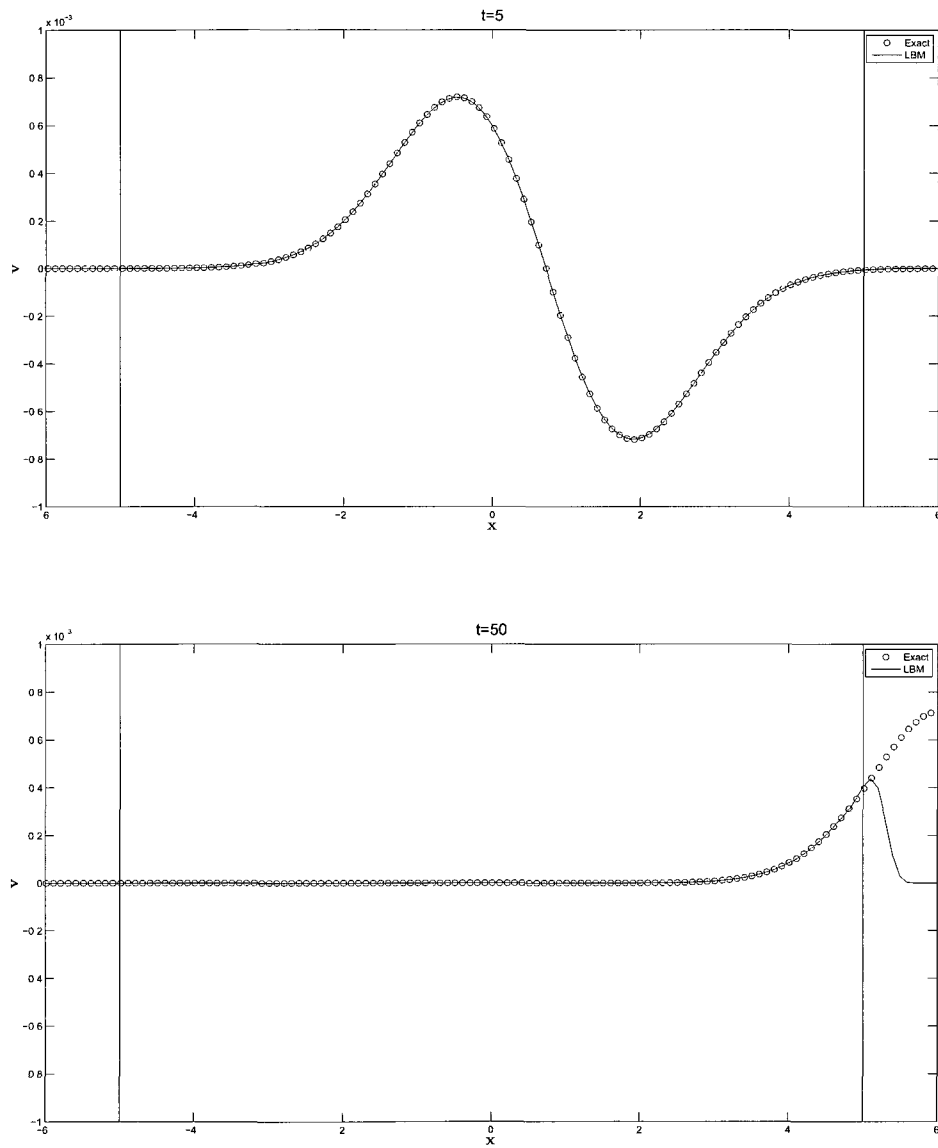


Fig. 30: Comparison of LB-IMEX 3 numerical v -velocity vorticity solution with exact solution at times $t = 5$ and 50 for $\epsilon = 0.001$.

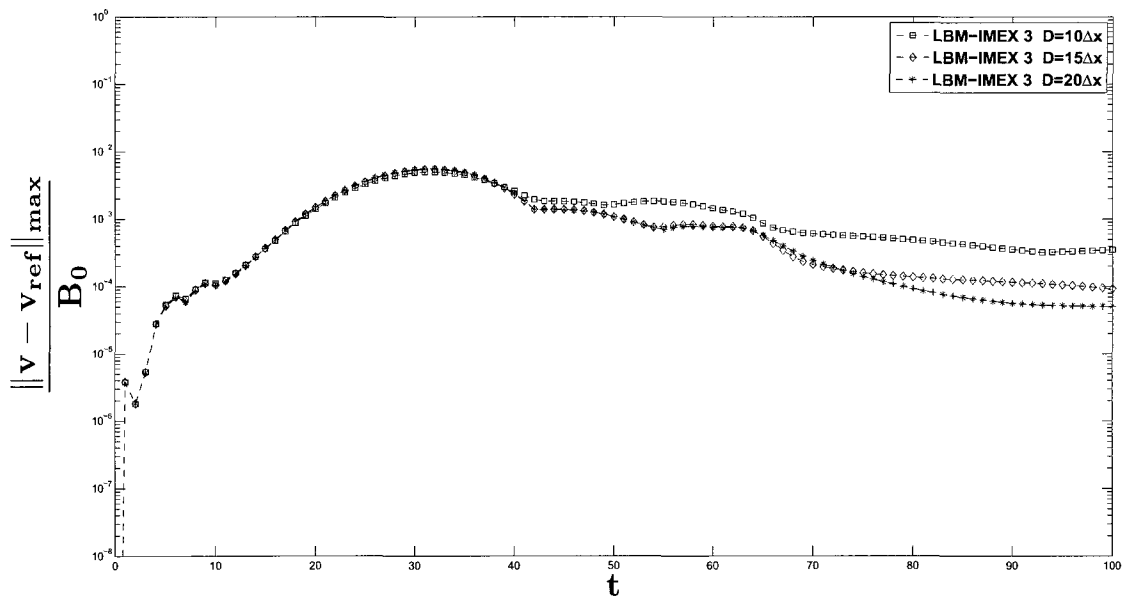


Fig. 31: Maximum difference between LB-IMEX 3 and reference solution of vorticity v -velocity versus time along the line segment defined by the points $(4.5, -4.5)$ and $(4.5, 4.5)$ for $\epsilon = 0.001$ and varying PML widths D .

CHAPTER 6

CONCLUDING REMARKS

In recent years, methods based on the Boltzmann-BGK equation have been intensely studied not only as an alternative to the Navier-Stokes equations, but also for their applicability in cases where the macroscopic governing equations are difficult or impossible to solve. Instead of having to solve multiple transport equations as in the case of Navier-Stokes or Euler equations, only one transport equation for the distribution function needs to be solved for the Boltzmann-BGK models. The flow properties are then obtained by integrating the distribution function over the particle velocity space. Furthermore, qualitatively good results can be obtained even when the velocity space is reduced to a very small number of discrete velocities. As more effective discrete velocity Boltzmann-BGK models are being developed and their capability is extended to simulate aeroacoustics phenomena with increasingly better accuracy, the research and development of accurate numerical boundary conditions becomes more imperative. For the Euler and Navier-Stokes equations, the Perfectly Matched Layer method has been shown to produce highly accurate non-reflective boundary conditions that preserve well the accuracy of the solution in the interior domain. In this work, Perfectly Matched Layer absorbing boundary conditions have been derived for the discrete velocity Boltzmann-BGK equation in two and three dimensions for the case of horizontal mean flow. Both split and unsplit formulations of the PML equations have been shown to produce satisfactory numerical results.

There are several benefits to using Perfectly Matched Layers over other non-reflective boundary conditions, the most important of which is its improved accuracy. Since the PML equations are perfectly matched to the governing equations at the boundary of the numerical domain, the boundary reflection errors are greatly reduced, and, as a result, the overall error of the numerical solution is decreased. A reduction in computational cost is another advantage of the Perfectly Matched Layer especially when we compare it to asymptotic boundary conditions which require a large computational domain to maintain the validity of the far field solution. Because the solution in other buffer zones must be changed in a gradual fashion to prevent reflections being generated inside the zone itself and because these methods are prone to reflections at the interface of the buffer layer and the computational domain, they tend to be larger and less efficient than the PML domains. The accuracy

of characteristic boundary conditions depends on the angle of incidence with which waves exit the computational domain. When the waves are normal to the boundaries, characteristic boundary conditions are very accurate, but as the angle of incidence is increased, their accuracy declines. As a result, characteristic boundary conditions would not be good candidates for further extension to the case of oblique mean flows.

The PML equations presented in this work for the discrete velocity Boltzmann-BGK equation are more general than those previously proposed by Najafiyazdi and Mongeau [52] in the sense that we made no restrictive assumptions in regards to the absorption coefficients or the numerical schemes used for the spatial derivatives. As long as the desired level of accuracy is obtained, any finite difference scheme can be used to solve the PML equations. The choice of finite difference scheme in this work has been motivated by the fact that DRP schemes preserve the wavemodes of the original governing equations, and, as a result, they are better than other schemes for aeroacoustics applications.

As demonstrated in the numerical examples, both the finite difference and the coupled method for solving the PML equations can produce accurate results. However, there are some considerations to be made before choosing between the two. If accuracy and stability are the main concern, then the finite difference method is by far the better choice. Since finite differences are used to obtain both the interior domain and the PML solutions, the two solutions are better matched at the interface so they are stable and produce more accurate results. If, on the other hand, the computational domain contains complicated geometrical constructs or if the goal is a faster and computationally inexpensive method, then the coupled scheme is more suitable because the LB method is faster, more efficient, and more adaptable to complicated geometry.

It is important to note that although the stated objectives for this dissertation have been accomplished, the applications we studied so far are limited to inviscid flows. At present, we have not considered problems that involve viscosity, or mass and heat transfer as would be supported by the Navier-Stokes equations. Consequently, our investigation of discrete velocity Boltzmann-BGK models is limited to isothermal models. In addition, only the linear stability of the PML equations has been provided. However, these limitations can be the starting point for future work, which could include the more general case of an oblique nonuniform mean flow and a more comprehensive analysis of stability that takes into consideration the nonlinear

effects. Our present efforts have shown that effective nonreflective boundary conditions based on the Perfectly Matched Layer can be derived for discrete velocity Boltzmann-BGK models. This work has also provided a foundation on which future efforts can be built.

REFERENCES

- [1] Huang, K., *Statistical Mechanics*, Wiley, 1987.
- [2] Bhanatgar, P., Gross, E., and Krook, M., “A Model for Collision Process in Gases. I. Small Amplitude Process in Charged and Neutral One-Component Systems,” *Physical Review*, Vol. 94, No. 3, 1954, pp. 511–525.
- [3] He, X. and Luo, L.-S., “A Priori Derivation of the Lattice Boltzmann Equation,” *Physical Review E*, Vol. 55, No. 6, 1997, pp. 6333–6336.
- [4] He, X. and Luo, L.-S., “Theory of the lattice Boltzmann method: From the Boltzmann equation to the lattice Boltzmann equation,” *Physical Review E*, Vol. 56, No. 6, 1997, pp. 6811–6817.
- [5] Shi, Y., Zhao, T. S., and Guo, Z. L., “Finite Difference-Based Lattice Boltzmann Simulation of Natural Convection Heat Transfer in a Horizontal Concentric Annulus,” *Computers and Fluids*, Vol. 35, 2006, pp. 1–15.
- [6] Stiebler, M., Tolke, J., and Krafczyk, M., “An Upwind Discretization Scheme for the Finite Volume Lattice Boltzmann Method,” *Computers and Fluids*, Vol. 35, 2006, pp. 814–819.
- [7] Tamura, A. and Tsutahara, M., “Direct Simulation of Acoustic Waves Emitted from Moving Bodies by the Finite Difference Lattice Boltzmann Method,” AIAA paper 2006-2489, 2006.
- [8] Tsutahara, M., Kataoka, T., Shikata, K., and Takada, N., “New Model and Scheme for Compressible Fluids of the Finite Difference Lattice Boltzmann Method and Direct Simulations of Aerodynamic Sound,” *Computers and Fluids*, Vol. 37, 2008, pp. 79–89.
- [9] Chen, S. and Doolen, G. D., “Lattice Boltzmann Method for Fluid Flows,” *Annual Reviews of Fluid Mechanics*, Vol. 30, 1998, pp. 329–364.
- [10] Li, Q., He, Y. L., Wang, Y., and Tao, W. Q., “Coupled Double-Distribution-Function Lattice Boltzmann Method for the Compressible Navier-Stokes Equations,” *Physical Review E*, Vol. 76, No. 056705, 2007.

- [11] Kam, E. W. S., So, R. M. C., and Leung, R. C. K., “Lattice Boltzmann Method Simulation of Aeroacoustics and Nonreflecting Boundary Conditions,” *AIAA Journal*, Vol. 45, No. 7, 2007, pp. 1703–1712.
- [12] Marié, S., Ricot, D., and Sagaut, P., “Comparison Between Lattice Boltzmann Method and Navier-Stokes High Order Schemes for Computational Aeroacoustics,” *Journal of Computational Physics*, Vol. 228, 2009, pp. 1056–1070.
- [13] Reider, M. B. and Sterling, J. D., “Accuracy of Discret-Velocity BGK Models for the Simulation of the Incompressible Navier-Stokes Equations,” *Computers and Fluids*, Vol. 24, No. 4, 1995, pp. 459–467.
- [14] Marié, S., Ricot, D., and Sagaut, P., “Accuracy of Lattice Boltzmann Method for Aeroacoustic Simulations,” AIAA paper 2007-3515, 2007.
- [15] Qian, Y. H., d’Humières, D., and Lallemand, P., “Lattice BGK Models for Navier-Stokes Equation,” *Europhysics Letters*, Vol. 17, 1992, pp. 479–484.
- [16] Najafiyazdi, A. and Mongeau, L., “Radiation and Absorbing Boundary Conditions for the Lattice Boltzmann Method,” AIAA paper 2009-496, 2009.
- [17] Engquist, B. and Majda, A., “Radiation Boundary Conditions for Acoustic Equations and Elastic Wave Calculations,” *Communications on Pure and Applied Mathematics*, Vol. 32, No. 3, 1979, pp. 313–357.
- [18] Bayliss, A. and Turkel, E., “Radiation Boundary Conditions for Wave-Like Equations,” *Communications on Pure and Applied Mathematics*, Vol. 33, 1980, pp. 707–725.
- [19] Rudy, D. H. and Strikwerda, J. C., “A Non-Reflecting Outflow Boundary Condition for Subsonic Navier-Stokes Calculation,” *Journal of Computational Physics*, Vol. 36, 1980, pp. 55–70.
- [20] Rudy, D. H. and Strikwerda, J. C., “Boundary Conditions for Subsonic Compressible Navier-Stokes Calculations,” *Computers and Fluids*, Vol. 9, 1981, pp. 327–338.
- [21] Hagstrom, T. and Hariharan, S. I., “Accurate Boundary Conditions for Exterior Problems in Gas Dynamics,” *Mathematics and Computation*, Vol. 51, October 1988, pp. 581–597.

- [22] Tam, C. K. W. and Webb, J. C., “Dispersion-Relation-Preserving Finite Difference Schemes for Computational Acoustics,” *Journal of Computational Physics*, Vol. 107, 1993, pp. 262–281.
- [23] Thompson, K. W., “Time Dependent Boundary Conditions for Hyperbolic Systems,” *Journal of Computational Physics*, Vol. 68, 1987, pp. 1–24.
- [24] Thompson, K. W., “Time Dependent Boundary Conditions for Hyperbolic Systems, II,” *Journal of Computational Physics*, Vol. 89, 1990, pp. 439–461.
- [25] Giles, M. B., “Nonreflecting Boundary Conditions for Euler Equations Calculations,” *AIAA Journal*, Vol. 28, 1990, pp. 2050–2058.
- [26] Poinso, T. and Lele, S. K., “Boundary Conditions for Simulation of Compressible Viscous Flows,” *Journal of Computational Physics*, Vol. 101, 1992, pp. 104–129.
- [27] Schulze, D., “Far Field Boundary Conditions Based on Characteristic and Bicharacteristic Theory Applied to Transonic Flows,” *Fourteenth International Conference on Numerical Methods in Fluid Dynamics*, Vol. 453, Springer, Berlin, 1995, pp. 211–215.
- [28] Israeli, M. and Orszag, S. A., “Approximation of Radiation Boundary Conditions,” *Journal of Computational Physics*, Vol. 41, 1981, pp. 115–135.
- [29] Kosloff, R. and Kosloff, D., “Absorbing Boundaries for Wave Propagation Problems,” *Journal of Computational Physics*, Vol. 63, 1986, pp. 363–376.
- [30] Streett, C. L. and Macaraeg, M. G., “Spectral Multi-Domain for Large-Scale Fluid Dynamic Simulations,” *Applied Numerical Mathematics*, Vol. 6, 1989, pp. 123–139.
- [31] Rai, M. M. and Moin, P., “Direct Simulations of Turbulent Flow Using Finite Difference Schemes,” *Journal of Computational Physics*, Vol. 96, 1991, pp. 15–53.
- [32] Colonius, T., Lele, S. K., and Moin, P., “Boundary Conditions for Direct Computation of Aerodynamic Sound Generation,” *AIAA Journal*, Vol. 31, 1993, pp. 1574–1582.

- [33] Liu, C. and Liu, Z., “High Order Finite Difference and Multigrid Methods for Spatially Evolving Instability in a Planar Channel,” *Journal of Computational Physics*, Vol. 106, 1993, pp. 92–100.
- [34] Ta’asan, S. and Nark, D. M., “An Absorbing Buffer Zone Technique of Acoustic Wave Propagation,” AIAA paper 95-0164, 1995.
- [35] Freund, J. B., “Proposed Inflow/Outflow Boundary Conditions for Direct Computation of Aerodynamic Sound,” *AIAA Journal*, Vol. 35, No. 4, 1997, pp. 740–742.
- [36] Visbal, M. R. and Gaitonde, D. V., “Very High-Order Spatially Implicit Schemes for Computational Acoustics on Curvilinear Meshes,” *Journal of Computational Acoustics*, Vol. 9, No. 4, 2001, pp. 1259–1286.
- [37] Bodony, D. J., “Analysis of Sponge Zones for Computational Fluid Mechanics,” *Journal of Computational Physics*, Vol. 212, 2006, pp. 681–702.
- [38] Hu, F. Q., “On Absorbing Boundary Conditions for Linearized Euler Equations by a Perfectly Matched Layer,” *Journal of Computational Physics*, Vol. 129, 1996, pp. 201–219.
- [39] Hu, F. Q., “A Stable, Perfectly Matched Layer for Linearized Euler Equations in Unsplit Physical Variables,” *Journal of Computational Physics*, Vol. 173, 2001, pp. 455–480.
- [40] Hu, F. Q., “A Perfectly Matched Layer Absorbing Boundary Condition for Linearized Euler Equations with a Non-Uniform Mean Flow,” *Journal of Computational Physics*, Vol. 208, 2005, pp. 469–492.
- [41] Hu, F. Q., “On the Construction of PML Absorbing Boundary Condition for the Non-Linear Euler Equations,” AIAA paper 2006-0798, 2006.
- [42] Hu, F. Q., Li, X. D., and Lin, D. K., “PML Absorbing Boundary Conditions for Non-Linear Aeroacoustics Problems,” AIAA paper 2006-2521, 2006.
- [43] Appelo, D., Hagstrom, T., and Kreiss, G., “Perfectly Matched Layers for Hyperbolic Systems: General Formulation, Well-Posedness and Stability,” *SIAM Journal of Applied Mathematics*, Vol. 67, 2006, pp. 1–23.

- [44] Parrish, S. A. and Hu, F. Q., “PML Absorbing Boundary Conditions for the Linearized and Nonlinear Euler Equations in the Case of Oblique Mean Flow,” *International Journal for Numerical Methods in Fluids*, Vol. 60, No. 5, 2008, pp. 565–589.
- [45] Tsyntaxov, S. V., “Numerical Solution of Problems on Unbounded Domains. A review,” *Applied Numerical Mathematics*, Vol. 27, 1998, pp. 465–532.
- [46] Hu, F. Q., “Absorbing Boundary Conditions,” *International Journal of Computational Fluid Dynamics*, Vol. 18, No. 6, 2004, pp. 513–522.
- [47] Berenger, J. P., “A Perfectly Matched Layer for the Absorption of Electromagnetic Waves,” *Journal of Computational Physics*, Vol. 114, 1994, pp. 185–200.
- [48] Chew, W. C. and Weedon, W. H., “A 3D Perfectly Matched Medium from Modified Maxwell’s Equations with Stretched Coordinates,” *Microwave Optical Technical Letters*, Vol. 7, 1994, pp. 599–604.
- [49] Rappaport, C. M., “Perfectly Matched Absorbing Boundary Conditions Based on Anisotropic Lossy Mapping of Space,” *IEEE Microwave and Guided Wave Letters*, Vol. 5, No. 3, 1995, pp. 90–92.
- [50] Teixeira, F. L. and Chew, W. C., “General Closed-Form PML Constitutive Tensors to Match Arbitrary Bianisotropic and Dispersive Linear Media,” *IEEE Microwave and Guided Wave Letters*, Vol. 8, No. 6, 1998, pp. 223–225.
- [51] Hu, F. Q., Li, X. D., and Lin, D. K., “Absorbing boundary conditions for nonlinear Euler and Navier-Stokes equations based on the perfectly matched layer technique,” *Journal of Computational Physics*, Vol. 227, No. 9, 2008, pp. 4398–4424.
- [52] Najafiyazdi, A. and Mongeau, L., “A Perfectly Matched Layer Formulation for the Lattice Boltzman Method,” AIAA paper 2009-3117, 2009.
- [53] Pieraccini, S. and Puppo, G., “Implicit-Explicit Schemes for BGK Kinetic Equations,” *Journal of Scientific Computing*, Vol. 32, No. 1, 2007, pp. 1–28.
- [54] Pareschi, L. and Russo, G., “Implicit-Explicit Runge-Kutta Schemes and Application to Hyperbolic Systems with Relaxation,” *Journal of Scientific Computing*, Vol. 25, 2005, pp. 129–155.

- [55] Goldstein, H., *Classical Mechanics*, Cambridge, MA: Addison-Wesley, 1959.
- [56] Harris, S., *An Introduction to the Theory of the Boltzmann Equation*, Dover Publications, Inc., Mineola, New York, 2004.
- [57] Yvon, J., *La Théorie Statistique des Fluides et l'Equation d'Etat*, Paris: Hermann, 1935.
- [58] Bogoliubov, N. N., "Expansions into a series of powers of a small parameter in the theory of statistical equilibrium. Kinetic equations." *Journal of Physics USSR*, Vol. 10, No. 3, 1946, pp. 265–274.
- [59] Born, M. and Green, H. S., "A General Kinetic Theory of Liquids. I. The Molecular Distribution Functions," *Proceedings of the Royal Society of London. Series A, Mathematical and Physical Sciences*, Vol. 188 of A, 1946, pp. 10–18.
- [60] Kirkwood, J., "The Statistical Mechanical Theory of Transport Processes I. General Theory," *The Journal of Chemical Physics*, Vol. 14, No. 3, March 1946, pp. 180.
- [61] Cercignani, C., *Theory and Applications of the Boltzmann equation*, Scottish Academic Press, Edinburgh and London, UK, 1975.
- [62] Chapman, S. and Cowling, T. G., *The Mathematical Theory of Non-Uniform Gases*, Cambridge University Press, 3rd ed., 1970.
- [63] Grad, H., "On the Kinetic Theory of Rarefied Gases," *Communications on Pure and Applied Mathematics*, Vol. 2, No. 4, 1949, pp. 331–407.
- [64] Welander, P., "On the temperature jump in a rarefied gas," *Arkiv Fysik*, Vol. 7, No. 44, 1954, pp. 507–553.
- [65] Carleman, T., *Problèmes Mathématiques dans la Théorie Cinétique des Gaz*, Almquist and Wiksells, Uppsala, Sweden, 1957.
- [66] Kac, M., *Probability and Related Topics in the Physical Sciences*, New York: Interscience, 1959.
- [67] Broadwell, J., "Study of rarefied shear flow by the discrete velocity method," *Journal of Fluid Mechanics*, Vol. 19, 1964, pp. 401.

- [68] Shan, X., Yuan, X. F., and Chen, H., “Kinetic Theory Representation of Hydrodynamics: A Way Beyond the Navier-Stokes Equation,” *Journal of Fluid Mechanics*, Vol. 550, 2006, pp. 413–441.
- [69] Qian, Y. H., “Simulating Thermohydrodynamics with Lattice BGK models,” *Journal of Scientific Computing*, Vol. 8, 1993, pp. 231–242.
- [70] Weimar, J. R. and Boon, J. P., “Nonlinear Reactions Advected by a Flow,” *Physica A*, Vol. 224, 1996, pp. 207–215.
- [71] Becache, E., Fauqueux, S., and Joly, P., “Stability of Perfectly Matched Layers, Group Velocities and Anisotropic Waves,” *Journal of Computational Physics*, Vol. 188, 2003, pp. 399–433.
- [72] Hagstrom, T. and Nazarov, I., “Perfectly Matched Layers and Radiation Boundary Conditions for Shear Flow Calculations,” AIAA paper 2003-3298, 2003.
- [73] Kang, J. and Kallivokas, L. F., “Total wavefield-based inversion in PML-truncated domains,” *Journal of Physics: Conference Series*, Vol. 135, 2008, pp. 012055.
- [74] Parrish, S. A. and Hu, F. Q., “Application of PML Absorbing Boundary Condition to Aeroacoustic Problems with an Oblique Mean Flow,” AIAA paper 2007-3509, 2007.
- [75] Kennedy, C. A. and Carpenter, M. H., “Additive Runge-Kutta Schemes for Convection-Diffusion-Reaction Equations,” *Applied Numerical Mathematics*, Vol. 44, No. 1-2, 2002, pp. 139–181.
- [76] R. Weiner, M. Arnold, P. R. and Strehmel, K., “Partitioning strategies in Runge-Kutta type methods,” *IMA Journal of Numerical Analysis*, Vol. 13, No. 2, 1993, pp. 303–319.
- [77] Murua, A., “Formal series and numerical integrators, Part I: Systems of ODEs and symplectic integrators,” *Applied Numerical Mathematics*, Vol. 29, No. 2, 1999, pp. 221–251.
- [78] Tam, C. K. W., “Computational Aeroacoustics: An Overview of Computational Challenges and Applications,” *International Journal of Computational Fluid Dynamics*, Vol. 18, No. 6, 2004, pp. 547–567.

- [79] Frisch, U., Hasslacher, B., and Pomeau, Y., “Lattice-Gas Automata for the Navier-Stokes Equation,” *Physical Review Letters*, Vol. 56, No. 14, 1986, pp. 1505–1508.
- [80] Wolfram, S., “Cellular Automaton Fluids 1: Basic Theory,” *J. Stat. Phys.*, Vol. 45, 1986, pp. 471–526.
- [81] Luo, L., “The Future of Lattice-Gas and Lattice Boltzmann Methods,” ICASE MS 403, NASA Langley Research Center, 6 North Dryden Street, Building 1298, Hampton, Virginia 23681-0001, 1998.
- [82] McNamara, G. R. and Zanetti, G., “Use of the Boltzmann Equation to Simulate Lattice-Gas Automata,” *Physical Review Letters*, Vol. 61, 1988, pp. 2332–2335.
- [83] Dellar, P. J., “Bulk and shear viscosities in lattice Boltzmann equations,” *Physical Review E*, Vol. 64, No. 031203, 2001.

VITA

Elena Craig
 Department of Mathematics and Statistics
 Old Dominion University
 Norfolk, VA 23529

Education

Geodetic Engineering Courses, Transilvania University, Brasov, Romania, 1999–2000.
 Biology & Environmental Science Courses, Vassar College, Summer 2001.
 A.S. Mathematics and Science, Orange County Community College, 2002.
 B.S. Mathematics, Old Dominion University, 2005.
 M.S. Computational and Applied Mathematics, Old Dominion University, 2007.

Awards and Honors

Summer Research Scholarship for Community College Students, Vassar College, 2001
 Academic Achievement Award, Orange County Community College, 2002
 David Kotler Memorial Scholarship, Orange County Community College, 2002
 Faculty Perpetual Scholarship, Orange County Community College, 2002
 Virginia Commonwealth Grant (2004-2005)
 Dominion Graduate Scholar Award, Old Dominion University (2005-2006)
 University Graduate Fellowship, Old Dominion University (2007-2008)

Publications and Presentations

Craig, E., and Hu, F. Q., “A Perfectly Matched Layer for the Boltzmann-BGK Equation and its Application to the Lattice Boltzmann Method,” 2011 SIAM Conference on Computational Science and Engineering, Reno, Nevada, March 2011
 Craig, E., and Hu, F. Q., “On the Perfectly Matched Layer for the Boltzmann- BGK Equation and its Application to Computational Aeroacoustics,” 16th AIAA/CEAS Aeroacoustics Conference, AIAA Paper 2010-3935, 2010.
 Craig, E., and Hu, F. Q., “A Perfectly Matched Layer for the Boltzmann-BGK Equation,” SIAM Conference, Old Dominion University Chapter, April, 2010.